

Examination of Hydrophobic/Hydrophilic Dual Layer Membranes for Membrane Distillation

Inci Boztepe

Bachelor of Chemical Engineering

Institute of Sustainable Industries and Liveable Cities

College of Engineering and Science

Victoria University

**Thesis submitted in fulfilment of the requirements for the degree of Master
of Engineering (by Research)**

(2018)



Abstract

Membrane Distillation (MD) is a separation technology that uses a temperature difference across a membrane to purify water. Membrane distillation has been known since the early 1960s and there are still breakthroughs to be made. Improvements in the module design or new membranes materials, such as composite membranes, are being investigated, and much research has focused on these aspects.

This study focused on membrane distillation performance for direct contact membrane distillation with 5 different membranes, which included 3 hydrophobic and 2 hydrophobic/hydrophilic dual layer membranes. Their performance was modelled using mathematical modelling program MATLAB. The purpose of the study was to predict the flux and energy efficiency for membranes, and verify with the experimental work. This work extended membrane distillation 1-D modelling to dual layer membranes, which has not previously been performed. The approach of the study required membrane characterization tests to provide input parameters to the model, and also serve as parameters for explaining the flux performance of the membranes. The membrane characteristics measured were porosity, thickness, tortuosity and pore size. Membrane distillation experiments were performed at different feed and cold inlet temperatures and flowrates, and permeate fluxes for various membranes and different operating conditions were measured and analysed.

The experimental results were compared with predictions from the mathematical modelling for both the single layer and dual layer membranes, and very good agreements have been found. Error was within 10% for flux and energy efficiencies between the experiments and the model. Single layer membranes' performances were found better than dual layer membranes. The thickness of the hydrophobic layer was the highest among the other membranes, hence it affected heat and mass transfer across the membrane adversely compared to single layer membranes. Therefore, the permeate flux and energy efficiency was lower for dual layer membrane compared to single layer membranes. Better performance for single layer membranes can be attributed to their characteristics.

Declaration of Authenticity

Masters by Research Student Declaration Master by Research Declaration “I, Inci Boztepe, declare that the Master by Research thesis entitled, “Examination of Hydrophobic/Hydrophilic Dual Layer Membranes for Membrane Distillation” is no more than 60,000 words in length including quotes and exclusive of tables, figures, appendices, bibliography, references and footnotes. This thesis contains no material that has been submitted previously, in whole or in part, for the award of any other academic degree or diploma. Except where otherwise indicated, this thesis is my own work”.

Signature



Date: 11/08/2018

Acknowledgement

I would like to appreciate my principal supervisor, Prof. Stephen Gray, Executive Director of Institute for Sustainable Industries and Liveable Cities (ISILC), Victoria University for his great supervision and an endless source of information in the area throughout for this project.

I thank to my co-supervisor, Prof. Jun-De Li, College of Engineering & Science, Victoria University, for his detailed help for modelling as part of the for MATLAB and his way of teaching in depth knowledge in modelling.

I am greatly thankful to my another co-supervisor, Dr. Jianhua Zhang, Institute for Sustainable Industries and Liveable Cities (ISILC), as being wonderful guide during the experiments and broadening my experimental knowledge in the area.

I also thank Dr. Zongli Xie, Derrick Ng, and Guang Yang for helping to me use the SEM, and Porometer at CSIRO under their guidance.

I am thankful to Prof. Ho Kyong Shon, Centre for Technology in Water and Wastewater, School of Civil and Environmental Engineering, University of Technology, Sydney for providing a dual layer membrane for examination in this project.

I need to thank all the researchers in ISILC for their help and guidance for using experimental equipment. In particular, I thank my friends Digby Wrede and Dr. Ikechukwu A. Ike, for their help and passion in answering all my questions.

I would like to thank to my great family, especially my mum and sister, for their continuous support and encouragement through the years. This work could not be completed without my mum's support.

List of Publications

Poster Presentation

Inci Boztepe, Stephen Gray, Jun-De Li, Jianhua Zhang, “Mathematical Modelling of DCMD for PTFE membrane”, Early Career Researcher Membrane Symposium, Membrane Society of Australasia, 5-6 February 2018, Sydney, Australia.

TABLE OF CONTENTS

Abstract	i
Declaration	ii
Acknowledgement	iii
List of Publications	iv
Table of Contents	v
List of Figures	ix
List of Tables	xii
Chapter 1. INTRODUCTION	1
1.1. Background.....	1
1.2. Research Objectives.....	3
1.3. Thesis Outline.....	4
Chapter 2. LITERATURE REVIEW	6
2.1. Introduction.....	6
2.2. Comparison of Membrane Liquid Separation Technologies.....	6
2.3. Direct Contact Membrane Distillation Theory.....	9
2.4. Membrane Distillation Configurations.....	12
2.5. Historical Evaluation of Membrane Distillation.....	13
2.6. Membrane Distillation Studies.....	14
2.7. Membranes Used in Membrane Distillation.....	15
2.8. Performance of Single and Dual Layer Membranes.....	19
2.9. Mathematical Modelling in Membrane Distillation.....	23
2.9.1. Modelling of hydrophobic single layer membranes.....	24
2.9.2. Modelling of hydrophobic/hydrophilic dual layer membranes.....	25
2.10. Objectives.....	26

Chapter 3. EXAMINATION OF CHARACTERIZATION TESTS FOR SINGLE LAYER AND DUAL LAYER MEMBRANES.....	28
3.1. Introduction.....	28
3.2. Experimental and Methods.....	29
3.2.1. Membrane types.....	29
3.2.2. FTIR spectroscopy analysis.....	30
3.2.3. Liquid entry pressure (LEP) measurement.....	30
3.2.4. Contact angle measurement	31
3.2.5. Porosity measurement.....	31
3.2.6. Pore size measurement.....	32
3.2.6.1. Gas permeation test.....	32
3.2.6.2. Porometer (Wet/Dry Run Method).....	34
3.2.7. SEM measurement (Thickness).....	35
3.3. Results and Discussion	35
3.3.1. Membrane properties.....	35
3.4. Summary.....	51
Chapter 4. PERFORMANCE OF SINGLE LAYER AND DUAL LAYER MEMBRANES IN MEMBRANE DISTILLATION.....	53
4.1. Introduction.....	53
4.2. Membrane Distillation Performance Parameters.....	53
4.2.1. Process conditions.....	53
4.2.2. Membrane module.....	55
4.3. Direct Contact Membrane Distillation Performance.....	57
4.4. Experimental and Methods.....	59
4.5. Results and Discussion	61
4.5.1. Direct Contact Membrane Distillation (DCMD) tests for single and dual layer membranes.....	61
4.5.1.1. Global mass transfer coefficient (C_{global}) dependence on velocity.....	61

4.5.1.2. Global mass transfer coefficient (C_{global}) relation with temperature.....	63
4.5.1.3. Salt rejection and velocity relation for single and dual layer membranes.....	67
4.5.1.4. Feed inlet temperature effect on salt rejection	68
4.6. Summary.....	70
Chapter 5. MATHEMATICAL MODELLING OF MEMBRANE DISTILLATION AND COMPARISON WITH EXPERIMENTAL RESULTS.....	72
5.1. Introduction.....	72
5.2. Modelling Assumptions.....	73
5.3. Modelling Structure	73
5.3.1. Mass and energy balance equations	74
5.3.1.1. Mass balance.....	74
5.3.1.2. Energy balance.....	75
5.3.2. Transport model (Transfer resistances) equations	76
5.3.2.1. Mass transfer resistance.....	76
5.3.2.2. Heat transfer resistance.....	76
5.3.3. Flow model equations.....	78
5.3.3.1. Mass flux.....	78
5.3.3.2. Heat flux.....	80
5.3.3.2.1. Heat flux through hydrophobic single layer membrane	80
5.3.3.2.2. Heat flux through hydrophobic/hydrophilic dual layer membrane.....	82
5.3.4. Physical property model equations.....	85
5.3.5. Spacer modelling.....	87
5.4. Experimental and Methods.....	88
5.4.1. Modelling algorithms	88
5.4.2. Modelling inputs.....	91
5.5. Results and Discussion	92

5.5.1. Temperature profiles for co- and counter-current flows along the membrane length.....	92
5.5.2. Model verification.....	95
5.5.2.1. Flux prediction at different feed velocities.....	95
5.5.2.2. Flux prediction at different inlet temperatures.....	97
5.5.2.3. Validation of energy efficiency at different temperatures.....	100
5.6. Summary.....	103
Chapter 6. CONCLUSION AND RECOMMENDATIONS.....	106
6.1. Introduction.....	106
6.2. Outcomes.....	107
6.3. Recommendations for future studies.....	109
Nomenclature.....	110
References.....	113
Appendix.....	118

List of Figures

Figure 1.1. MD publications between 1991 and 2018.....	1
Figure 2.1. Generic flow diagram for membrane separation processes.....	7
Figure 2.2. Direct Contact Membrane Distillation process schema.....	9
Figure 2.3. Heat and mass flow across the membrane in direct contact membrane distillation.....	11
Figure 2.4. Membrane wetting schematic demonstration.....	12
Figure 2.5. Membrane Distillation configuration types.....	13
Figure 2.6. Distribution of publications due to different MD applications during three phases.....	15
Figure 2.7. Membrane structure classification.....	15
Figure 2.8. Diagram of the temperature and concentration profile through a hydrophobic/hydrophilic dual layer membrane.....	26
Figure 3.1. Set-up for LEP test.....	31
Figure 3.2. Gas permeability measurement experimental set-up.....	34
Figure 3.3. FT-IR images of membranes	38
Figure 3.4. SEM images of membrane surfaces.....	41
Figure 3.5. Cross sections of membranes.....	44
Figure 3.6. Pore flow distributions.....	47
Figure 3.7. Contact angle measurement images for membranes.....	51
Figure 4.1. Parameters for better performance MD.....	53
Figure 4.2. Tubular module for hollow fiber and plate module for flat sheet membrane.....	55

Figure 4.3. Plate and frame DCMD module set-up.....	56
Figure 4.4. Flow modes for DCMD.....	57
Figure 4.5. Membrane Distillation process set-up.....	59
Figure 4.6. Global mass transfer coefficient relation to velocity for co-current flow at 60°C feed and 20°C permeate inlet temperatures	62
Figure 4.7. Global mass transfer coefficient relation to velocity for counter-current flow at 60°C feed and 20°C permeate inlet temperatures.....	63
Figure 4.8. Global mass transfer coefficient relation to feed inlet temperature for co-current	64
Figure 4.9. Vapour pressure relation to temperature	65
Figure 4.10. Global mass transfer coefficient versus feed inlet temperature for counter-current.....	66
Figure 4.11. Salt rejection at different velocities for co-current flow at 60°C feed and 20°C permeate inlet temperatures	67
Figure 4.12. Salt rejection at different velocities for counter-current flow at 60°C feed and 20°C permeate inlet temperatures	68
Figure 4.13. Salt rejection at different feed inlet temperatures for co-current flow.....	69
Figure 4.14. Salt rejection at different feed inlet temperatures for counter-current flow.....	70
Figure 5.1. Membrane vapor transport regions.....	79
Figure 5.2. Diagram of the temperature and concentration profile through hydrophobic membrane and composite hydrophobic/hydrophilic dual layer membrane.....	82
Figure 5.3. Spacer figure.....	87
Figure 5.4. Diagram of the modelling algorithm for simulation of co-current DCMD.....	89

Figure 5.5. Diagram of the modelling algorithm for simulation of counter-current DCMD.....	90
Figure 5.6. Temperature profile for co-current flow of single layer membrane.....	92
Figure 5.7. Temperature profile for counter-current flow of single layer membrane.....	93
Figure 5.8. Temperature profile of co-current flow for M5.....	94
Figure 5.9. Temperature profile for counter-current flow of M5.....	95
Figure 5.10. Flux versus velocity at 60°C hot and 20°C cold inlet with co-current flow.....	96
Figure 5.11. Flux versus velocity at 60°C hot and 20°C cold inlet with counter-current.....	97
Figure 5.12. Flux versus feed inlet temperature with co-current flow.....	98
Figure 5.13. Flux versus feed inlet temperature with counter-current flow.....	99
Figure 5.14. Flux versus permeate inlet temperature with co-current flow.....	100
Figure 5.15. Energy efficiency at different feed inlet temperatures with co-current...	101
Figure 5.16. Thermal efficiency at different feed inlet temperatures with counter-current.....	102
Figure 5.17. Correlation between ϵ/bt and flux/energy efficiency at 60°C feed and 20° permeate inlet temperatures.....	103

List of Tables

Table 1.1. MD process parameters and their corresponding costs in 2017.....	2
Table 2.1. Different membrane separation techniques and their properties.....	8
Table 2.2. Advantages and disadvantages of MD process.....	10
Table 2.3. Polymeric materials and their properties.....	16
Table 2.4. Common flat sheet commercial membranes used in MD.....	18
Table 2.5. Studies on MD membranes and their characteristics for dual layer membranes and hydrophobic membranes.....	20
Table 3.1. Membrane codes and their compositions.....	29
Table 3.2. Membrane characteristics.....	35
Table 4.1. Different experimental conditions for DCMD experiments.....	60
Table 4.2. Module flow channel dimensions and membrane areas.....	61
Table 5.1. Equations used to describe the physical properties of water.....	85
Table 5.2. Spacer and module dimensions.....	91
Table 5.3. Membranes and their conductivities.....	91

CHAPTER 1. INTRODUCTION

1.1. Background

Membrane Distillation (MD) is a membrane separation technology that has been known since the 1960s. MD can be used in different applications such as desalination, environmental-waste clean-up and treatment of food-dairy stream. MD was developed in laboratory tests and was then scaled up to be used in industry. Amongst researchers, MD is being studied to improve its performance in terms of enhancing the MD permeate flux and reducing the energy consumption of the process. For MD process, there are some obstacles that should be focused on by researchers, which are membrane and MD module design, membrane wetting, low permeate flux, and high thermal energy consumption. To overcome these problems in MD, suitable membrane materials, module designs and process conditions became vital research subjects.

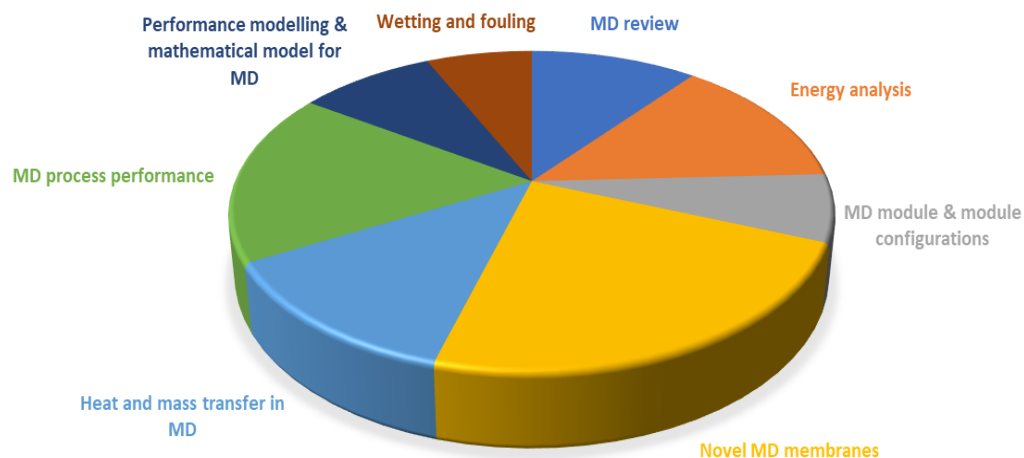


Figure 1.1. MD publications between 1991 and 2018

Fig. 1.1 shows the relative proportion of papers that have been published in MD between 1991 and 2018. Throughout the years in membrane distillation research, novel membranes for MD contributed most of the research focus, followed by MD process performance and heat and mass transfer in MD.

The inadequacy of commercial MD membranes and its poor economic performance meant that MD was not commercialized in the late 1960s [1-3]. After 1980s, with developments in suitable, good performance MD membranes and MD module designs, MD has gained its place for the applications [4]. After 2000s, MD developers have installed MD pilot and demonstration plants [5]. The first pilot for MD separation technology was Memstill®, which was conducted in Singapore Senoko Incineration Plant in 2006 with a capacity of 1 m³ per day [1, 5]. After 5 years, Memstill® installed a demonstration plant with capacity of 100 m³/day in Singapore at Jurong Island. Another pilot plant was commissioned by Memsys®, MD technology developer, using solar power in Singapore with 1 m³ a day capacity [5]. The first MD desalination plant based on seawater with capacity of 10 m³ per day company was commissioned by Aquaver in Maldives using waste heat from a diesel electricity generation system in 2014 [4]. A larger MD demonstration treating sea water RO brine of capacity 400 m³ per day has been constructed in Korea, however, no performance data has yet been published. MD desalination plant can be operated in combination with power plant and/or other types of low grade energy sources like waste industrial heat and renewable energy to reduce the cost and consumption of energy used in the process [6]. However, MD plants with small capacity could be a reason for slow progress and growth of MD [5].

Another issue for MD desalination plants other than their capacities is cost. Cost differs depending upon the MD plants' location, process water conditions, the size of plant, and available and economic heat source [3]. Table 1.1 includes parameters and their corresponding costs adapted from [7].

Table 1.1. MD process parameters and their corresponding costs in 2017 [7]

Parameters	Capital, \$
MD module	161,967
Membrane cost (m ²)	60
Electric cost (KW/h)	0.069

Because MD requires moderate temperature to provide the thermal driving force across the membrane, utilizing renewable solar energy or waste heat can reduce water production cost [8]. Using the aforementioned alternative energy sources enables the required energy cost for MD to be reduced. Improving membranes and membrane module designs for MD can also ameliorate the size of the MD pilot and demonstration desalination plants.

Choosing the appropriate membranes for MD has been an issue for commercialisation of the process [2]. Although hydrophobic membranes such as PTFE, PVDF, and PP have been the preferred membranes for MD for many years for desalination purposes, manufacturing new ideal membranes has been considered in academia [9]. A membrane closer to the 'Ideal MD membrane' is required to meet high mass transfer and low heat transfer through the membrane. Changing the hydrophobic material of the membrane does not highly affect the heat transfer because thermal conductivities for most hydrophobic polymers are similar [9]. However, it was proposed that an additional hydrophilic support layer would improve the heat transfer characteristics for dual layer membranes. The necessity of finding the ideal membranes has arisen from this idea and use of hydrophobic/hydrophilic dual layer membranes was proposed by [10].

1.2. Research Objectives

The claims for improved heat transfer outcomes by hydrophobic/hydrophilic dual layer membranes has only been described by conceptual models that have not quantified how reduced conductive heat transfer occurs. Quantifying this via modelling of the performance of dual layer membranes is something that has not previously been done. Lack of modelling work around dual layer hydrophobic/hydrophilic membranes inspired the purpose of this work, which is accurate modelling of dual layer composite membranes. Although some modelling studies are available for hydrophobic/hydrophilic dual layer membranes in the literature, none of them predicted the MD flux and energy efficiency using 1-D model, and some of them were just conceptual models that identify the concept of heat and mass transfer through dual layer membranes. Therefore, the originality of the work stems from using a 1-D model to calculate heat and mass transfer across the hydrophobic/hydrophilic membrane, and to verify the model with experimental results from desalination tests.

Performance modelling was undertaken, and experimental results used to verify the model. Modelling work considered how differences between the membranes should be modelled to accurately describe their heat and mass transfer mechanisms. To address this issue, heat and mass transfer equations were derived for hydrophilic/hydrophobic dual layer membranes, which can be found in the Chapter 5. Those equations were gathered from published references. Besides using hydrophobic/hydrophilic membranes, oleophobic coating on polyethylene (PE) membrane was also tested and modelled for the DCMD. However, mathematical modelling for polyurethane (PU) coated PTFE membrane has not been done due to the complexity of the model in terms of facing the hydrophilic layer on the feed side and time constraints.

1.3. Thesis Outline

Chapters contributing to this thesis can be summarised as follows:

Chapter 1 – Introduction, presents MD background from research and industrial concept.

Chapter 2 – Literature Review, focuses on MD applications, MD studies, MD membranes including identification of single and dual layer membranes that were studied in previous studies, and modelling works for hydrophobic and hydrophobic/hydrophilic membranes.

Chapter 3 – Examination of Characterization Tests for Single Layer and Dual Layer Membranes, describes characterization tests used in this work. These tests include LEP measurement, FT-IR spectroscopy, Scanning Electron Microscopy (SEM), gas permeability, porosity and pore sizes. These characteristics were used for comparison with previous studies and to describe the membrane in the modelling program.

Chapter 4 – Performance of Single Layer and Dual Layer Membranes in Direct Contact Membrane Distillation, presents MD tests for both hydrophobic and hydrophobic/hydrophilic membranes under different operating conditions, such as feed inlet and cold inlet temperatures, and flow rates for desalination. These results are used for comparison with modelling predictions.

Chapter 5 – Mathematical Modelling for Membrane Distillation describes modelling equations, which were coded in the modelling program and that describe the heat and

mass flows and transfers through the membrane. Comparison between model predictions and experimental results was undertaken.

Chapter 6 – Conclusions and Recommendations summarises the conclusions for this study and also gives some recommendations for future studies, which can lead to further detailed understanding of dual layer membrane performance.

CHAPTER 2. LITERATURE REVIEW

2.1. Introduction

Membrane distillation (MD) is a thermal separation process in which vapour transportation through a non-wetted porous hydrophobic membrane is driven by vapour pressure difference between the two sides of the membrane [11]. MD is an emerging technology with developments for processes as well as for high performance membrane materials being researched. There are different types of MD configurations, such as direct contact MD, air gap MD, vacuum MD as well as sweeping gas MD for various applications such as desalination, water-reuse, and waste clean-up [12]. In the early 1980s membrane distillation studies became active and membrane distillation research developed strongly during that period. It has been stated that 61% of membrane distillation studies included performance modelling, and many membrane distillation publications focused on direct contact membrane distillation process in terms of being the most suitable configuration for desalination [13].

This chapter will review different membrane separation technologies with the focus on MD membranes and MD process modelling. This will include a history of MD development and its applications.

2.2. Comparison of Membrane Liquid Separation Technologies

Membrane separation technology has gained popularity in applications because of its high water quality performance and low electrical energy and maintenance costs compared to conventional water technologies [14]. There are also some advantages for using membrane separation technologies over conventional separation technologies, such as lower chemical use during the process, removal of microorganisms, convenient operation and construction, zero liquid discharge with the assistance of evaporators, and conserving water use by reusing the permeate in water recycling applications [14]. Membrane separation processes compete with the other physical methods of separation such as sand filtration, settling, adsorption, distillation, and crystallisation [15]. The membrane is the key feature that differentiates membrane separation processes from other separation processes. For separation, a driving force is needed across the membrane. The driving force should be either pressure, temperature, concentration or electrical potential [15]. Membranes used for water related technologies experience problems such as membrane

fouling, wetting, mechanical failure and ageing/degradation of the membrane, which are all operational issues for membrane processes. However, these problems can be overcome by improving membrane properties.

Applications for membrane separation technology include municipal water and wastewater treatment, reuse applications, industrial water treatment/recycling and desalination of seawater and brackish water. A generalised diagram for membrane separation processes can be found below in Fig 2.1 [16].

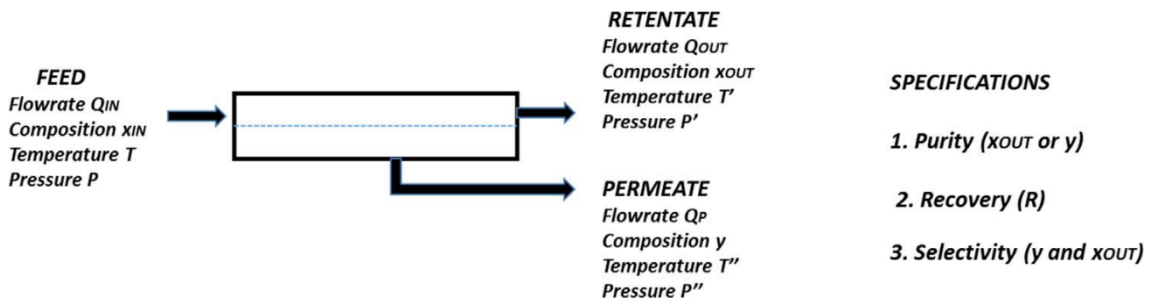


Figure 2.1. Generic flow diagram for membrane separation processes [16]

Pressure-driven membrane processes consist of reverse osmosis, nanofiltration, ultrafiltration, and microfiltration. Reverse osmosis is the most commonly used membrane separation technology, which has the oldest commercial membranes, and was established commercially in the 1960s. More recently, pervaporation and vapor permeation are the latest membrane separation technologies to seek wider commercial application [17]. The difference between these processes is that latent heat is used to pervaporate the liquid for transport through the pervaporation membrane, whereas there is no phase change for vapour permeation [15]. Microfiltration is generally used to separate solid particles from liquids via size exclusion and pores sizes are general $<1 \mu\text{m}$ [14]. Among the membrane separation processes, microfiltration membranes have the largest pores, followed by ultrafiltration membranes. Microfiltration and ultrafiltration membrane separation technologies are similar with regards to their equipment and operation, with the pore size of the membranes the only significant difference [17]. The pore size that distinguishes microfiltration from ultrafiltration is arbitrary, but is commonly regarded as being $0.1 \mu\text{m}$, with microfiltration membranes having pores $>0.1 \mu\text{m}$ and ultrafiltration membranes pores that are $<0.1 \mu\text{m}$. Ultrafiltration is used to remove

particles and high molecular weight molecules, that are in the range of 0.001 to 0.02 μm . Particles and molecules smaller than the pore size pass through the membrane, whereas the larger particles and macromolecules are retained [15].

Reverse osmosis (RO) has the smallest pore sizes and is mainly used for desalination processes [17]. Table 2.1 shows different membranes for liquid based separation technologies, their driving forces, membrane types as well as applications [15, 18].

Table 2.1. Different membrane separation techniques and their properties

Membrane Separation	Membrane Type	Driving Force	Applications
Microfiltration Ultrafiltration	Symmetric microporous Asymmetric microporous	Hydrostatic pressure	Clarification Separation of macromolecular solutions
Nanofiltration, Reverse osmosis	Asymmetric dense membranes	Hydrostatic pressure	Separation of small organic compounds and salts from solutions
Pervaporation	Asymmetric, dense composite	Concentration gradient, vapour pressure	Separation of mixtures of volatile liquids
Vapour permeation	Dense membrane, composite	Concentration gradient	Separation of volatile vapours and gases
Electrodialysis	Dense ion conducting membranes	Electrical potential	Separation of salts, charged species
Membrane Distillation	Microporous	Vapour Pressure	Separation of water from non-volatile solutes

2.3. Direct Contact Membrane Distillation Theory

Operating at low temperature and transmembrane hydrostatic pressure makes MD a desirable membrane separation process to be used in different applications with the most of its potential applications in desalination [12]. MD is a thermally driven membrane separation process in which evaporation and condensation takes place on the feed and permeate sides of the membrane, respectively. Vapour is evaporated because of a temperature or vapour pressure difference across the membrane. Vapour molecules transports through the membrane, and are condensed due to the low temperature on the permeate side for direct contact membrane distillation.

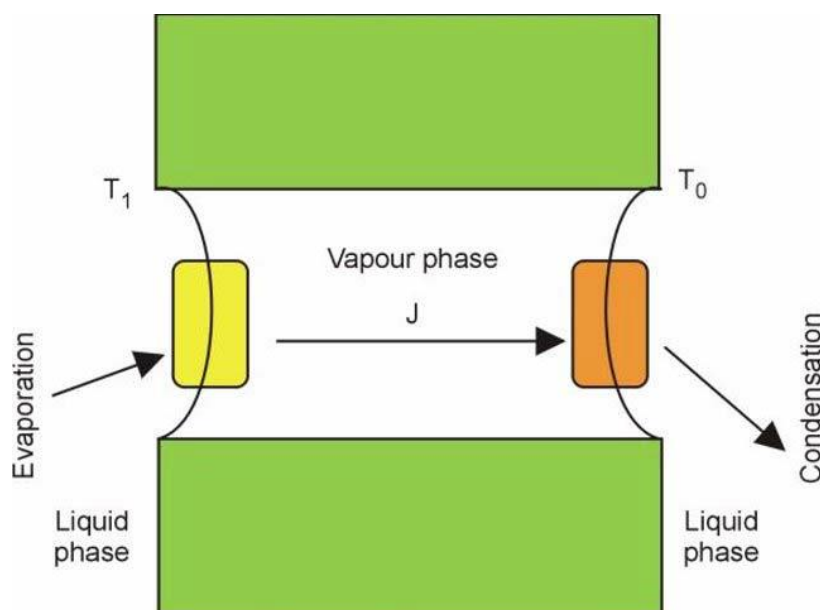


Figure 2.2. Direct Contact Membrane Distillation process schema [19]

Fig. 2.2 represents the vapour transportation through the membrane including evaporation and condensation during direct contact membrane distillation [19]. There are some obstacles that can be overcome by using MD technology, such as reaching high solute concentration, pure water production as permeate and reducing the effects of concentration polarization at very high salt concentrations [19, 20]. Increasing the feed flow rate and using spacers [21] can minimise concentration polarization in DCMD by inducing turbulent flow [22].

In MD, heat and mass transfer phenomena occur simultaneously [12]. Water vapour molecules transport across the membrane, and membrane pores should not be wetted throughout this process. Use of hydrophobic membranes does not allow liquid to enter membrane pores unless the transmembrane pressure exceeds the liquid entry pressure (LEP). MD has some advantages and disadvantages when it is compared to other membrane separation technologies and conventional separation technologies as identified in Table 2.2 [6, 20, 23].

Table 2.2. Advantages and disadvantages of MD process

Advantages of MD	Disadvantages of MD
Low operating temperatures	Heat loss by conduction
High rejection factor	Lower flux encountered with mass transfer resistance and drop in driving force along the membrane
Reduced corrosion problems	Membrane wetting and fouling
Less tendency to foul	High thermal energy consumption
Feasible for combining with the other membrane separation technologies	
Being able to use alternative or waste energy sources	

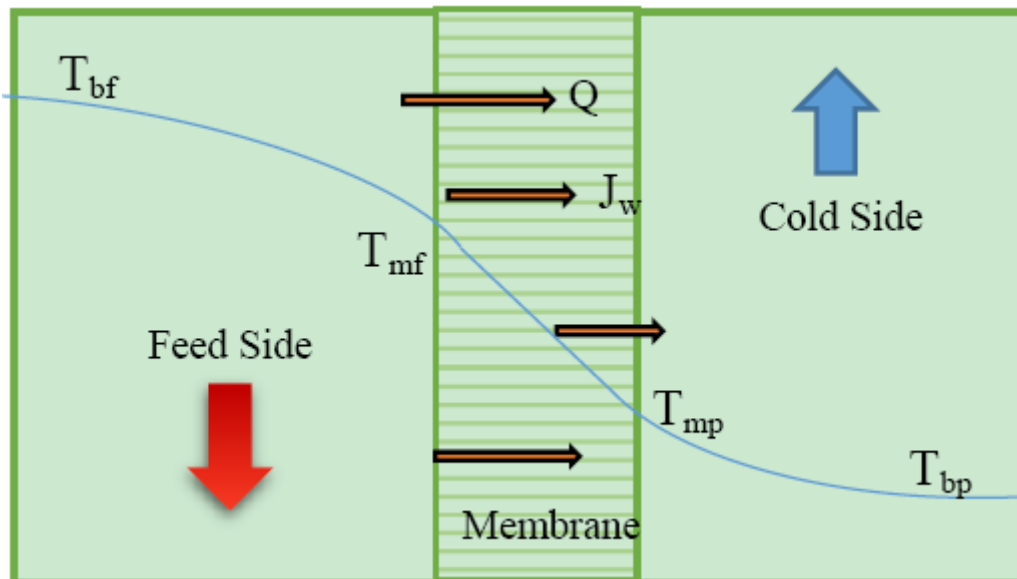


Figure 2.3. Heat and mass flow across the membrane in direct contact membrane distillation: T_{bf} , bulk feed temperature; T_{mf} , membrane interface temperature on feed side; Q , heat transfer; J_w , mass flux; T_{mp} , membrane interface temperature on permeate side; T_{bp} , bulk permeate temperature [24]

Fig. 2.3 describes the heat and mass transfer in MD process [24]. As it can be seen from Fig. 2.3, the feed side is the saline water and cold side is the pure permeate (water) and they are separated by a membrane in between. When water vapour is transported towards the cold permeate side, non-volatiles (salt-ions) cannot pass through the membrane to the permeate, so the non-volatile components remain in the hot feed. Fouling in MD consists of three types: organic, inorganic and biological fouling [25, 26]. When inorganic or organic compounds accumulate on the membrane surface or pores, membrane fouling occurs via interactions between foulants and between foulants and the membrane surface. This can lead to membrane wetting [25, 27]. Foulants may totally or partially block the pores as it is depicted in Fig. 2.4 [25, 28].

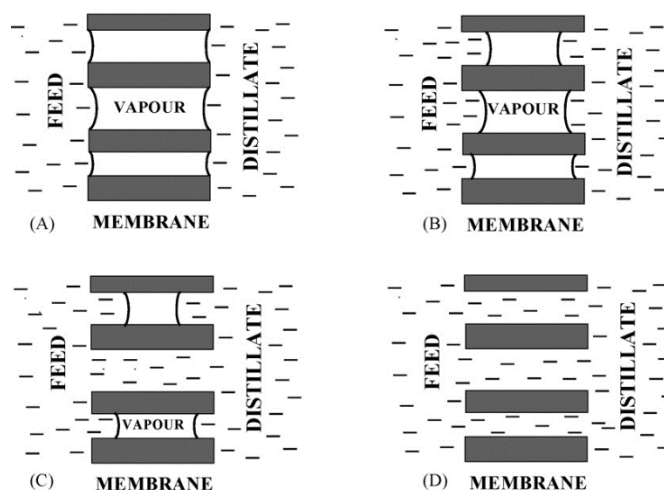


Figure 2.4. Membrane wetting schematic demonstration (A) non-wetted; (B) surface wetting; (C) partial wetting; (D) wetted [28]

Interactions between proteins, lipids and membrane decreases the liquid surface tension on the membrane surface, which lowers the wetting pressure [29]. If the transmembrane pressure is higher than the LEP as aforementioned, salt ions penetrate the membrane pores as membrane wetting occurs. Membrane wetting can also occur if the liquid phase surface tension is decreased, so the LEP is reduced. This may happen due to high organic content in the feed, or if surfactant is present in the feed. [30]. A more detailed description of heat and mass transfer in DCMD will be discussed in Chapter 5.

2.4. Membrane Distillation Configurations

Bulk feed solution is in direct contact with the membrane surface in all membrane distillation processes, and water evaporates on the membrane surface of the feed side. In DCMD, vapor transports through the porous membrane to the permeate side followed by condensation into the permeate. In air gap membrane distillation (AGMD), stagnant air is positioned between the membrane and the permeate stream [31]. Water vapor condenses on the condensation plate in the air gap, allowing the heat of condensation to be transferred to a coolant and often this is the feed. By this mechanism heat loss by conduction can be reduced [32]. Nevertheless, the air gap reduces the rate of mass transfer lowering membrane flux [33]. For sweeping gas membrane distillation (SGMD), water vapour is condensed outside of the membrane module. Heat loss is also reduced with this configuration similar to AGMD, but the mass transfer coefficient for SGMD is enhanced

due to a non-stationary gas barrier. Finally, for vacuum membrane distillation (VMD), a vacuum is created by a pump on the permeate side of the membrane. Vapor condensation is processed outside the membrane module, and the conductive heat loss across the membrane can be neglected for this configuration [11, 20]. All MD configurations have their pros and cons for different applications of MD [11]. Fig. 2.5 depicts schematically the different types of Membrane Distillation configurations [34].

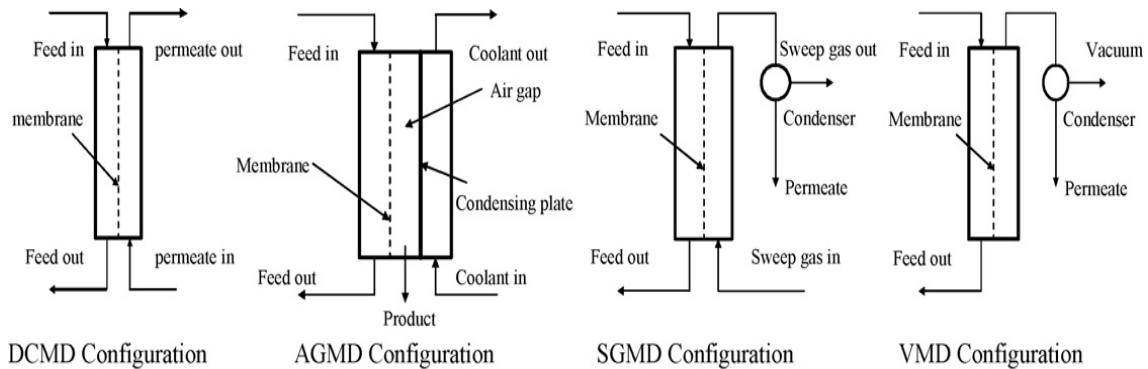


Figure 2.5. Membrane Distillation configuration types [34]

2.5. Historical Evaluation of Membrane Distillation

Membrane distillation is a process that has been studied for over 50 years. The first membrane distillation patent was granted to Bodell in 1963, followed by the first published MD paper using DCMD configuration by Findley in 1967 [5, 12]. Demineralized water recovery from saline water method using MD was the new approach for improving the desalination efficiency, and a patent was granted to Weyl in 1967. In this process, hot feed solution was in direct contact with membrane as well as cold permeate solution [5]. Weyl used a PTFE membrane with 3.2 mm thickness, 9 μm mean pore size and 42 percent of porosity. Other types of hydrophobic membranes such as polyethylene (PE), polypropylene (PP) and polyvinyl chloride (PVC) were also proposed. Findley also emphasized the most suitable membrane for MD in his publication in 1967. Sweeping gas membrane distillation and vacuum membrane distillation configuration were used by Bodell in his second patent in 1968. Bodell and Weyl were studying the desalination of saline water using MD process, whereas Findley was studying heat and mass transfer phenomena that occurs in MD process [35]. For a decade after 1970, a period called the 'death phase' for MD occurred since there was no study that could be found in the area [35]. The reason could be the breakthrough of high flux RO membrane

based on an asymmetric cellulose acetate membrane developed by Loeb and Sourirajan. By 1980s, with the advancements in manufacturing new membranes, the popularity for research to enhance MD performance rose [35]. In 1982, Cheng & Wiersma were granted a patent for developing the first composite hydrophobic/hydrophilic membrane for MD. A 'Workshop in MD' was held in Rome on 5th May in 1986 and the terminology of MD was discussed during the workshop. MD was commercialized by the companies such as Gore and Associates, Enka AG and Swedish Development Co. after 1985.

Current studies mostly focus on fabricating suitable membranes for MD that can give higher permeate flux and can consume lower energy in the process. Membrane fabrication gained popularity as a research area for membrane distillation and fabrication of composite membranes is a key research area [5].

2.6. Membrane Distillation Studies

Membrane distillation applications consist of desalination, brine concentration, food applications, chemical processes, and wastewater treatment processes [36]. MD is mostly used in these areas for separation and water treatment [5]. MD is also applied for volatile component separation from liquid solutions [34]. The most utilised membrane distillation application studied is desalination. Between the years 1970 and 1990, desalination studies accounted for 67% of MD articles. Between 1991 and 2010, desalination related MD was 34% of the studies. After 2011, desalination studies consisted of 48% of MD articles. Brine concentration and food industry applications were unknown before 1991. From 1991 to 2010, brine concentration and food applications gained in popularity among MD papers. Since 1991, MD brine concentration research has increased, whereas application for food industry has accounted for just 4% of the publications for MD. Food industry applications consist of concentration of food products, fruit juices, aromatic compounds, and whey protein. MD has also been studied for wastewater treatment applications. Textile, olive mills and rubber industries supplied wastewater for MD studies [34]. Wastewater application was the third most published area for MD after 1991. It became a more preferred application for MD studies during the growth phase for membrane distillation publications. Fig. 2.6 shows studies on different application areas for MD that have been published [5].

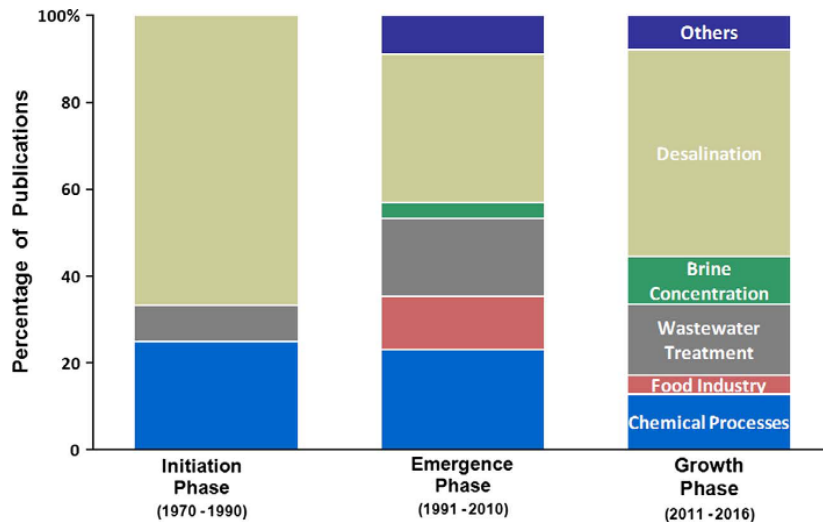


Figure 2.6. Distribution of publications due to different MD applications during three phases [5]

2.7. Membranes Used in Membrane Distillation

MD membranes are hydrophobic, porous, polymeric media [15]. The ideal membrane should have high energy efficiency as well as high flux. The functioning of the membranes depends on their structure, since it is related to the separation mechanism. There are 2 types of membrane structures: symmetric and asymmetric. Fig 2.7. depicts different structures adopted by membranes [37, 38].

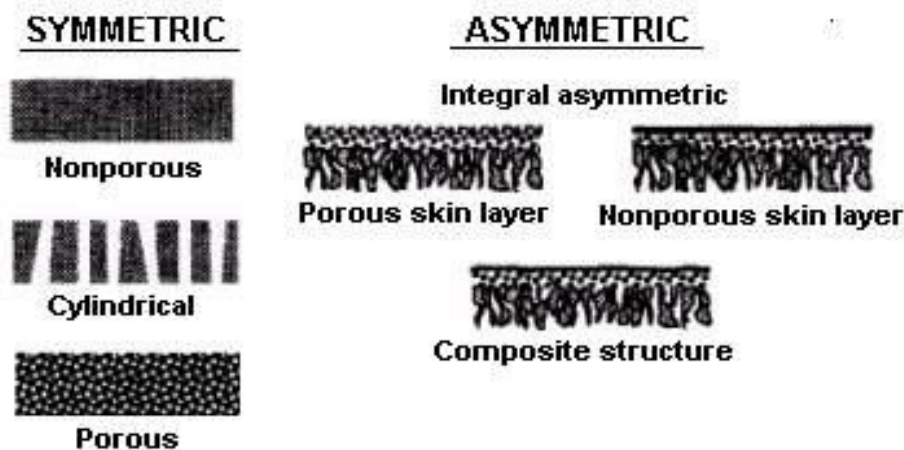


Figure 2.7. Membrane structure classification [37]

Polymers, ceramic, carbon, metal and glass can be used as membrane materials; however, the most popular membrane materials are polymeric [39]. The most suitable polymeric

membrane materials are PTFE, PP and PVDF for carrying the necessary requirements for performance. Those necessities are porous, hydrophobic, narrow pore size distribution, and small tortuosity factor. However, these membranes were initially manufactured for use in microfiltration (MF) process [40]. Only commercial MF membranes were used for MD between the years of 1970 and 1990. Fabrication of specific MD membranes by surface modification, grafting and blending methods have been popularly used in academic study after 2011. Specific MD membranes promised to decrease wetting and fouling, as well as to enhance flux [5, 41]. This can be done by controlling the MD membrane properties, such as porosity, mean pore size, hydrophobicity etc. [5]. Polymer membranes can be fabricated by phase-inversion method [39]. Membrane materials should be thermally and chemically stable for bearing process conditions. Table 2.3 shows the most common polymeric MD membrane materials and their properties [11, 39].

Table 2.3. Polymeric materials and their properties

Polymeric Materials	Properties
Polyethersulfone (PES)	Chemical and thermal durability
Polyacrylonitrile (PAN)	Extreme resistance to oxidation and hydrolysis Main material for UF membrane and composite membranes Better tolerance to solvents Good organic fouling resistance Often hydrophilic material (not desirable for MD)
Polysulfone (PS)	High performance polymer with excellent chemical and thermal stability Common material for UF and MF membranes
Polyetherimide (PEI)	Good material for asymmetric pervaporation membranes
Polyvinylidene fluoride (PVDF)	Good chemical and thermal resistance

	Resistant to organic and inorganic acids High pH tolerance
Polyethylene (PE)	Excellent mechanical strength Non-toxic Low cost
Polypropylene (PP)	Generally hydrophobic High chemical stability Cheaper than PTFE membrane
Polytetrafluoroethylene (PTFE)	Hydrophobic by nature High resistance to chemicals

Membrane hydrophobicity increases for the materials listed in Table 2.3, as one moves down the rows from PES to PTFE. Polysulfone (PS), polyethersulfone (PES), polyacrylonitrile (PAN) and polyvinylidene fluoride (PVDF) polymers are hydrophobic by nature, however with different methods and additives they can be modified to be hydrophilic membranes [39]. Table 2.4 lists the most used polymeric membrane materials, and describes their key material attributes of relevance to membrane separation processes.

Membranes can be prepared by two main processes, which are phase-inversion process and interfacial polymerization process. These processes can be used for commercial membrane productions [39], although interfacial polymerisation is used for manufacture of dense membranes. Several separation mechanisms can be used to induce membrane formation via phase inversion, and the two most common methods are thermally induced phase separation (TIPS) and non-solvent induced phase separation (NIPS) [39]. Thermally induced phase separation (TIPS) is one of the mainly used microporous membrane preparation methods. PVDF membranes can be prepared by this method, while non-solvent induced phase separation method (NIPS) is used to prepare PS, PES, PAN and PVDF membranes [39].

For MD, the most common membrane type used is single layer hydrophobic membrane. Nevertheless, other types of membranes are also used such as dual layer composite hydrophobic/hydrophilic membranes, trilayer hydrophilic/hydrophobic/hydrophilic

membranes, and hydrophobic/hydrophilic/hydrophobic membranes [11]. Table 2.4 lists, flat sheet membranes specifically used for MD as well as their membrane characteristics [11, 40].

Table 2.4. Common flat sheet commercial membranes used in MD

Material	Membrane Trade Name	Manufacturer	Thickness (µm)	Mean Pore Size (µm)	Porosity (%)
PTFE	Gore	Gore	64	0.2	90
PTFE	Gore	Gore	77	0.45	89
PTFE	Sartorius	Sartorius	70	0.2	70
PP	Enka	Sartorius	100	0.1	75
PP	Metricel	Gelman	90	0.1	55
PP	PP22	Osmonics Corp	150	0.22	70
PVDF	GVHP	Millipore	110	0.22	75

2.8. Performance of Single and Dual Layer Membranes

Direct contact membrane distillation modelling is based on heat and mass transfer analysis of the process and the membrane characteristics. Heat and mass transfer analysis of the process is able to predict permeate flux, heat and mass transfer coefficients, heat and mass transfer resistances, and energy efficiency, as well as temperature and concentration polarization coefficients [42]. Models have incorporated the effect of membrane characteristics, such as membrane porosity, thickness and pore size distribution on membrane distillation performance [43]. In [44], performance modelling for composite membranes was investigated, which showed that increases of surface porosity and feed temperature also increased MD performance and permeate flux. Membranes with different characteristics have been investigated to understand mass transport so as to enhance MD performance [45]. Previous works on theoretical models for MD have required at least one adjustment factor, such as pore tortuosity to predict permeate flux [45].

The thermal efficiency can be calculated from the ratio of flux (J) and latent heat transfer (h_{latent}) to mass flux (\dot{m}_f), specific heat capacity (C_p) and temperature difference between bulk temperature (T_{fi}) inlet and bulk temperature outlet (T_{fo}) as described by Eq. 4.1 [46, 47].

$$\text{Energy efficiency} = EE = \frac{Jh_{latent}A}{\dot{m}_f C_p (T_{fi} - T_{fo})} \times 100 \quad (4.1)$$

Flux can be calculated from the change of the permeate weight (ΔW) to change of time (t) and the area of the membrane (A) [48].

$$\text{Flux} = J = \frac{\Delta W}{\Delta t A} \quad (4.2)$$

One of the objectives in terms of increasing the performance of MD is to increase the energy efficiency. Table 2.5 lists published information for membrane characteristics and performance for dual layer and single layer membranes.

Table 2.5. Studies on MD membranes and their characteristics for dual layer membranes and hydrophobic membranes

Reference	MD process	Membrane type	Fabrication	Thickness (μm)	Pore size	Porosity	Rejection and Permeability
Dual Layer Membranes							
[49]	DCMD	Polyelectrolyte Hydrogel on composite Polypropylene flat sheet membrane	UV-initiated graft polymerization	170 ($\approx 35 \mu\text{m}$ -thick gel layer (in the dry state))	200 nm (PP)	70% (PP)	99.09% (For 30 gL ⁻¹ NaCl feed solution) 7.4 kg/m ² h
[13]	DCMD	Surface modifying macromolecules (SMM) blended Polyetherimide (PEI) membranes	Phase inversion method	50.92	22.86 nm	19.21% (Hydrophobic top-layer) 17.63% (Hydrophilic sub-layer)	>99.7% 21 kg/m ² hr with 12% PEI concentration (M12 membrane)
[43]	DCMD	Hydrophobic surface modifying macromolecules (SMMs) blended	Phase inversion method				>99.9 % M4 flux (1×10^{-6}) is lower than commercial PTFE

		hydrophilic polysulfone (PS)					membrane (1.8×10^{-6} m/s) M1 flux (2.7×10^{-6}) is higher than commercial PTFE membrane
[50]	DCMD	PTFE/PU Compound membrane	Co-stretching method	30 (PU layer)	382 nm	78%	3.88 kg/m ² hr
[51]	DCMD	Dual layer composite flat-sheet PVDF membranes	Phase inversion method	71 (top-layer) 44 (bottom layer)	95 nm	70.6±3.8 %	99.8 % 10.4 ± 0.4 kg/m ² hr (M1)
Single Layer Membranes							
[52]	DCMD	Thermally induced phase separation (TIPS)- made polyethylene (PE) flat sheet membrane	Commercial	45±3.2	0.06±0.03 μm	56.5±5.5%	25 kg/(m ² h)

[53]	DCMD	Commercial polytetrafluoroethylene (PTFE) flat sheet membrane	Commercial	36±1	0.45±0.05 (μm)	94±0.5%	29 kg/(m ² h)
[44]	DCMD	PTFE/PP composite membrane	Commercial	20 ± 0.4 (PTFE) 80 ± 1.6 (PP)	0.5 ± 0.02 (PTFE) 0.1 ± 0.004 (PP)	70% ± 5.0 (PTFE) 34% ± 2.4 (PP)	40 kg/(m ² h)
[46]	DCMD	Commercial polytetrafluoroethylene (PTFE) flat sheet membrane	Commercial (Membrane Solutions)	215 (active + support layer) 30 (active layer)	1.00 (μm)	92.9%	25.5 kg/(m ² h)
[54]	DCMD	Commercial polypropylene (PP) flat sheet membrane	Commercial (GE Osmonics)	150	0.22	70%	28 kg/(m ² h)

Table 2.5 shows some membrane types and their relation to membrane characteristics in order to achieve higher flux for desalination. This can be used as a guide to follow how membrane characteristics can be effective for membrane distillation performance in terms of obtaining higher flux. According to the study in [55], dual layer hydrophobic/hydrophilic membrane design requires thinner and larger pores for the hydrophilic sub-layer than the hydrophobic top-layer. Another study in [56] states that the top hydrophobic layer characteristics, that are mean pore size, LEP, and effective porosity have influential effect on MD permeate flux.

More recently, Qtaishat et al. [3] used hydrophobic/hydrophilic composite membranes for membrane distillation and analysed performance in terms of physically understanding the MD process [13]. Qtaishat et al. [3] prepared novel composite MD membranes by combining hydrophilic polysulfone and coating with hydrophobic surface modifying macromolecules (SMMs). Three types of SMMs were used, such as MDI (diisocyanate 4,4'-methylene bis (p-phenyl isocyanate)), PDMS (α,ω -Aminopropyl poly (dimethyl siloxane)) and BA-L (2-(perfluoroalkyl) ethanol). These three different types of SMMs were tested and better DCMD fluxes than those of hydrophobic single layer polytetrafluoroethylene (PTFE) membranes were obtained [43]. Energy efficiency for non-woven supported PTFE flat sheet microfiltration composite membrane reached a maximum of 50% at 70°C, and flux reached highest at 46 L/m²h at 80°C in DCMD [46]. For DCMD, with hollow fiber asymmetric hydrophilic polyethersulfone (PES) membrane, energy efficiency reached 76% with the feed temperature at 74.5° C [57]. Hydrophilic asymmetric PES flat sheet and hollow fiber membranes performed with high flux up to 66.7 kg/m²h at a feed temperature of 73.9° C for 2 m/s and 0.68 m/s flow rates, respectively, for feed and permeate. Another study demonstrated 58% energy efficiency with PVDF hollow fiber membrane at 72° C feed inlet temperature [58].

The aforementioned studies showed that membranes with dual layers can increase permeate flux and energy efficiency for MD. Hydrophobic/hydrophilic dual layer membrane performances in DCMD depends upon the characteristics of the hydrophobic and hydrophilic layers, and these need to be characterised for modelling programs. In the fabrication process of blending of the composite dual layer membranes, solution concentrations also play vital role in determining membrane characteristics that in terms effect MD performance [10].

2.9. Mathematical Modelling in Membrane Distillation

Different types of theoretical models have been proposed for various MD configurations. The main focus of the models is performance modelling of MD for different process conditions [34]. Several studies focused on heat and mass transfer mechanism modelling in DCMD [59]. Different approaches to solving the equations have also been used, such as analytical resistance network models and numerical modelling to model DCMD process. In [60], modelling has been divided into three categories; 2 sub-models to

describe the flow regime on the feed and permeate side and 1 sub-model for vapour transport through the membrane that is dependent upon membrane properties.

For modelling, variations in membrane materials are accounted for in the membrane characteristics included in the equations for heat and mass transfer, which will be discussed in Chapter 5 in detail.

2.9.1. Modelling of hydrophobic single layer membranes

Prediction of flux has been done for PTFE membrane in DCMD mode [21] with different parameters taken into account as model variables, such as velocity, feed temperature and module length. Process performance was predicted with derived heat and mass transfer coefficients at different feed inlet temperatures. Moreover, accuracy was observed between experimental and modelling results for counter-current and co-current flow while predicting the relationship between membrane length and temperature. A 1-D model was developed for predicting the feed and permeate temperatures, mass flux and outlet feed salinity for AGMD with co-current and counter-current flow [61]. Modelling also was used to do a simple cost analysis for the process to examine how much energy is required for AGMD using flat sheet membranes. Different feed water temperatures, feed salinity and membrane pore sizes as well as different air gap widths were considered. The error for the model prediction was within 10%. Work by [62] used performance modelling and flux prediction as well as experiments to demonstrate that for hollow fibre DCMD permeate flow rate does not affect the permeate flux significantly compared to the effect of feed temperature increase. However, the tortuosity factor influenced the result when comparing the experimental results with the model. Nevertheless, the study found good correlation between the model and experiments. Feed inlet temperature effect on permeate flux was correlated in the work and also achieved good agreement between experimental results and modelling work. Another study modelled the compression of PTFE membrane and its effects on permeate flux and energy efficiency [63, 64]. Moreover, the model was consistent with experimental results for predicting the flux at different pressures. A two dimensional model was developed by [65] to understand mass and heat transfer mechanisms throughout membrane models in DCMD. Flat sheet hydrophobic PTFE membrane for DCMD was modelled and parameters investigated the impact of different velocities and feed temperatures [66]. Also, the model was verified with the experimental results by deriving the heat and mass transfer coefficients to predict

the flux. Composite PTFE/PP hydrophobic membrane was modelled, and included mass, momentum, and energy balances in [44]. The result showed that increasing the feed inlet temperature both increased the model and experiment permeate flux. Additionally, model results were compared with experimental results for validation of the model. 2-D model as presented by [67] and considered X and Y flow modes with commercial PTFE membrane at different velocities and feed temperatures. The modelling result was in agreement with the experimental result. Another 2-D model was used to model DCMD performance using different membranes at different process conditions for desalination using solar energy [8].

Most of the modelling work in literature has been performed for AGMD rather than DCMD. Both 1-D and 2-D models have been used to predict the MD permeate flux and to model the performance. The reason for using the 2-D model was to see the effects of flow in the axial direction as well as the longitudinal direction, which influences heat and mass transfer outcomes. However, 2-D computational fluid dynamics models also have computational burdens and so are generally only used when mass and heat flows do not distribute uniformly across the membrane [68]. When it comes to modelling hydrophobic single layer membranes, different studies have shown accuracy between models and experiments, and most studies have focused on AGMD for desalination.

2.9.2. Modelling of hydrophobic/hydrophilic dual layer membranes

The first modelling work on hydrophobic/hydrophilic dual layer membranes was done by [10]. The study tested the model to observe membrane top and sub layer characteristics by simulating the permeate flux in DCMD. Qtaishat et al. [13], used hydrophobic/hydrophilic composite membranes in their study in which the heat transfer differed compared to hydrophobic membranes. The heat transfer was calculated by considering fluxes through the hydrophobic top-layer and hydrophilic sub-layer. Therefore, the heat flux through the membrane matrix was divided into two sections: hydrophobic top-layer and hydrophilic sub-layer [10]. The diagram of heat and mass transfer for hydrophobic/hydrophilic dual layer membranes can be seen in Fig. 2.8.

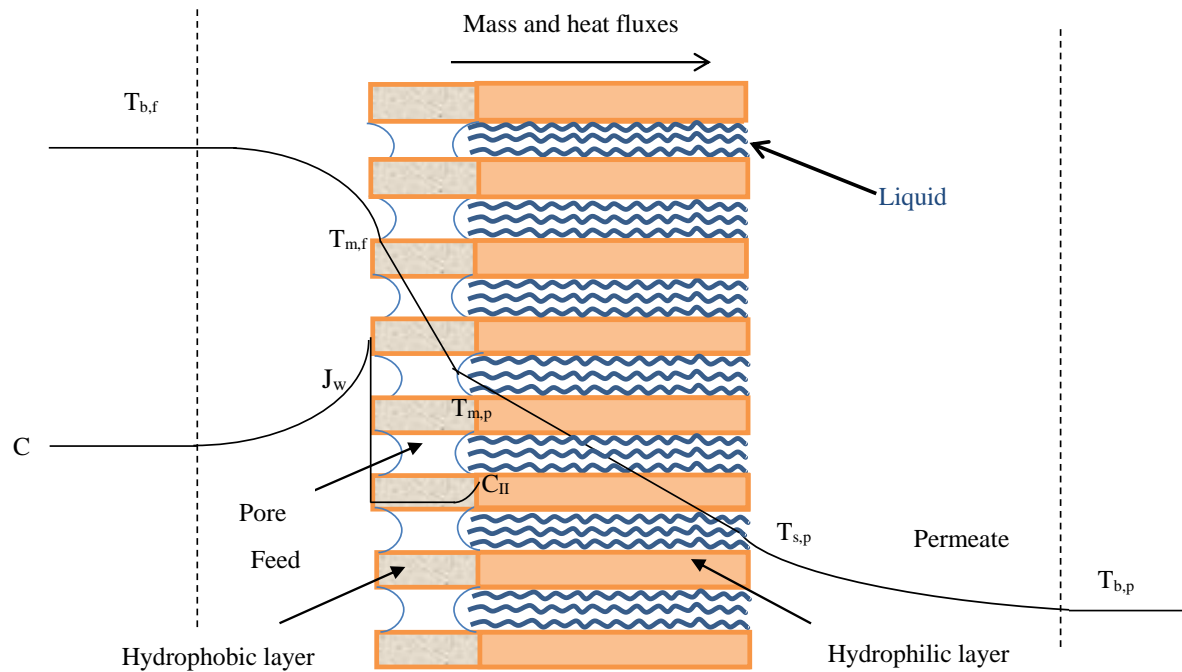


Figure 2.8. Diagram of the temperature and concentration profile through a hydrophobic/hydrophilic dual layer membrane

Deviation was observed for hydrophobic/hydrophilic hollow fiber membranes between modelling and experimental results because of the influence of an additional hydrophilic layer on permeate flux [69]. Another study examined the effect of the hydrophilic layer's thermal conductivity on permeate flux for hollow fiber composite membranes with co-current flow while excluding the counter-current flow to prevent membrane wetting [70]. Increasing the thermal conductivity of the hydrophilic layer improved the permeate flux. The model prediction was accurate with the experimental result. However, increment trend changed after thermal conductivity of the hydrophilic layer reached a certain high level due to temperature polarization, and limited temperature difference across hydrophilic layer of the membrane.

2.10. Objectives

Due to lack of modelling work around dual layer hydrophilic/hydrophobic membranes, this work's focus is to undertake modelling of dual layer composite membranes and to predict permeate flux of MD. Although some modelling studies are available for

hydrophobic/hydrophilic dual layer membranes, few predicted MD flux and energy efficiency and most are just conceptual models that describe the concept of dual layer membranes and how membrane characteristics effect performance. The studies with those conceptual models showed that hydrophobic/hydrophilic dual layer membranes can improve permeate flux and energy efficiency in MD. This hypothesis will be tested by performance modelling using 1-D model.

The aim is to predict MD performance and to account for differences between MD membranes based on their characteristics. To address this issue, heat and mass transfer equations are derived for hydrophilic/hydrophobic dual layer membranes, which can be found in the Chapter 5. Those equations were gathered from previous studies. Most of the modelling works were also focused on Air Gap Membrane Distillation (AGMD) and hollow fiber membranes. However, this study will focus on flat sheet, DCMD performance modelling.

The research objective of this study is to model and compare single layer hydrophobic and dual layer hydrophobic/hydrophilic membranes in order to observe their performance and to predict the flux and energy efficiency for DCMD. This work also includes sub-objectives that support the main objective, and these are:

- ❖ To derive heat and mass transfer equations for both hydrophobic single layer membranes and hydrophobic/hydrophilic dual layer membranes,
- ❖ To characterize hydrophobic and hydrophobic/hydrophilic membranes to gather parameters, that are important inputs to the mathematical model,
- ❖ To work at different process conditions to examine the effects of conditions on MD performance, and,
- ❖ To validate the model with experimental data while predicting the MD permeate flux and energy efficiency at different process conditions.

CHAPTER 3. EXAMINATION OF CHARACTERIZATION TESTS FOR SINGLE LAYER AND DUAL LAYER MEMBRANES

3.1. Introduction

Membrane distillation process performance depends on membrane properties. Membrane properties can be measured by characterization tests for different membrane parameters, so that membrane properties can be related to MD performance [11]. The properties of interest are thickness, pore size, porosity, tortuosity, Liquid Entry Pressure (LEP) and membrane thermal conductivity. Membranes have different characteristic properties, which need to be identified carefully in order to model the membrane performance with high accuracy. Membrane properties affect the MD flux according to Equation 3.1. Increasing membrane pore size and porosity increases MD flux, however, increasing thickness and membrane tortuosity decreases the flux.

$$N \propto \frac{r \varepsilon}{\delta \tau} \quad (3.1)$$

where N is the molar flux, r is the mean pore size of the membrane, ε is the membrane porosity, δ is the membrane thickness and τ is the tortuosity of the membrane [34].

Characteristics of the membranes can be divided in two different groups: those related to membrane permeation such as liquid and gas flow tests, and those related to the morphology and chemistry of the membranes such as scanning electron microscopy (SEM), and Fourier – transform infrared (FTIR) spectroscopy [11].

Requirements for membranes to obtain better MD performance are listed below [1, 11, 30]:

- 1- Membranes should have thermal stability, being durable under high process temperatures.
- 2- High LEP for membranes, to prevent wetting
- 3- Low thickness and tortuosity reduces mass transfer resistance, but high membrane thickness increases thermal resistance of the membrane to prevent heat loss.
- 4- Narrow pore size distribution, to lower the risk of maximum pore size wetting, so that membrane rejection can increase.

5- High porosity, MD permeability and thermal resistance can increase that leads to increase in MD flux and thermal efficiency.

6- Membrane should have larger pore size to reduce mass transfer resistance.

3.2.Experimental and Methods

3.2.1. Membrane types

Five different membranes were considered in this study and these are presented in Table 3.1. Three different single layer membranes were considered, one with an oleophobic layer (O-PE). Additionally, 2 dual layer membranes were considered, one that had a hydrophobic layer facing the feed (HFP-co-PVDF-N6) and the other a hydrophilic layer facing the feed (PU-PTFE).

Table 3.1. Membrane codes and their compositions

Membrane	Membrane code	Membrane Composition
PTFE	M1	PTFE active layer and PP support layer
PE	M2	Symmetric Polyethylene
O-PE	M3	Symmetric oleophobic Polyethylene
PU-PTFE	M4	Polyurethane coated PTFE
PVDF-co-HFP-N6	M5	Electrospun PH active top layer on Nylon-6 support layer

3.2.2. FTIR spectroscopy analysis

The bulk and skin layer functional groups of the membrane were obtained by FTIR analysis (Perkin Elmer Frontier) [11]. Moreover, membranes were analysed in their dry state to prevent water interference of the signals. Membrane samples were put in the sample loading area, the so-called FTIR diamond plate. Before starting the analysis, the diamond plate was cleaned with ethanol to reduce the risk of contamination. The spectrum range was between 650 and 4000 cm^{-1} . Fingerprint region is known as the area for peaks was between 2000 and 650 cm^{-1} on the FT-IR graphs. Identification of chemical functional groups was made by comparison with reference spectrum peak ranges.

3.2.3. Liquid entry pressure (LEP) measurement

The Liquid Entry Pressure (LEP) is the pressure above which water is able to enter the membrane pores and permeate through the largest pores of the membrane. LEP is an indicator of likely membrane wetting, as water enters the pores when the pressure difference across the membrane is greater than the LEP [1, 71].

$$\Delta P = P_f - P_p \quad (3.2)$$

$$\text{LEP} = \frac{-2B\gamma_1}{r_{\max}} \cos \theta \quad (3.3)$$

where B is the geometric pore coefficient [20], which is equal to 1 for cylindrical pores, P_f is the interfacial pressure on the feed side, P_p is the interfacial pressure on the permeate side, r_{\max} is the maximum pore size, γ_1 is the surface tension of the liquid, and θ is the contact angle of the membrane [46]. The test was run by gradually increasing the pressure drop across the membrane of interest, that was held in membrane holder with 20% NaCl on the high-pressure side and deionised water on the permeate side. When the applied pressure on the salt solution exceeded the LEP, the salt solution was forced through the membrane and a change in conductivity was detected on the permeate side. Fig. 3.1 shows the schematic set-up for LEP test [1].

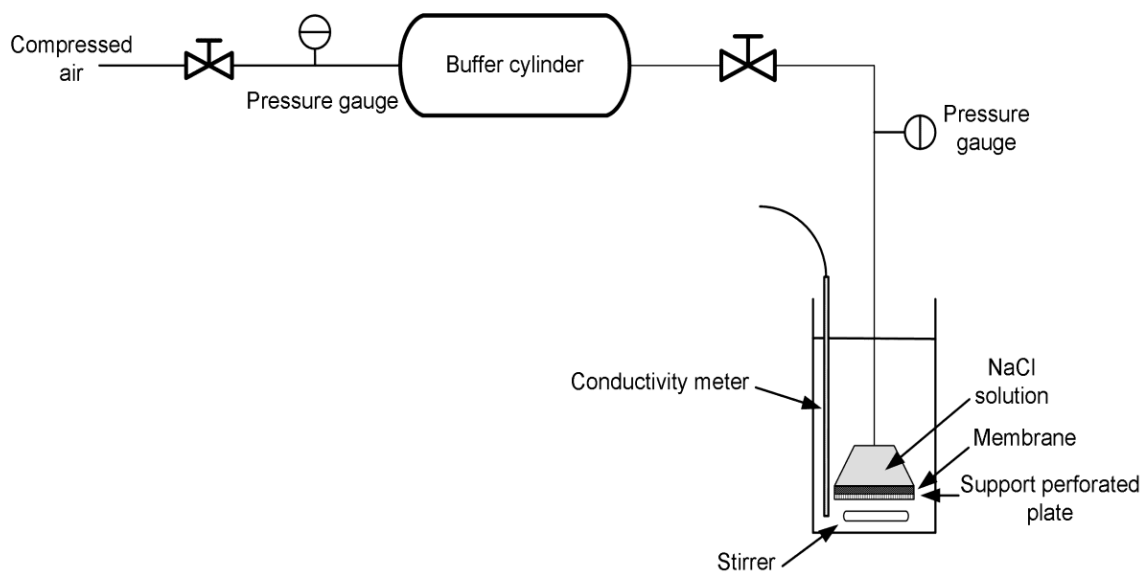


Figure 3.1. Set-up for LEP test [1]

3.2.4. Contact angle measurement

Contact Angle Analyser Kruss DSA25 was used to determine the contact angle of the membrane material, and is a measure of the extent of hydrophobicity [1]. It is one of the vital parts of membrane characterization as it is also used to calculate the Liquid Entry pressure (LEP). Contact angle was measured by the sessile drop method. A syringe was used to place a 4 μl drop on the membrane surface. The angle between the air-water interface and the membrane surface measured through the water phase is defined as the contact angle, and was determined by imaging of the drop on the membrane surface. Contact angle measurements were performed for all membranes used in this study, and the results can be found in Table 3.2. The results reported are the mean of 2 replicate measurements. Contact angle measurements for dual layer membrane were taken by testing both sides of the membrane to characterise both the hydrophilic and hydrophobic layers.

3.2.5. Porosity measurement

Porosity was measured by mass difference of a dry and wet membrane by using water and acetone. Water was used as liquid for porosity to determine the membrane support layer volume so that membrane active layer volume could be found, as water does not enter the pores of hydrophobic membranes. Acetone was used to calculate the solid membrane volume, as it wets the membrane surface and can enter the pores. Membrane

samples were cut into small pieces (5 cm×3 cm), and membranes were separated as active layer and support layer, and the active layer volume (V_a), the support layer volume ($V_{support}$), the masses of the membrane and its support layer were measured [1, 72], and the porosity was determined as follows.

$$V_{support} = \frac{m_{support}}{\rho_{support}} \quad (3.6)$$

$$V_m - V_a = V_{support} \quad (3.7)$$

where V_m is the whole membrane volume and $\rho_{support}$ is the support layer's density. Eq. 3.6 and Eq. 3.7 were used to calculate the membrane porosity.

$$\varepsilon = 1 - \frac{(m_{total} - m_{support})/\rho}{(V_m - V_{support})} \quad (3.8)$$

where ε is the porosity, m_{total} is the membrane with support and active layer, $m_{support}$ is the support layer mass, and ρ is the membrane density.

To calculate the density of the membrane, the active layer of the membrane was soaked in acetone in 50 ml flask, air bubbles were removed from the flask by using an ultrasonic vibrator. The membrane active layer mass and flask mass were measured by balance. The density of the active layer can be calculated [72] from:

$$\rho_{active\ layer} = \frac{m_{active\ layer}}{V_{flask} - \left(\frac{m_{acetone+membrane} - m_{active\ layer}}{\rho_{acetone}} \right)} \quad (3.9)$$

where $m_{active\ layer}$ is the active layer mass, V_{flask} is the volume of the volumetric flask, $m_{acetone+membrane}$ is the total mass of the acetone and membrane in the volumetric flask.

The same method was also used for dual layer membranes. For dual layer membrane, the membrane layers were separated, and the porosity of both membrane layers were determined.

3.2.6. Pore size measurement

3.2.6.1. Gas permeation test

The aims for using the gas permeation test were to calculate mean pore size and effective porosity [73]. The experimental set-up for measuring gas permeability consists of

manometer, flow meter and membrane holder. There are two different pressure readings which are the pressure difference across the membrane, that was set at 1 ± 0.1 kPa, and the absolute pressure, which was varied between 5-80 kPa [1]. Gas permeation through the membrane was calculated by Knudsen diffusion – Poiseuille flow mechanism from Eq. 3.3 [1].

$$J = \left(\frac{8r\varepsilon}{3tb} \sqrt{\frac{1}{2\pi RMT}} + \frac{r^2\varepsilon}{8RTtb\mu} P_{pore} \right) \Delta P_{gas} \quad (3.3)$$

where R is the gas constant, μ is the gas viscosity and ΔP is the pressure difference across the membrane. From Eq. 3.3., by keeping the ΔP_{gas} constant while varying the P_{pore} , a straight line can be fitted to the relationship between $J/\Delta P_{gas}$ versus P_{pore} from which slope (k) and intercept (c) can be obtained. These terms can then be related to membranes properties by Eqs. 3.4 and 3.5.

$$k = \frac{r^2\varepsilon}{8RTtb\mu} \quad (3.4)$$

$$c = \frac{8r\varepsilon}{3tb} \sqrt{\frac{1}{2\pi RMT}} \quad (3.5)$$

Mean pore size (r) and effective porosity (ε/bt) can be derived from Eq. 3.6 and Eq. 3.7 as:

$$r = \frac{16k\eta}{3c} \sqrt{\frac{8RT}{\pi M}} \quad (3.6)$$

$$\frac{\varepsilon}{tb} = \frac{8RT\eta k}{r^2} \quad (3.7)$$

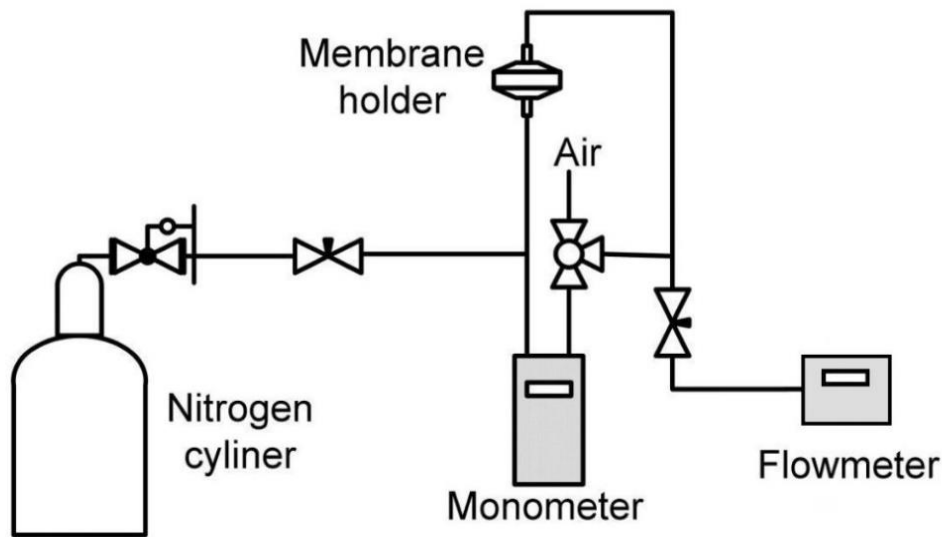


Figure 3.2. Gas permeability measurement experimental set-up

3.2.6.2. Porometer (Wet/Dry Run Method)

Another method for determining the mean pore size, maximum pore size, minimum pore size and pore size distribution is wet/dry flow method, which can be measured by Porometer Quantachrome 3GZ. The porometer measures air flow as a function of pressure through the membrane [74]. Wet run and dry run were conducted consecutively. The membrane was wetted with isopropyl alcohol (IPA) that has low surface tension. The liquid fills the pores of the membrane, and a gas permeation test was conducted by increasing the transmembrane pressure. The transmembrane pressure is expected not to be linear because of the flooded membrane pores by IPA. During the wet run, when the transmembrane pressure overcomes the surface tension of the liquid, it will push the liquid out of the pores. The dry run was conducted with the same range of pressure [75]. A dry run was measured by sending the gas through holder and measuring gas flow as a function of pressure. When plotted as flowrate versus pressure difference a straight line is drawn until it finds the intersection of wet and dry run in order to find the smallest pore size of the membrane [75].

$$D = \frac{4\gamma\cos\theta}{P_{capillary}} \quad (3.8)$$

where γ is surface tension of the liquid, θ is the contact angle of the liquid, P is the capillary pressure. When IPA is applied, $\cos\theta$ is equal to 1.

The bubble point corresponds to the membrane's largest pore once it overcomes the pressure [75]. Then, bubble point pressure and bubble point flow rate can be recorded by Porometer. Pore size distribution is relating a diameter, which meets each pressure points by Eq. 3.8 [76]. Pore size distribution graph revealed the minimum, maximum and mean pore sizes of the membranes.

3.2.7. SEM measurement (Thickness)

SEM (Zeiss Merlin Gemini 2 Field Emission Scanning Electron Microscopy) characterization was used to measure the thickness of the membrane, and to observe the cross-section morphology of the membrane. The membrane was frozen in liquid nitrogen and then the membrane was cut with a blade to expose a clean cross section. The membrane samples were sputtered with Iridium prior to the characterization. SEM measurement can be also used for estimating surface porosity, pore size as well as pore size distribution using image analysis [20]. This method was repeated for single and dual layer membranes to see their surface and cross sections, so that the membrane layer thicknesses could be measured.

3.3. Results and Discussion

3.3.1. Membrane properties

Table 3.2 shows the membrane characteristics of all membranes that were used in this study. Besides characterising the thickness for M4, the other characterization results were gathered from a previous study [77]. Characteristics of the membranes were used in the modelling program in order to calculate mass transfer and conductive heat transfer coefficients for the membranes.

Table 3.2. Membrane Characteristics

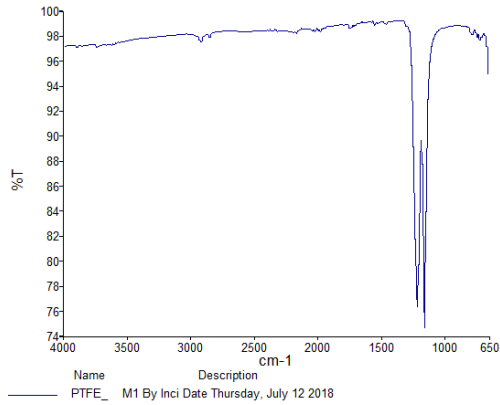
Membrane Codes	LEP (kPa)	Porosity (%)	Contact Angle (°)	Maximum Pore Size (µm)	Mean Pore Size (µm)	Thickness (µm)

M1	140	93	125	0.82	0.51	6.6 (active layer) 86 (support layer)
M2	93	75	101	0.39	0.21	14.3
M3	63	62	109	0.37	0.19	33.3
M4	90.5	-	77 (Hydrophilic layer) 104 (Hydrophobic layer)	0.45*	0.36*	11 (Hydrophilic PU layer) 18 (Hydrophobic layer)
M5	-	91 (Hydrophilic layer) 81 (Hydrophobic layer)	50 (Hydrophilic layer) 111 (Hydrophobic layer)	0.39 (Hydrophobic layer) 0.44 (Hydrophilic layer)	0.31 (Hydrophobic layer) 0.25 (hydrophilic layer)	93.9 (Hydrophobic layer) 13.6 (Hydrophilic layer)

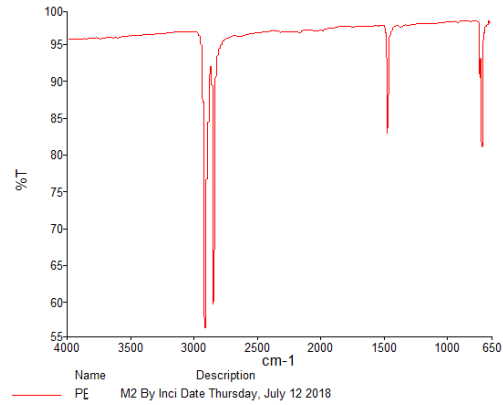
*Taken from Zhang et al. [77]

FT-IR spectra of the 5 membranes can be seen in Fig. 3.3. M1 membrane gave a peak at 1204.09 and 1109.87 cm^{-1} in Fig. 3.3a related to its C-F bonds. When Fig. 3.3b and Fig. 3.3c images were examined, C-H bonding gave identical peaks between PE and oleophobic coated PE. Both images had CH_2 stretch around 2900 cm^{-1} and CH_2 bend 1450 cm^{-1} . However, the C-C bonding peaks showed a difference in fingerprint region. Hydrophobic layer of M5 membrane can be defined as PVDF-co-HFP (PH) in Fig. 3.3e.

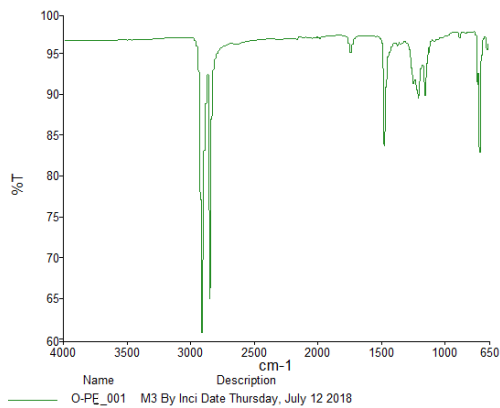
Hydrophilic layer of the dual layer membrane M5 was identified as Nylon-6 due to amide I and amide II peaks and around 1600 and 1500 wavelength respectively from Fig. 3.3f. N-H bonding was also observed for Fig. 3.3f. Peaks at around 3000 cm^{-1} showed C-H bonding for Fig. 3.3d. Peak between the range of 2000 cm^{-1} and 1500 cm^{-1} was the indicator of the existence of polyurethane (PU).



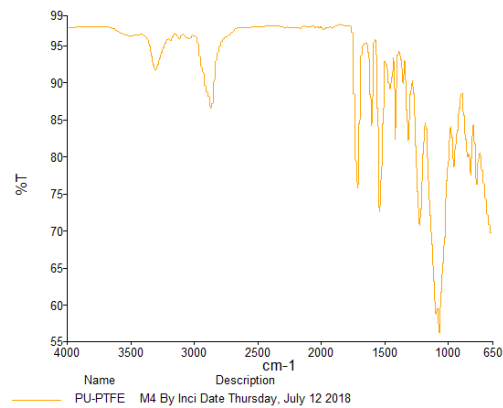
(a)



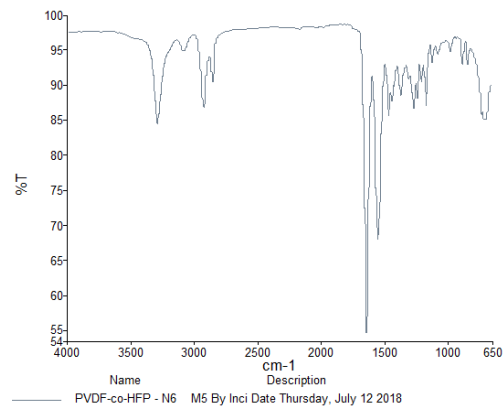
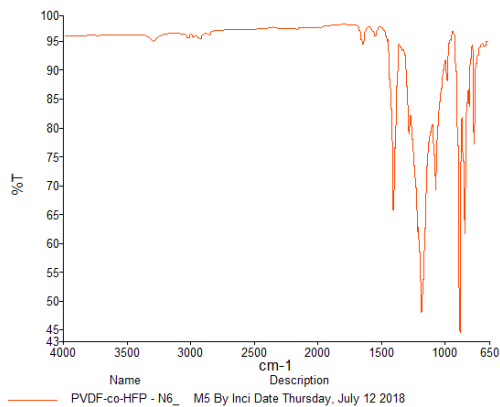
(b)



(c)



(d)

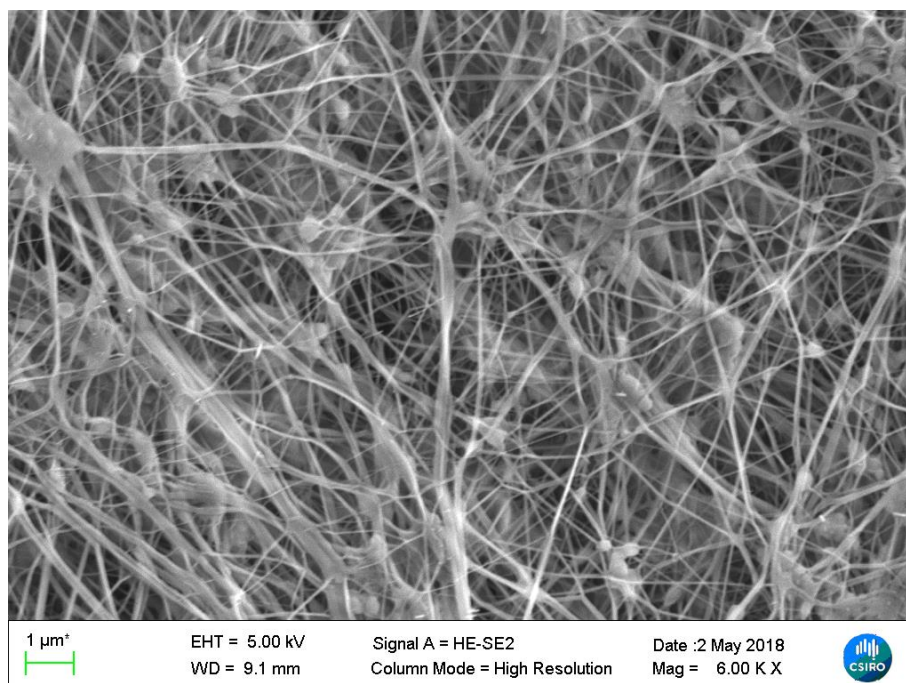


(e)

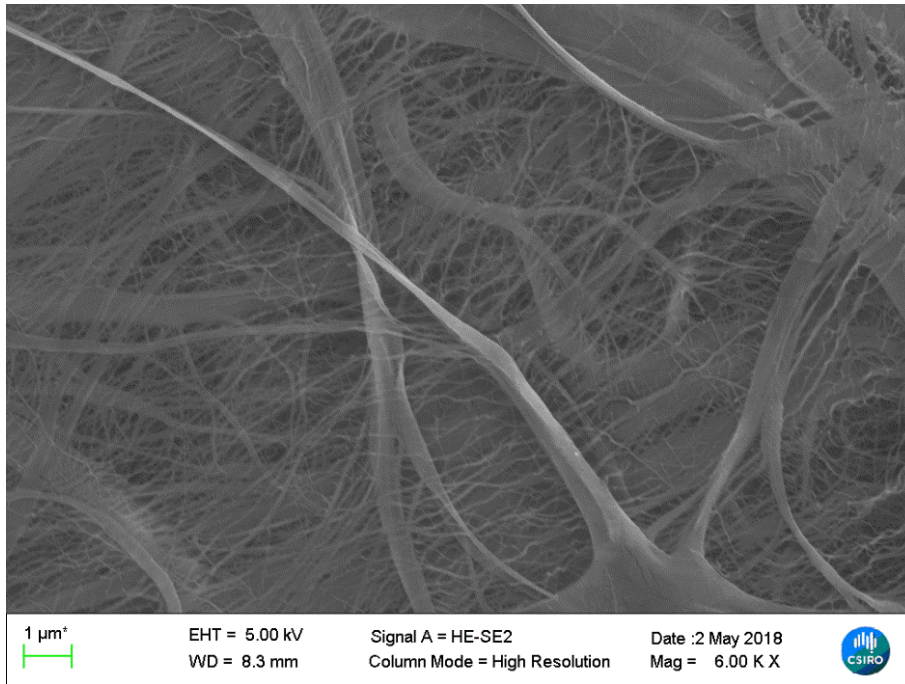
(f)

Figure 3.3. FT-IR images of membranes (a) M1 (b) M2 (c) M3 (d) M4 (e) M5 hydrophobic layer (f) M5 hydrophilic layer

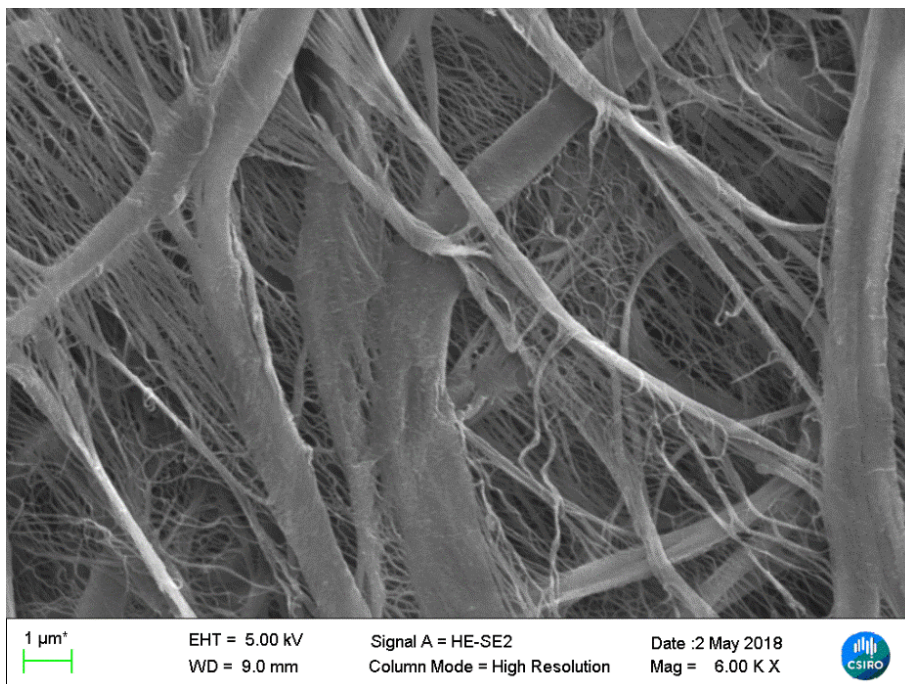
Fig. 3.4. illustrates the images from SEM for membrane surfaces. The surface images demonstrate surface porosities. From Fig. 3.4b and Fig. 3.4c, the surface structures of membrane M2 and M3 can be seen to be relatively similar to each other. According to Fig. 3.4a and Fig.3.4e, M1 and M5 membrane surfaces, membrane surface porosities can be judged as high. It is clear to declare from Fig.3.4d and Fig.3.4e that comparison between hydrophobic and hydrophilic layers of M5 membrane can be done regarding their surfaces, so that pore size of hydrophilic layer seems to be higher than the pore size of hydrophobic layer. As can be seen from Fig. 3.4a and 3.4e, the surfaces of M1 and M5 hydrophilic support layers were highly porous. PU hydrophilic layer coating on PTFE hydrophobic layer of membrane M4 is a dense coating. The dense PU hydrophilic layer surface was shown in Fig. 3.4d.



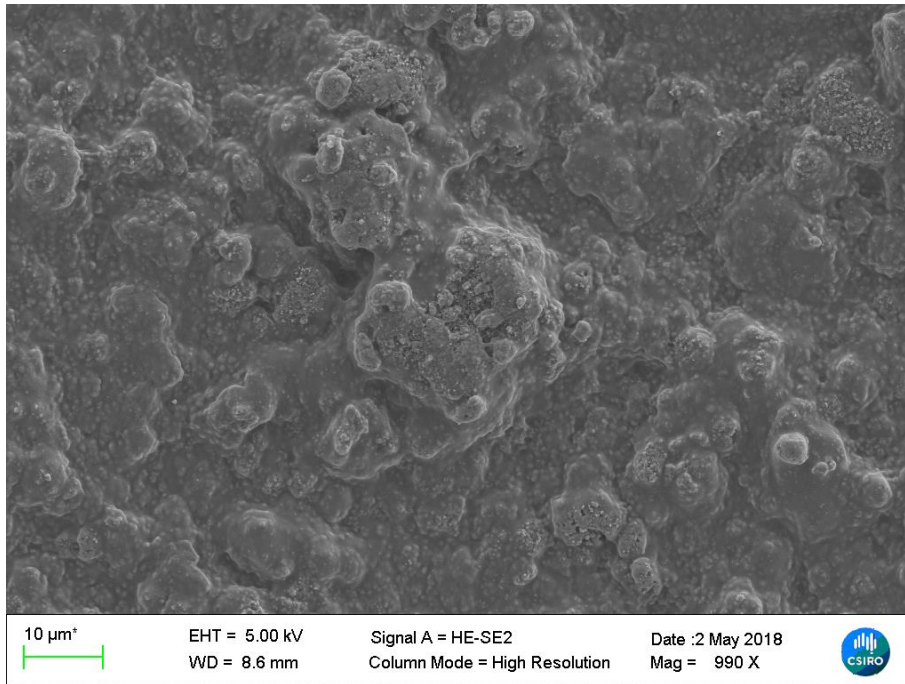
(a) active layer of M1



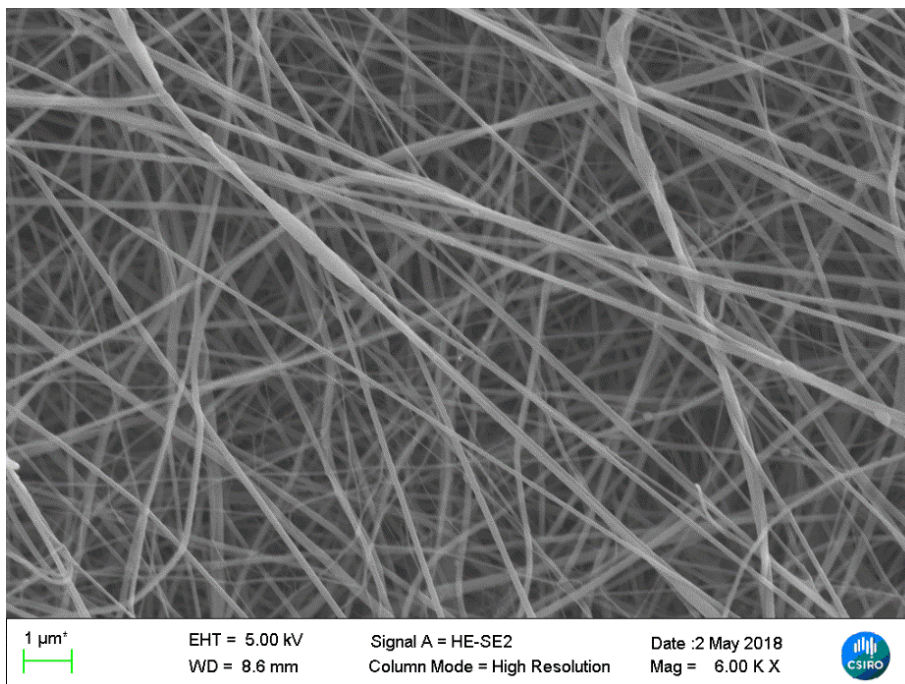
(b) M2 membrane surface



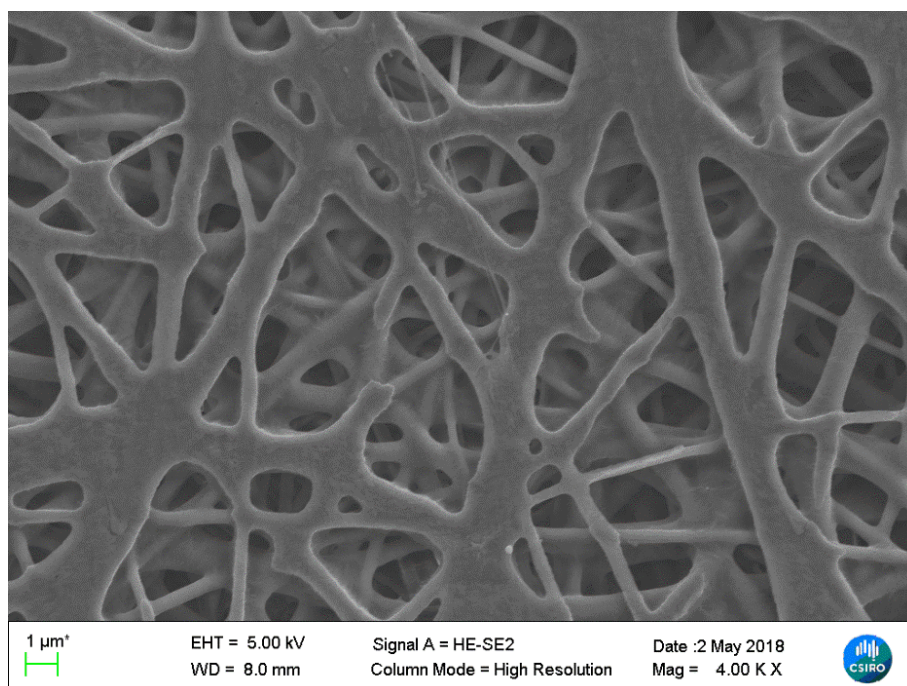
(c) M3 membrane oleophobic coated surface



(d) PU hydrophilic layer of M4 membrane



(e) M5 membrane hydrophilic layer



(f) M5 membrane hydrophobic layer

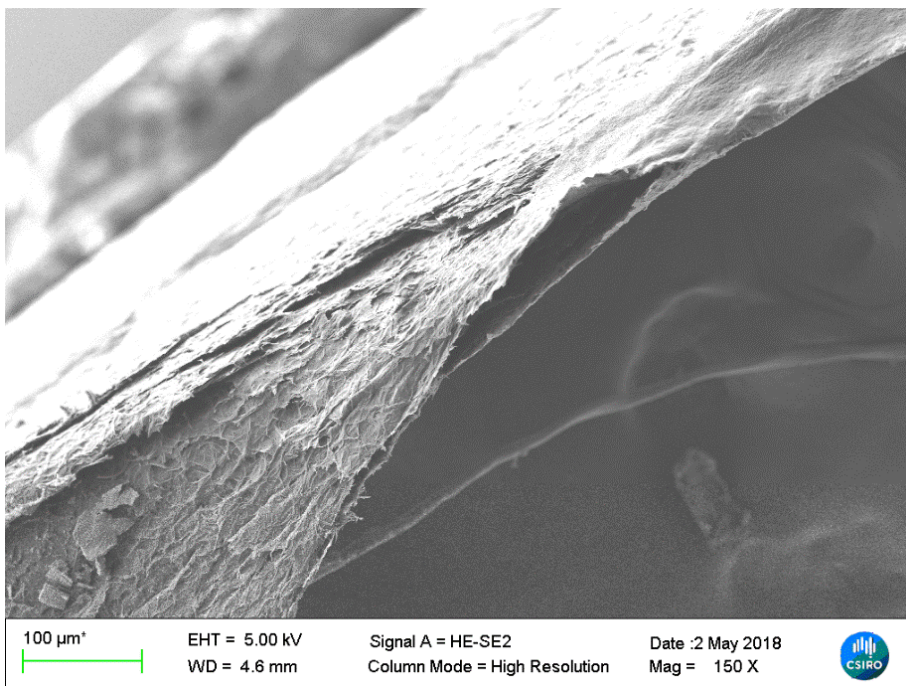
Figure 3.4. SEM images of membrane surfaces

Fig. 3.5 shows SEM images for the membranes' cross sections. As can be seen from Fig. 3.5d and Fig. 3.5e, M4 and M5 are dual layer membranes, whereas the other membranes are single layer. Nevertheless, M1 has active and support layers, that can be seen from Fig. 3.5a. For M5, layers were detached during the SEM testing, so it made much easier to see the layers. From Fig. 3.5e, the thicker layer is the hydrophobic and thinner layer is hydrophilic. For M4, on top of the thin PU layer, hydrophobic PTFE layer can be observed with attachment of textile support layer.

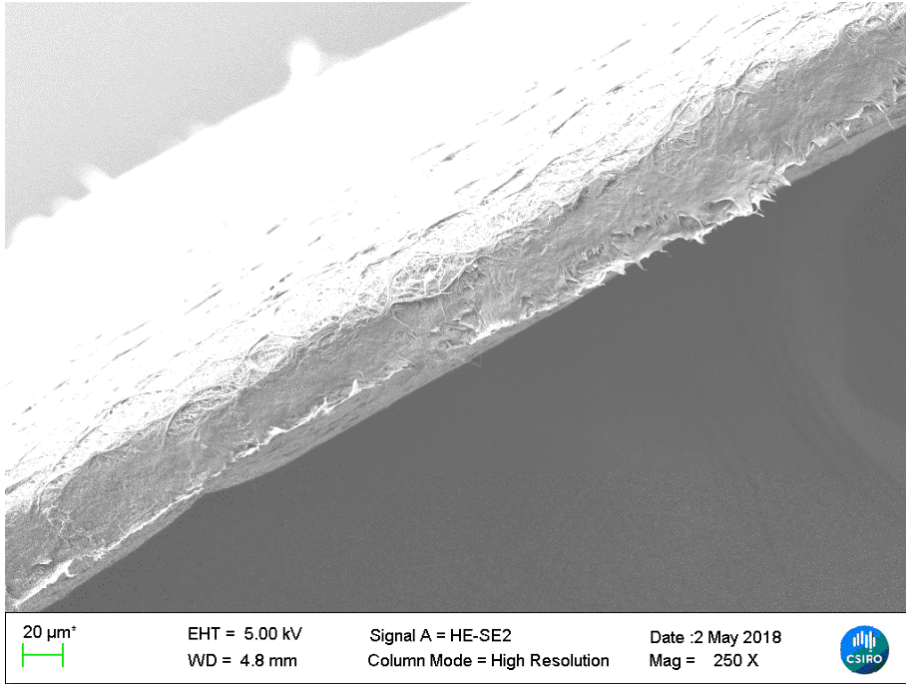
Although M3 is a single layer membrane, it has an oleophobic coating on PE membrane. Fig. 3.5c showed the cross section for M3. From this image, the thickness of the membrane is higher than the thickness of M2. Amongst the membranes, M2 is the one the thinnest. From Fig. 3.5a, M1 has active layer supported by a bone-like structure.



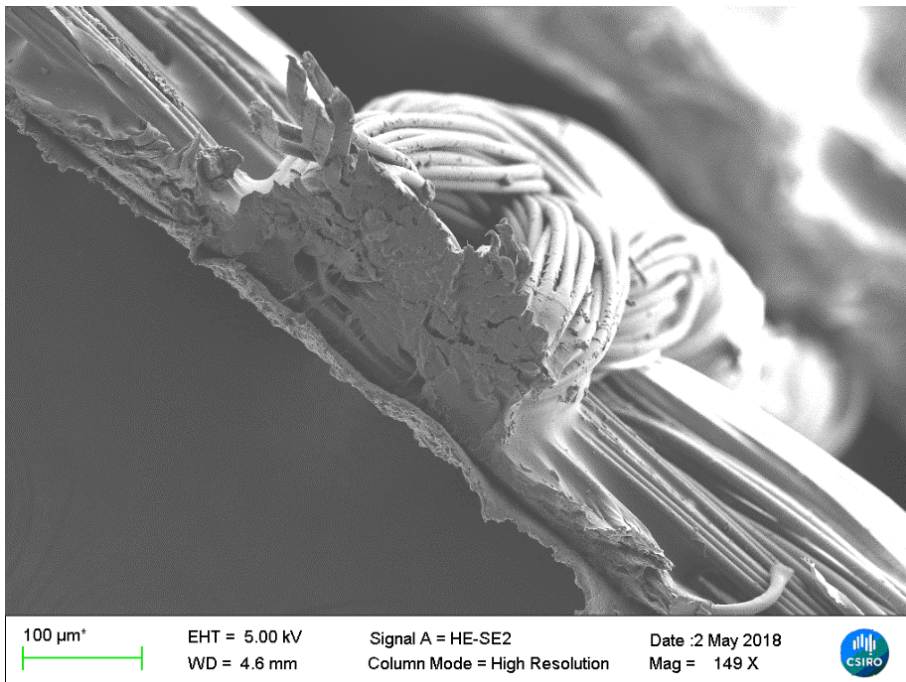
(a)



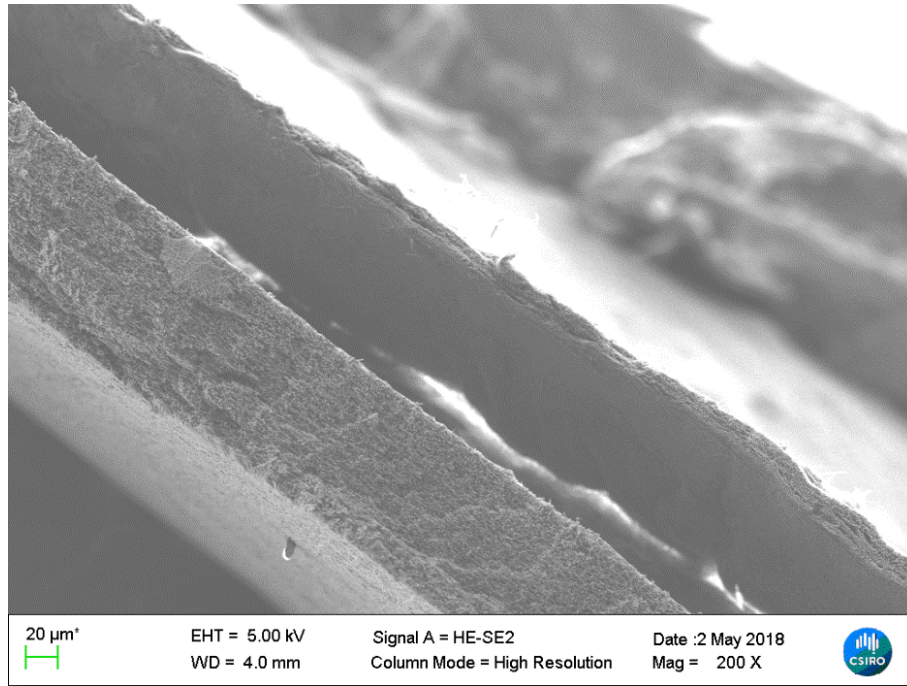
(b)



(c)



(d)

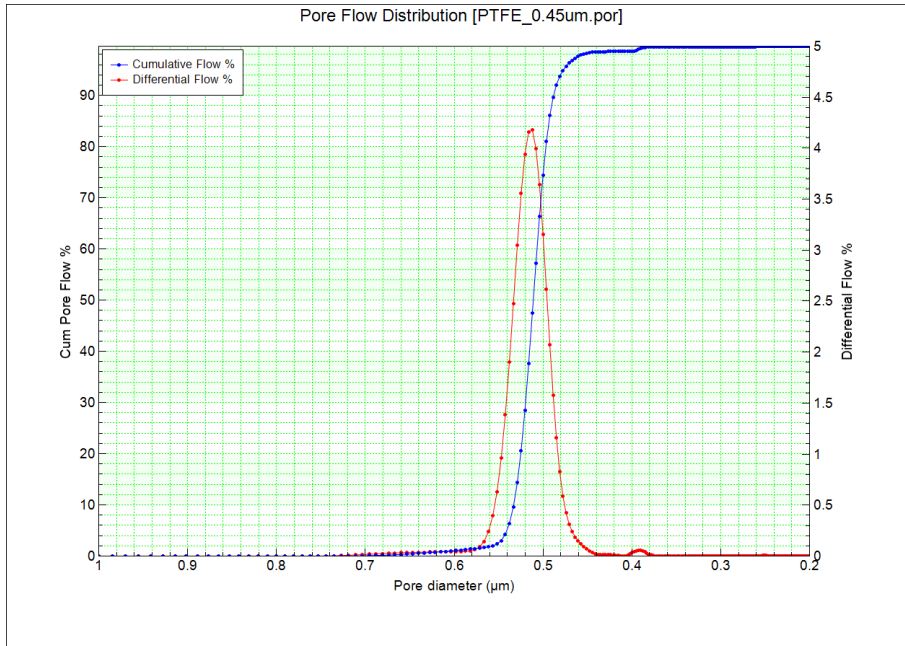


(e)

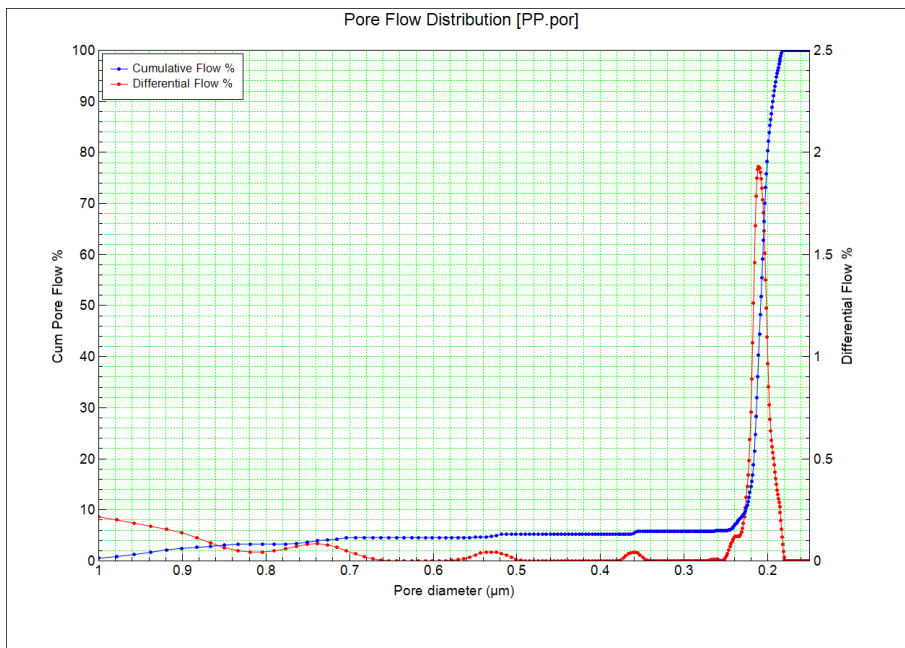
Figure 3.5. Cross sections of membranes (a) M1 (b) M2 (c) M3 (d) M4 (e) M5

Fig. 3.6 illustrates the pore size distribution graphs for M1, M2, M3 and M5. Both hydrophobic and hydrophilic layer pore size distributions were examined for M5. Pore size distribution identifies the range of pore sizes throughout the membrane. Fig. 3.6a showed that M1 has the largest mean pore size. Among all membranes, M3 has the smallest mean pore size as it was illustrated in Fig. 3.6c. From Fig. 3.6d and Fig. 3.6e, M5 hydrophobic top layer mean pore diameter was larger than the hydrophilic layer support layer mean pore diameter. For M5, the mass transfer resistance of a hydrophilic layer is higher than a hydrophobic layer.

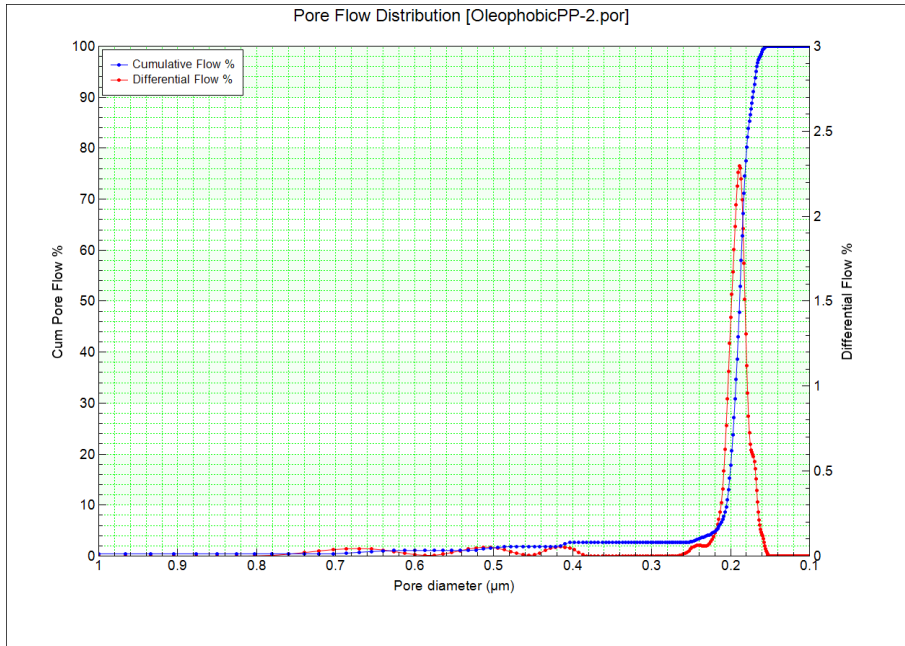
The pore size measurement was not done for M4 membrane because the dense layer made was not compatible with the measurement technique.



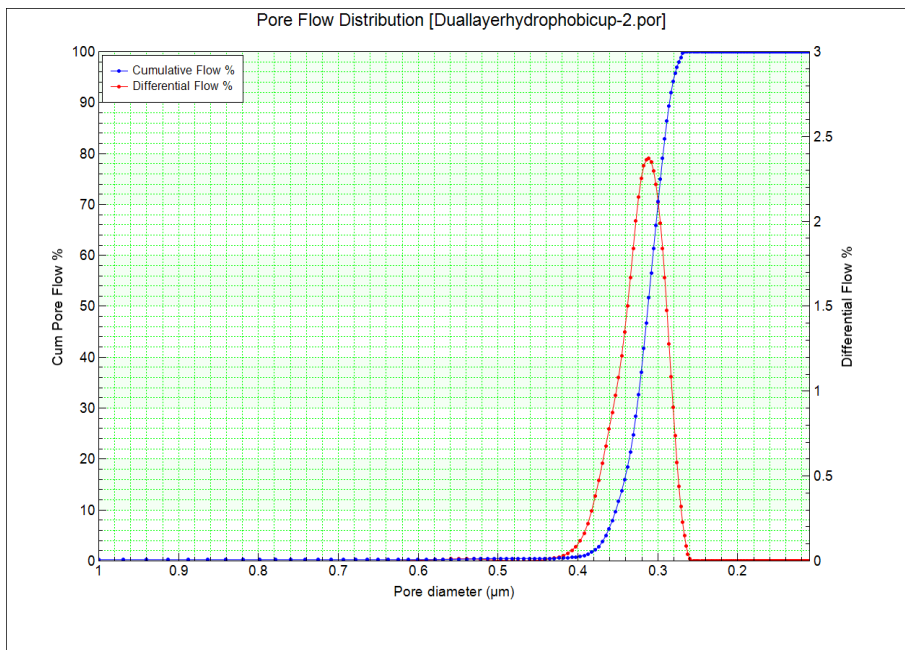
(a)



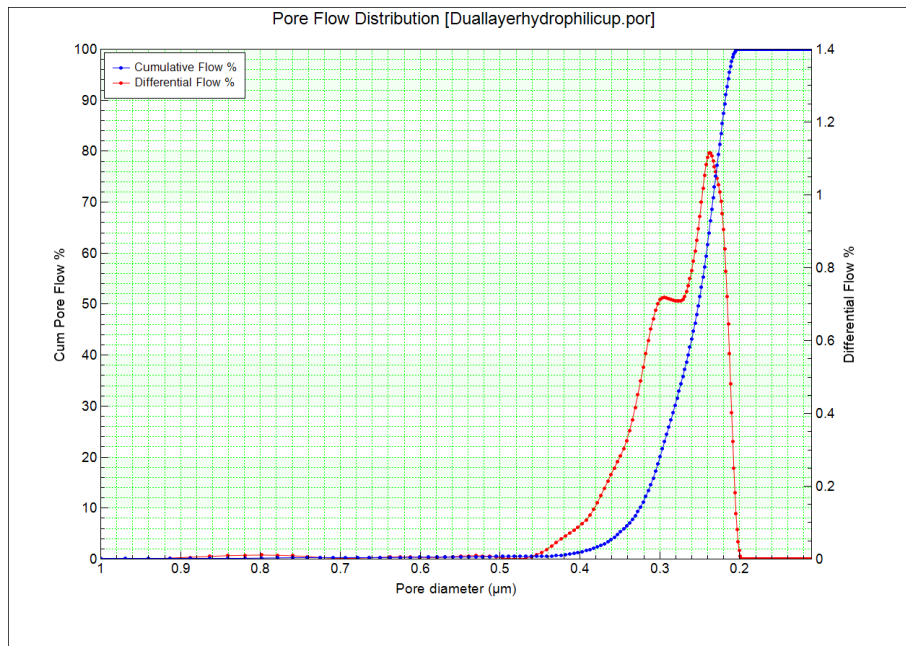
(b)



(c)



(d)



(e)

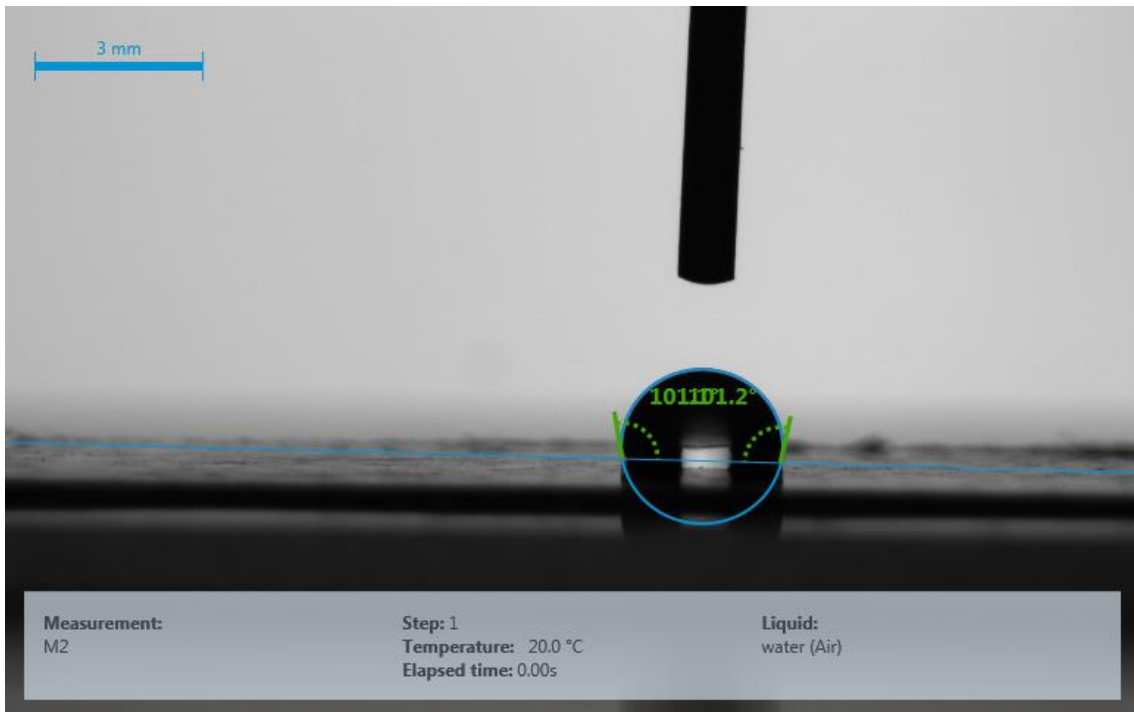
Figure 3.6. Pore flow distributions (a) M1 (b) M2 (c) M3 (d) hydrophobic layer of M5
(e) hydrophilic layer of M5

Fig. 3.7 demonstrates contact angle measurements of the membranes. All images were taken after calibration of the video capture. Membranes can be ordered from most hydrophobic to least hydrophobic as: M1, M5, M3, M2, M4. This order, however, was based on their layers, which was faced on the feed solution. When comparison was made between dual layer membranes, M4 and M5, hydrophobicity and hydrophilicity of M5 was found more than M4.

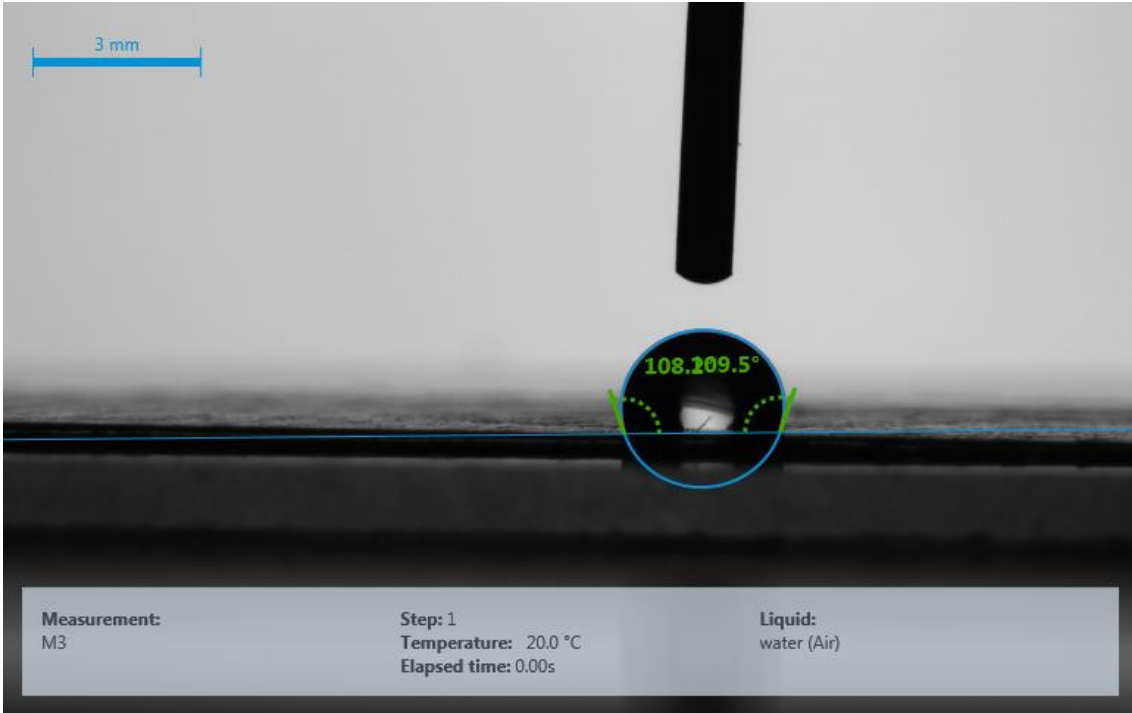
From Fig. 3.7c shows the hydrophobicity for M3, in which is also oleophobic (oil-repellent). Fig. 3.7d and Fig. 3.7f are the images for hydrophilic layers of dual layer membranes. Wetting tendency can be higher for M2 and M4 in order to their hydrophobicity. Although contact angles of the membranes were not used in modelling, it was important to understand their hydrophobicity in order to assume the character when contacting with feed.



(a)



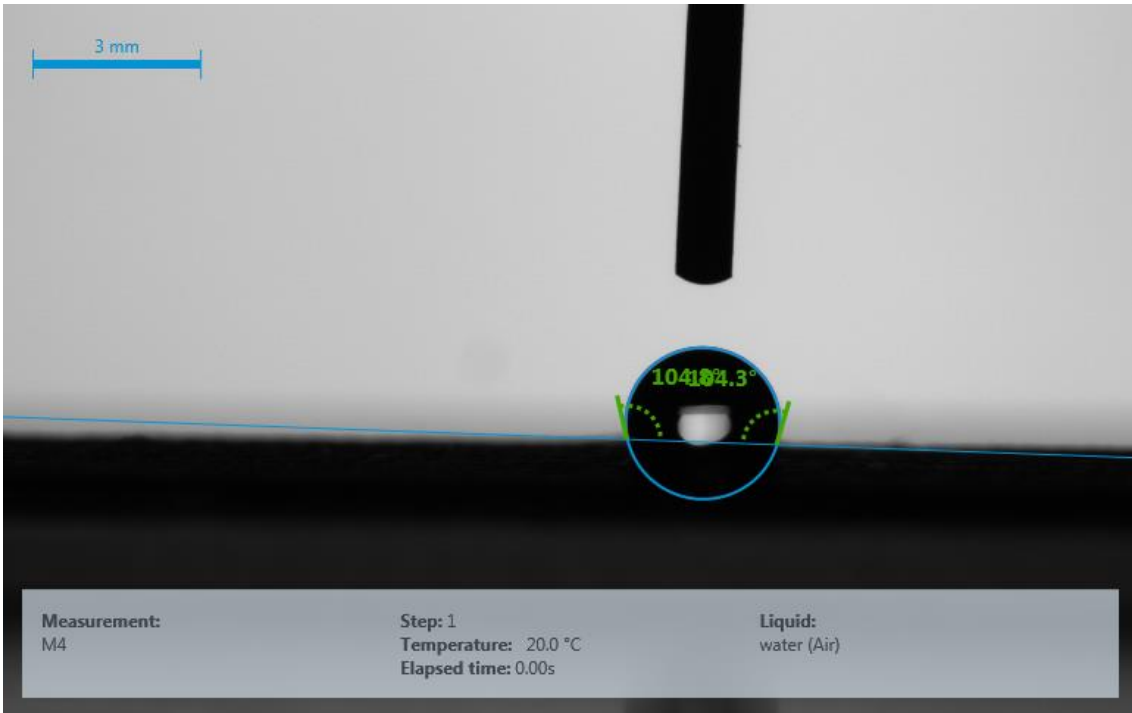
(b)



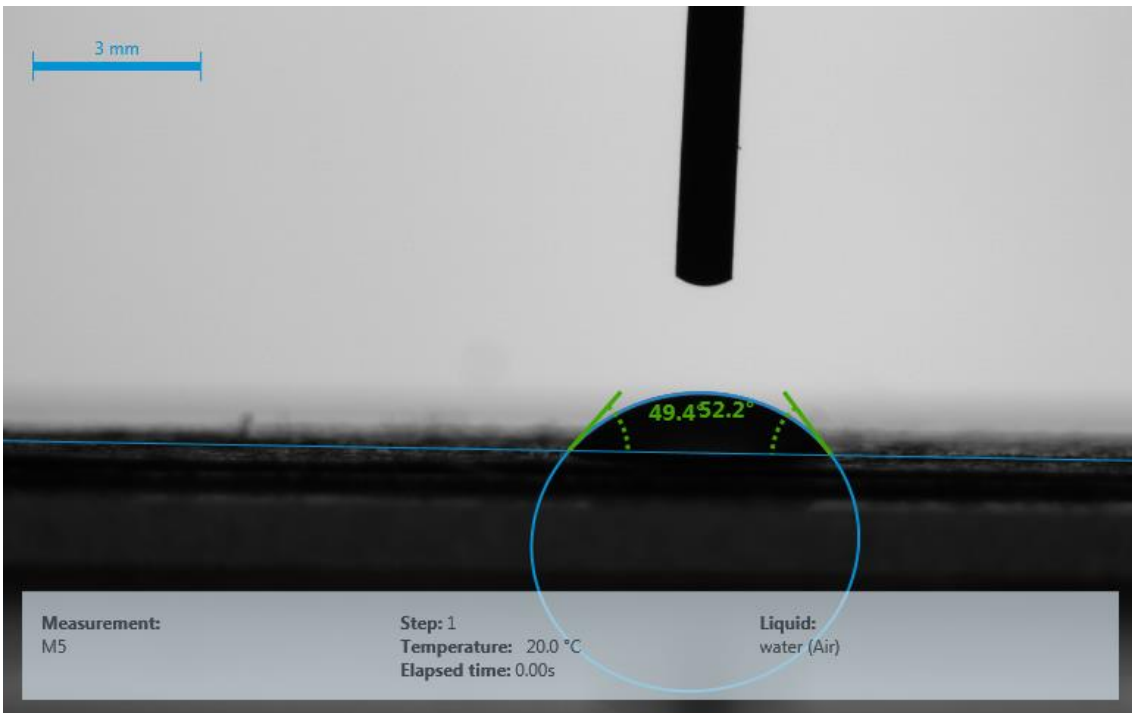
(c)



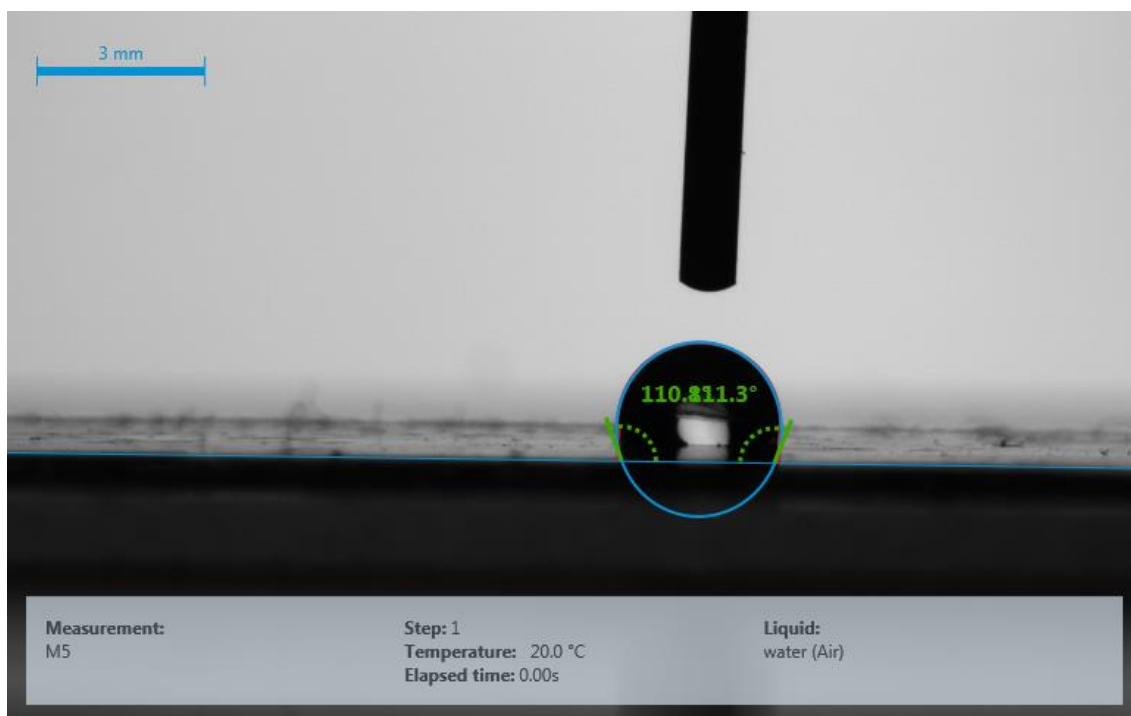
(d)



(e)



(f)



(g)

Figure 3.7. Contact angle measurement images for membranes (a) M1, (b) M2, (c) M3, (d) M4 hydrophilic layer, (e) M4 hydrophobic layer, (f) M5 hydrophilic layer, (g) M5 hydrophobic layer

3.4. Summary

Characterisation tests for the membranes were conducted in order to determine their porosities, pore sizes, and thicknesses so that these characteristics can be used to calculate mass and heat transfer coefficients in the model. FT-IR spectroscopy revealed all membranes' functional groups such as C-C, C-H bonding. SEM was successfully conducted to image both the membranes surfaces and cross sections. Surface images of the membranes showed their porous structures. Cross sections of the membranes were examined to measure the thicknesses. The M5 membrane's hydrophilic layer was thicker than the M4 membrane's hydrophilic layer. Hydrophobic layer of M5 was also thicker than the hydrophobic layer of M4 (when textile support excluded). Porosities of the membranes were calculated via gravimetric analysis with wetting and non-wetting fluids. High porosity was required for high MD flux and PTFE (M1) had the highest porosity among the membranes and the highest flux. Pore sizes of the membranes were determined

by Porometer. Minimum, mean and maximum pore sizes as well as bubble points of the membranes were measured by Porometer. Mean pore size was used to calculate the mass transfer coefficients. Pore flow distribution graphs were also provided by Porometer. M1 membrane has the maximum pore size, whereas M3 membrane has the smallest mean pore size. LEP tests were conducted for some of the membranes. Contact angles of the membranes showed their hydrophobicity, and the most hydrophobic membrane was found as M1, and least hydrophobic layer was M4.

CHAPTER 4. PERFORMANCE OF SINGLE LAYER AND DUAL LAYER MEMBRANES IN MEMBRANE DISTILLATION

4.1. Introduction

High efficiency in MD can be defined as high flux with high thermal efficiency, and the performance will be determined by 3 elements; 1-Membrane characteristics, 2- Process conditions, and 3- Membrane module design [78].

High Performance MD: High flux and energy efficient MD		
Membrane	Process Conditions	Membrane Module
Hydrophobic and wetting property Membrane thickness High porosity Pore size Low tortuosity (close to 1)	High feed temperature Low permeate temperature High flow rate Hydrostatic pressure < LEP System isolation and heat recovery	Provide high rate mass transfer Provide high turbulence for feed and permeate Low pressure drops Efficient evaporation

Figure 4.1. Parameters for better performance MD

Fig. 4.1 shows parameter requirements for high performance Membrane Distillation process [35, 79].

Membrane properties affecting permeate flux to get high performance MD have been discussed in the Chapter 3. In this chapter, process conditions and membrane module factors will be discussed.

4.2. Membrane Distillation Performance Parameters

4.2.1. Process conditions

Different process conditions affect the permeate flux as well as energy efficiency of the process. Better performance for MD can be obtained by high fluxes with moderate energy consumption [78].

Process conditions can be adjusted to minimise the performance deterioration effects. One of the vital parameters is process temperature. The feed inlet temperature highly effects the flux [80].

Temperature can be counted as one of the most important parameters that leads to high performance MD. Feed inlet temperature increases the permeate flux approximately linearly [35, 81]. The reason for this is that the vapor pressure of water increases exponentially with temperature as described by the Antoine Equation [20]. However, permeate temperature increase decreases the permeate flux and has the opposite effect to feed inlet temperature [35]. With the decrease of permeate temperature, permeate flux is expected to increase due to the an increase in vapor pressure difference across the membrane as the vapour pressure decreases on the permeate side [34]. From an economical implementation point of view, feed inlet temperature should be 50°C or higher [35]. In MD, high feed inlet temperature and low permeate temperature are ideal to get high flux.

Another process condition effect on permeate flux is flow rate of the feed and permeate sides. When flow rate of the feed increases, permeate flux also increases [81]. High velocity creates turbulence inside the membrane module that leads to an increase in driving force as the turbulence reduces temperature polarization [30, 82]. However, hydrostatic pressure should not exceed the liquid entry pressure (LEP) while increasing the feed and permeate flow rate. Exceeding the LEP results in wetting of the membrane and compromises rejection rate [35].

Salt concentration in the feed solution also affects the permeate flux. Non-volatile solutes such as salt ions in the feed solution decrease the vapor pressure that is exacerbated by concentration polarization, so that it reduces permeate flux [35]. The existence of concentration polarization reduces the mass transfer coefficient at the boundary layer of the feed side [20]. However, for the effect of salt concentration on vapour pressure is very low except when approaching saturation conditions (e.g. 350,000 mg/L NaCl). For volatile solutes, increasing the concentration of solutes in the feed also increases the vapor

pressure according to Henry's law, and the concentration of volatile solutes (e.g. ammonia) in the permeate increases.

Rejection rate across the membrane is expressed as a percentage, and is the concentration difference between feed and permeate as a percentage of the feed concentration as shown in Eq. 4.1 [83, 84].

$$R = \frac{C_f - C_p}{C_f} \quad (4.1)$$

R is the salt rejection coefficient, C_f is the feed concentration and C_p is the permeate concentration [85].

4.2.2. Membrane module

Membrane module design can also contribute to achieving high flux for membrane distillation process. Different module designs are adopted for Direct Contact Membrane Distillation (DCMD). However, the two commonly used module designs considered are hollow fiber and flat sheet modules. Fig. 4.2 depicts these module designs [21].

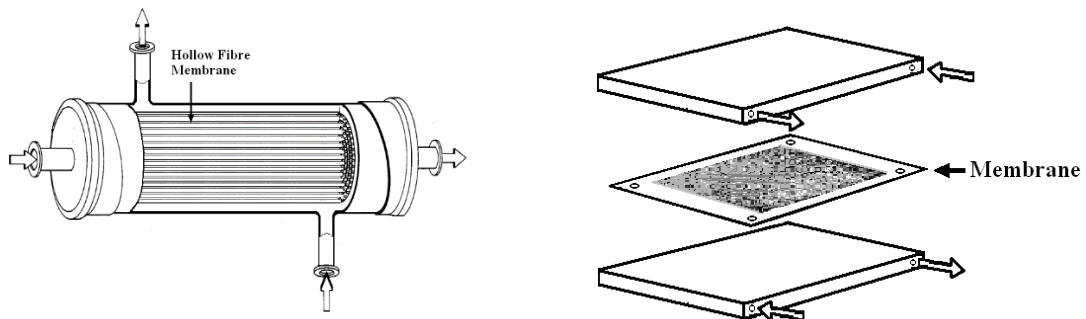


Figure 4.2. Tubular module for hollow fiber and plate module for flat sheet membrane

[21]

For hollow fiber configuration, feed enters the module on either the shell side or lumen side of the module and permeate on the other side of the membrane. This module configuration may have advantages due to its larger area per unit volume for use in commercial applications [30]. The disadvantage with this module can be observed that high temperature polarization is generated when uniform flow distribution cannot be achieved. These problems can be overcome by using a cross flow module.

Another common used module is the plate and frame module, which can be used for flat sheet membranes. In this module, a membrane is placed between the spacers and frames [20]. This module is mostly used in laboratory experiments while testing the membrane for the effect on the flux and energy efficiency. Flat sheet membranes are also used commercially in spiral wound modules where the flow is not uniform as it is for plate and frame modules [11]. The plate and frame arrangement provides controlled hydrodynamic flows that improve membrane performance, and cleaning and replacing the membrane is easier compared to other types of modules [11]. In this study, plate and frame flat sheet module was used to perform direct contact membrane distillation. Fig. 4.3 shows a schematic diagram of the module arrangement [65].

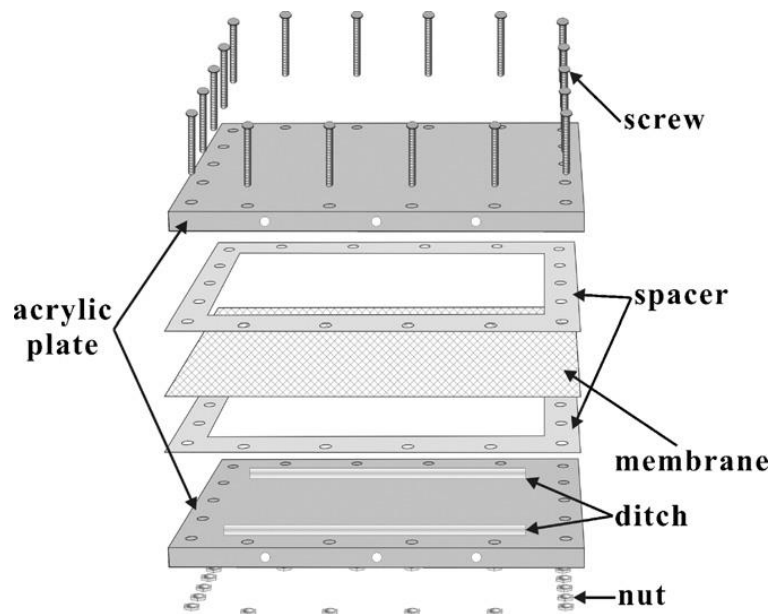


Figure 4.3. Plate and frame DCMD module set-up [65]

The membrane module should meet some requirements to get high efficiency membrane distillation [80]. These requirements are high turbulence for feed and permeate inside the channel to reduce temperature polarisation and increase flux. Another possible solution to diminish the temperature polarization effect is to set-up the module with spacers as in Fig. 4.3. Spacers can cut down the temperature polarization coefficient (TPC) to approximately 30 percent [30]. High rate mass and heat transfer can be achieved by high feed and low permeate temperature. However, it is worth mentioning that temperature polarization effect that reduces the performance arises from heat transfer through the membrane.

Different flow modes through the module that are used are: co-current, counter-current and cross-flow. The most commonly used flow arrangements are co-current and counter-current in MD. Counter-current flow is likely to perform better flux than co-current flow [86]. These flow modes for DCMD configuration are depicted in Fig. 4.4 [86].

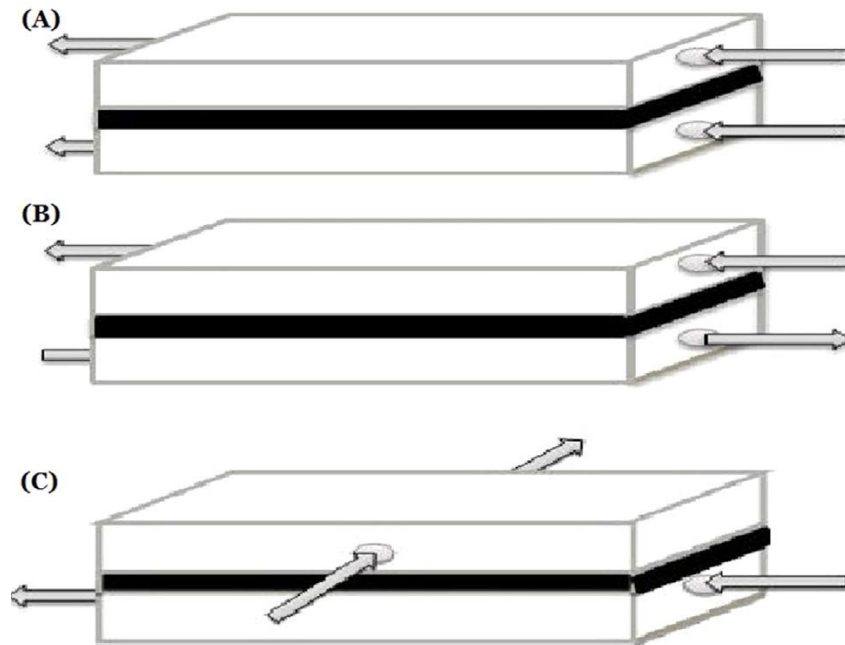


Figure 4.4. Flow modes for DCMD (A) co-current (B) counter-current (C) cross-current flows [86]

Low pressure drop along the membrane is another criteria for a well-designed module, as it prevents flooding in the membrane pores as the hydraulic pressure can be kept below the LEP so that wetting is prevented [11].

4.3. Direct Contact Membrane Distillation Performance

Direct contact membrane distillation performance can be judged by permeate flux (product), rejection and energy efficiency. Permeate flux (J) can be calculated by following Eq. 4.2.

$$J = C_m (P_f - P_p) \quad (4.2)$$

where C_m is the mass transfer coefficient, P_f is the vapor pressure at the feed side, P_p is the vapor pressure at the permeate side [20]. Vapor pressures on the bulk sides can be calculated by using the Antoine equation, which will be discussed in Chapter 5.

Calculating salt rejection factor via Eq. 4.1 is used to identify if the membrane has leaking or wetting issues, which reduce rejection and effects MD performance negatively.

Thermal efficiency for MD is the proportion of vaporisation latent heat to total heat transferred (via latent heat and conductive losses) from the feed to the permeate, as defined in Eq. 4.3 [20]. Thermal efficiency can be enhanced by high feed temperature, high flow rates and adequate membrane thickness [87, 88].

$$\text{Thermal efficiency} = \frac{J\Delta H_v}{J\Delta H_v + Q_{\text{conductive}}} \quad (4.3)$$

Specific flux or a global mass transfer coefficient, C_{global} is calculated to remove the effects of temperature difference (related to partial pressures) from the assessment. The global mass transfer term is related to the membrane properties and hydrodynamic resistance. At high flowrates when the flow is fully developed, the global mass transfer coefficient becomes independent of feed velocity.

$$J = C_{\text{global}} (P_{\text{Tf}} - P_{\text{Tp}}) \quad (4.4)$$

C_{global} can be calculated using Eq. 4.4 and calculating partial pressure difference in the bulk temperatures on feed and permeate sides of the membrane, respectively. J is the instantaneous flux and can be calculated by the following Eq. 4.5.

$$J = \frac{V}{At} \quad (4.5)$$

where V is the volume for weighted and collected permeate, t is the time period, A is the membrane area. The difference of vapor pressures at the feed bulk and permeate bulk is named as $\Delta P_{\text{average}}$, and equations Eq. 4.6 and Eq. 4.7 are used to calculate the average vapour pressure difference depending upon the flow arrangement.

Co-current flow:

$$\Delta P_{\text{average}} = \frac{(P_{fi} - P_{pi}) - (P_{fo} - P_{po})}{\ln \left[\frac{P_{fi} - P_{po}}{P_{fo} - P_{po}} \right]} \quad (4.6)$$

Counter-current flow:

$$\Delta P_{\text{average}} = \frac{(P_{fi} - P_{po}) - (P_{fo} - P_{pi})}{\ln \left[\frac{P_{fi} - P_{po}}{P_{fo} - P_{pi}} \right]} \quad (4.7)$$

$$C_{\text{global}} = \frac{J}{\Delta P_{\text{average}}} \quad (4.8)$$

MD flux is also affected by the dimension of the membrane, and flux can be increased using short and wide membranes compared to long and narrow membranes [67].

4.4. Experimental and Methods

Direct contact membrane distillation experiments were conducted for 4 hours and the system set-up is as shown in Fig. 4.5. DCMD set-up contained conductivity meter, balance, membrane module, feed and permeate pumps, heater and chiller. The feed solution was held in the feed reservoir tank and permeate was collected in the product reservoir tank, which was weighed throughout the experiment by a balance.

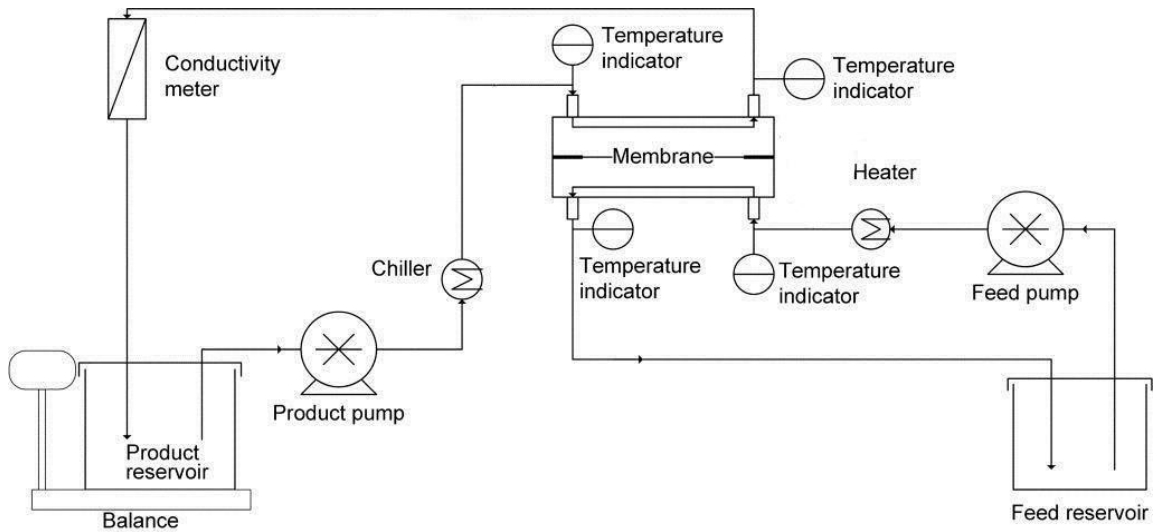


Figure 4.5. Membrane Distillation process set-up [1]

DCMD experiments were conducted for the five types of the membrane which are shown in Table 3.1. Experiments were done at different conditions such as feed and permeate temperatures and flow rates, and the conditions can be found in Table 4.1. Dual layer hydrophobic/hydrophilic M5 membrane was also tested for one more feed inlet temperature at 80 °C and at a flow rate of 750 ml/min. All experiments were conducted for 1% w/w (10 g/L) salt concentration, and change in the conductivity of the permeate tank was constantly recorded through experiments every 15 minutes by a conductivity

meter. Salt rejection, R, was calculated from Eq. 4.1 as a percentage. For all membranes used in DCMD experiments flux and energy efficiency of the membranes were calculated. Each experiment lasted for 4 hours and was tested in co-current and counter-current flow arrangements. Temperatures at the inlet and outlet of the feed and permeate sides were recorded every 5-15 minutes on data logging software.

Table 4.1. Different experimental conditions for DCMD experiments

Membranes	Flow Type	Flow Rates (ml/min)	Velocity (m/s)	Feed Inlet Temperatures (°C)	Permeate Inlet Temperature (°C)
M1 M4	Co-current	450 530 600	0.079 0.093 0.105	50 60 70	10 20 30
M2 M3	Co-current	530 600	0.093 0.105	60 70	20
M1 M2 M3 M4	Counter-current	530 600	0.093 0.105	60 70	20
M5	Co-current	450 530 600 750	0.079 0.093 0.105 0.131	50 60 70 80	10 20 30
M5	Counter-current	450 530 600 750	0.079 0.093 0.105 0.131	50 60 70 80	20

Experiments for all membranes were performed by adjusting the process conditions as showed in Table 4.1. All experiment conditions were kept constant throughout an experiment. Flow rate, feed and permeate inlet temperatures effects on permeate flux were examined for M1, M2, M3, M4 and M5 membranes, respectively. The channel dimensions and membrane areas can be found in Table 4.2. As the width of the M5 membrane differed to the other membranes, a different module arrangement was used, and the channel dimensions for M5 membrane arrangement are found in Table 4.2.

Table 4.2. Module flow channel dimensions and membrane areas

Membrane Codes	Module Length (mm)	Module width (mm)	Module depth (mm)	Membrane Dimensions (L×W) (mm)
M1, M2, M3, M4	135	135	0.8	135×135
M5	135	135	0.8	135×95

Repeat experiments were undertaken to obtain the reproducibility of the experiments and to estimate the experimental error. The repeat experiments were within 10% of each other.

4.5. Results and Discussion

4.5.1. Direct Contact Membrane Distillation (DCMD) tests for single and dual layer membranes

DCMD tests for membranes were conducted for PTFE (M1), PE (M2), O-PE (M3), PU-PTFE (M4), and PVDF-co-HFP-N6 (M5). Both co-current and counter-current flow modes were performed for all membranes. As was mentioned in Table 4.1, DCMD tests for M5 membrane were operated at 600 ml/min (0.105 m/s) while changing the temperature. For the other membranes, 530 ml/min (0.093 m/s) flowrate was used while changing the temperatures.

4.5.1.1. Global mass transfer coefficient (C_{global}) dependence on velocity

Comparison between MD membranes' performance can be evaluated by calculating the global mass transfer coefficient (C_{global}). Increasing the velocity in DCMD experiments increases the turbulence and the temperature difference across the membrane. Calculating C_{global} removes the effect of temperature and flowrate, if the flow is fully developed, while maintaining differences due to membrane characteristics [1]. Then comparison of mass transfer coefficients between membranes can be made [1].

Fig. 4.6 shows C_{global} dependence on velocity for co-current flow. As velocity increased, global mass transfer coefficient also increased for all membranes. M3 and M4 showed identical trend at 0.093 and 0.105 m/s.

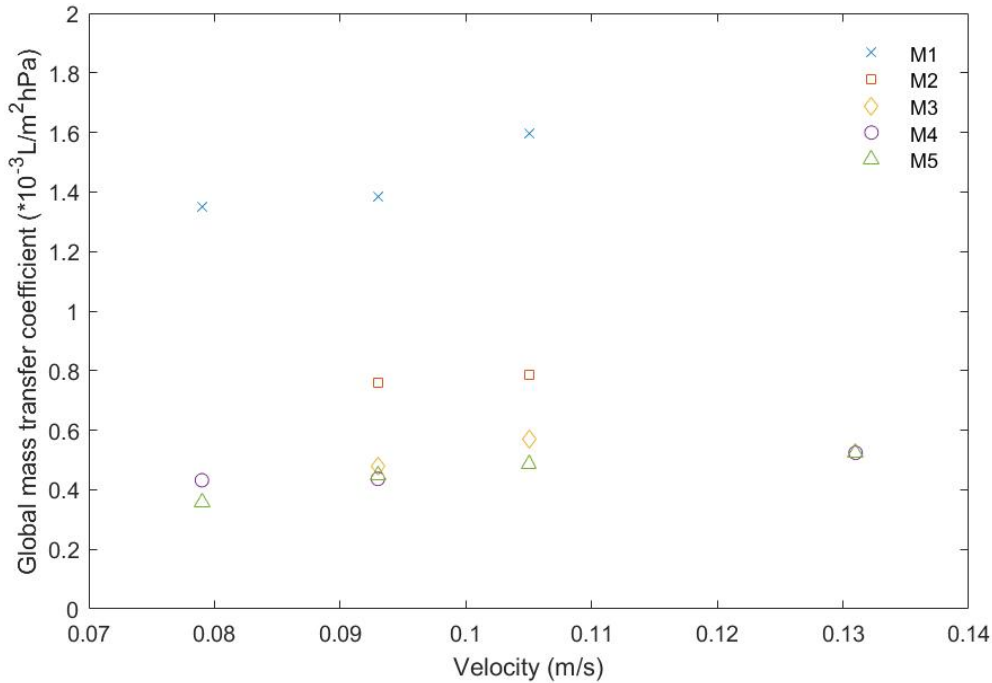


Figure 4.6. Global mass transfer coefficient relation to velocity for co-current flow at 60°C feed and 20°C permeate inlet temperatures

Performances of the membranes was made by observing their C_{global} values. M1 membrane performance was better than the other membranes for co-current flow, which was followed by M2 and M3, respectively. Performances of dual layer membranes, M4 and M5 were similar to each other. The reason was assumed due to their similar porosity and pore size characteristics. Global mass transfer coefficient was also used as parameter when choosing the right flow rate for M5 membrane, and the ideal flowrate was decided as 600 ml/min (0.105 m/s) for the experiments, that were operated with different feed inlet temperatures while keeping the flowrate constant.

Global mass transfer coefficient versus feed velocity was examined for counter-current flow as it was showed in Fig. 4.7. Increasing the feed velocity from 0.093 m/s to 0.105 m/s boosted C_{global} for all membrane with counter-current flow. However, C_{global} decreased when the velocity increased from 0.105 m/s to 0.131 m/s for M5, although the change was minor and could be assigned to experimental error.

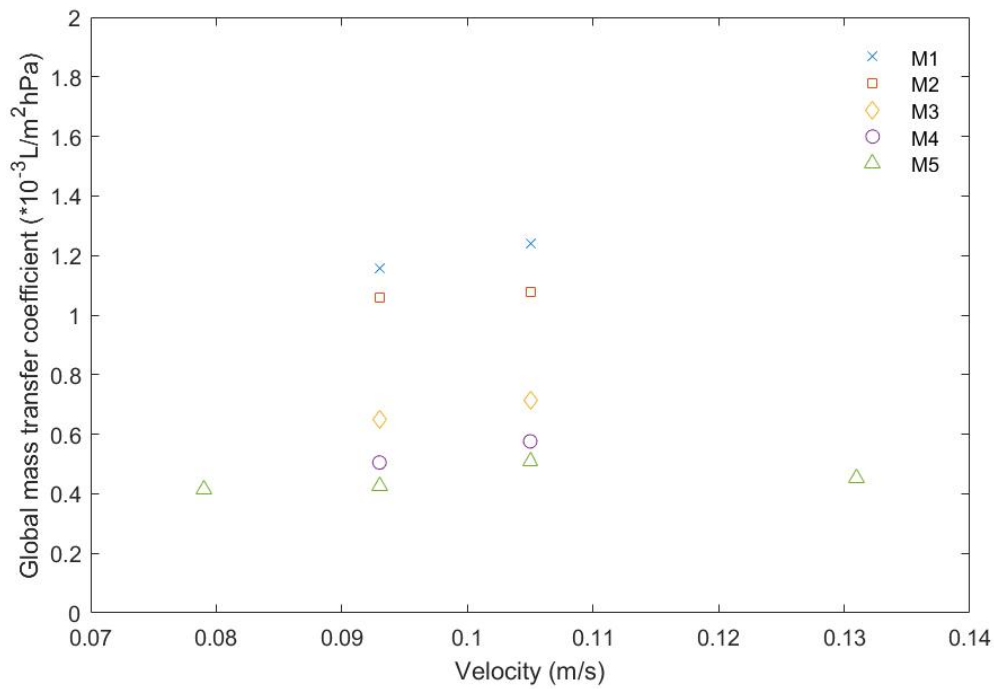


Figure 4.7. Global mass transfer coefficient relation to velocity for counter-current flow at 60°C feed and 20°C permeate inlet temperatures

C_{global} relation with the feed inlet temperature for the membranes was different when compared to co-current flow due to different calculation for average vapour pressure difference for C_{global} .

C_{global} calculation was used to compare the membranes regarding their characteristics by eliminating the effect of temperature and velocity. Therefore, global mass transfer coefficients can be used to compare the performance of the membranes. Global mass transfer coefficients were found to be different for co- and counter-current modes because of the different equations during the calculations of $\Delta P_{\text{average}}$ as it can be seen from Eq. 4.6 and Eq. 4.7. Moreover, different experimental fluxes for the membranes are also the reason for different C_{global} values for co- and counter-current flow modes from Eq. 4.8.

4.5.1.2. Global mass transfer coefficient (C_{global}) relation with temperature

Feed inlet temperature effect on C_{global} was observed for all membranes. Fig. 4.8 revealed the relation between C_{global} and feed inlet temperatures with co-current flow.

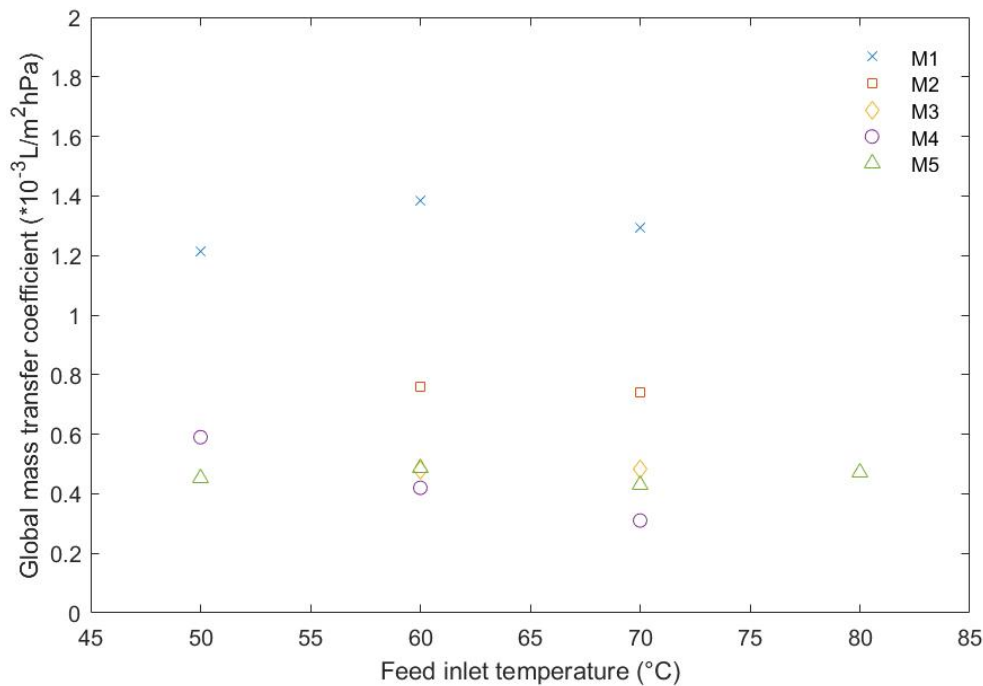


Figure 4.8. Global mass transfer coefficient relation to feed inlet temperature for co-current

Global mass transfer coefficient decreased when the feed inlet temperature increased from 60°C to 70°C for all membranes, and the trend for all membranes was the same for co-current flow. This can be explained by the higher available heat for transfer due to temperature increase at the membrane surface on the feed side that supports higher MD permeate flux [1]. Moreover, more heat transferred to sustain higher flux at higher temperatures results in increased temperature polarization. Hence, the decrease in global mass transfer coefficient can be explained by increased temperature polarization effects at higher temperatures that act to reduce the feed side temperature at the membrane surface.

High porosity and larger pore size as well as thinner active layer introduced higher C_{global} for M1 compared to the other membranes. The decrease for M4 can be explained by high temperature decrease across the hydrophilic layer, which resulted in reduced temperature difference across hydrophobic layer where evaporation takes place. The temperature difference across hydrophobic layer was lower than the bulk temperatures from which C_{global} was calculated, so a lower C_{global} was calculated. As the high temperature value across the hydrophobic layer was significantly lower than T_{bf} , the vapour pressure was

much reduced given the exponential relationship between vapour pressure and temperature. This reduction of calculated C_{global} becomes more significant as temperature increases, because of the exponential relationship between vapour pressure and temperature. Nevertheless, this behaviour was not observed for M5 due to the hydrophobic layer being located next to the hot feed, and the increase in vapour pressure on the permeate side being lower in absolute terms, again due to the exponential relationship between temperature and vapour pressure. The temperature decrease across the hydrophobic layer was higher than M4.

Fig. 4.9 shows the relation between vapour pressure and temperature. Vapour pressure increases exponentially as the temperature increases. The triangle values specify the values at the interfaces for membranes M1 and M5. However, T_{sp} interface temperature should be ignored when examining the graph for M1 as it is a single layer membrane. Temperature drop across the hydrophobic layer of M4 was between the temperatures of T_{mp} and T_{sp} , whereas the temperature drop across hydrophobic layer of M5 was between the temperatures, T_{mf} and T_{mp} single layer membranes and M5. Bulk temperatures difference was the difference between T_{bf} and T_{bp} for the membranes.

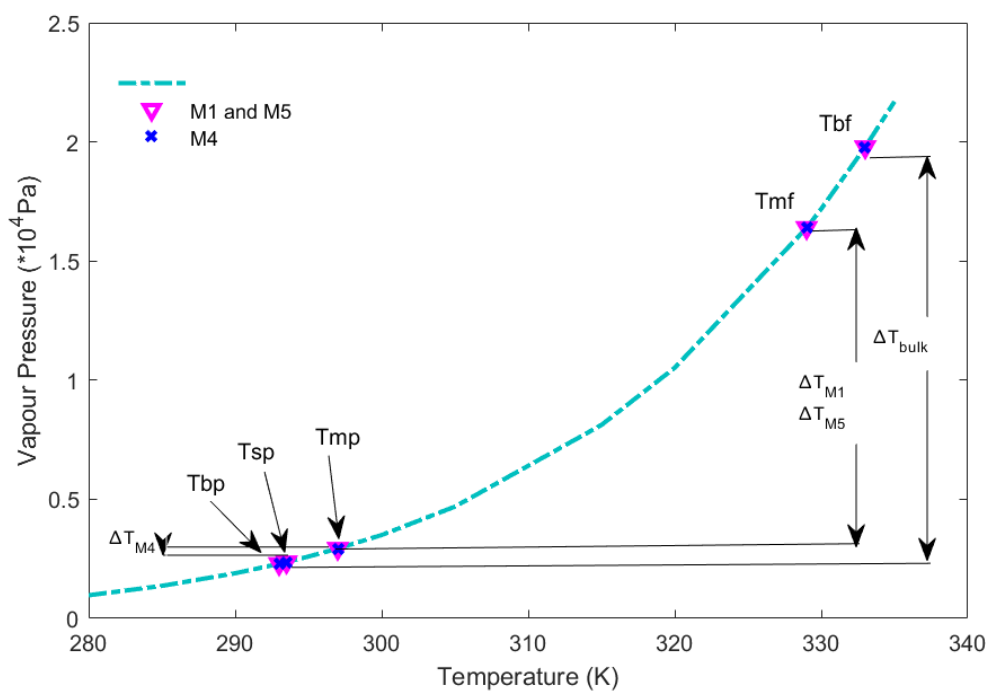


Figure 4.9. Vapour pressure relation to temperature

Fig. 4.10 shows the change of C_{global} with feed inlet temperature for counter-current flow. Global mass transfer coefficient was greater for M1 membrane, and increased with temperature increments. M4 membrane has the lowest C_{global} for counter-current flow at 70°C.

Global mass transfer coefficients increased as the temperature increased from 60°C to 70°C for M1, M2 and M5 on the contrary to co-current flow. However, the global mass transfer coefficient decreased with both flow modes for only M4 membrane due to the low temperature drop across the hydrophobic layer of the membrane.

Global mass transfer coefficients for M2 and M3 were different to each other although their mean pore sizes were similar. M2 had higher porosity and less thickness than M3, which leads to a greater C_{global} compared to M3 for co- and counter-current flow. Oleophobic coating for M3 did not make remarkable change for performance when compared to M2.

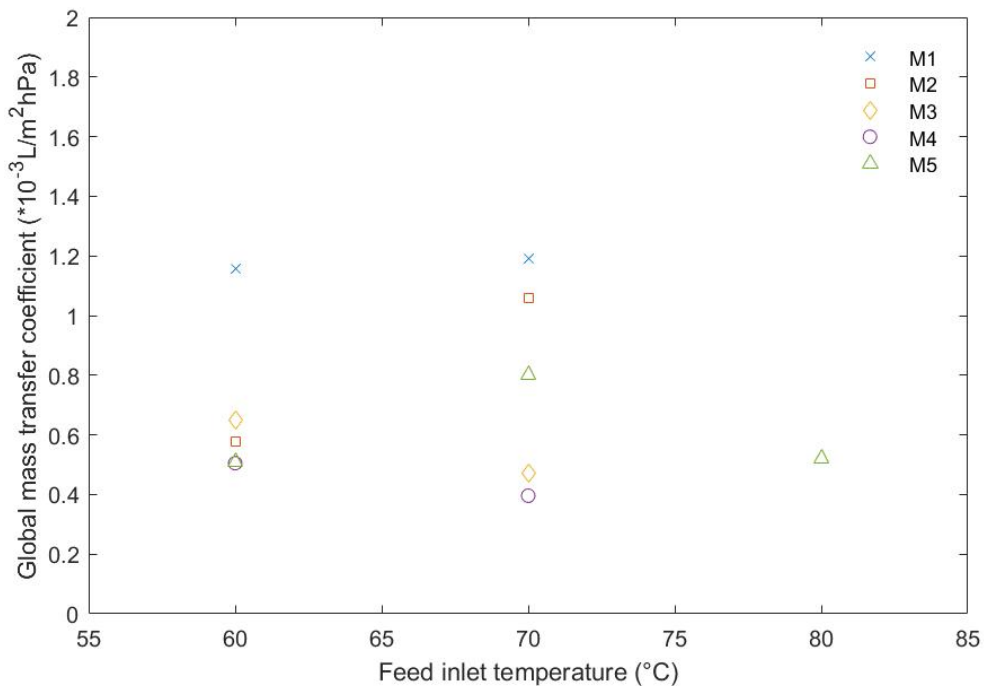


Figure 4.10. Global mass transfer coefficient versus feed inlet temperature for counter-current

4.5.1.3. Salt rejection and velocity relation for single and dual layer membranes

Salt rejection for single and dual layer membranes were calculated at the same feed and permeate inlet temperatures while testing at different velocities. Co-current and counter-current flows were also observed by plotting salt rejection and velocity for the membranes.

Fig. 4.11 shows salt rejection relation with velocities at 60°C feed and 20°C permeate inlet temperature for co-current flow. Rejection of 99.5 and over was achieved for M1, M2, M3 and M4. Rejection of approximately 99% was achieved with M5 membrane at 0.093 m/s. As the feed velocity increased, fluctuation was observed for the rejection of membrane M5. There are a couple of reasons that could explain this behaviour. Those possibilities are membrane wetting, differences in maximum pore sizes, and compressed membrane arising from its repeated use for many experiments. The LEP can be indicator for rejection. Higher salt rejection rate can indicate lower wetting capability for membranes, which can increase the membrane life. Higher salt rejection also produced pure permeate throughout the DCMD tests.

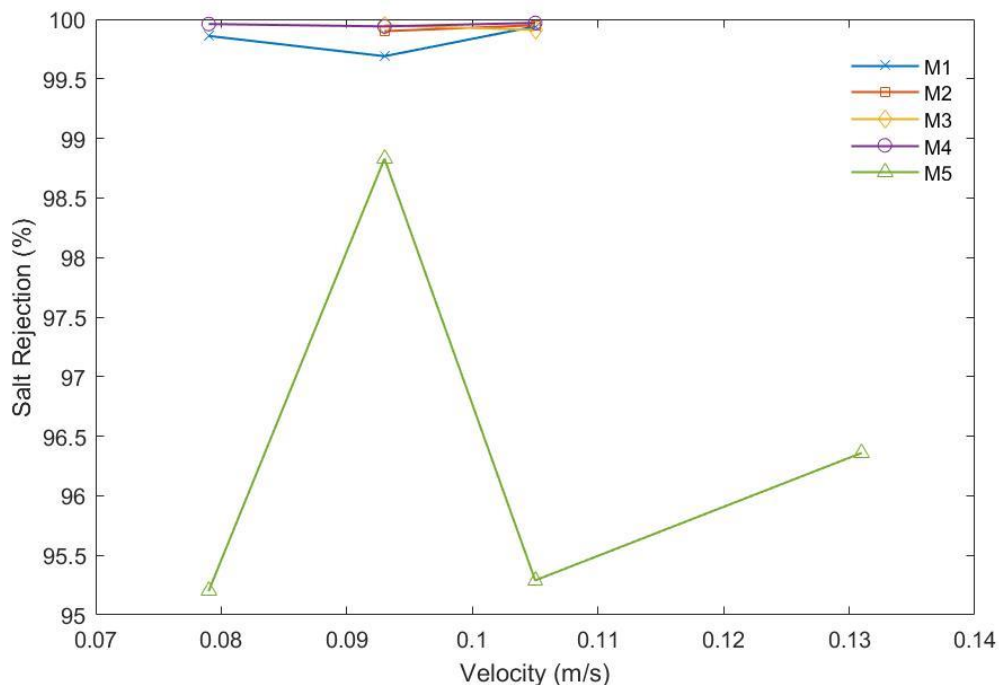


Figure 4.11. Salt rejection at different velocities for co-current flow at 60°C feed and 20°C permeate inlet temperatures

Fig. 4.12 illustrates rejection rate with different velocities for counter-current flow.

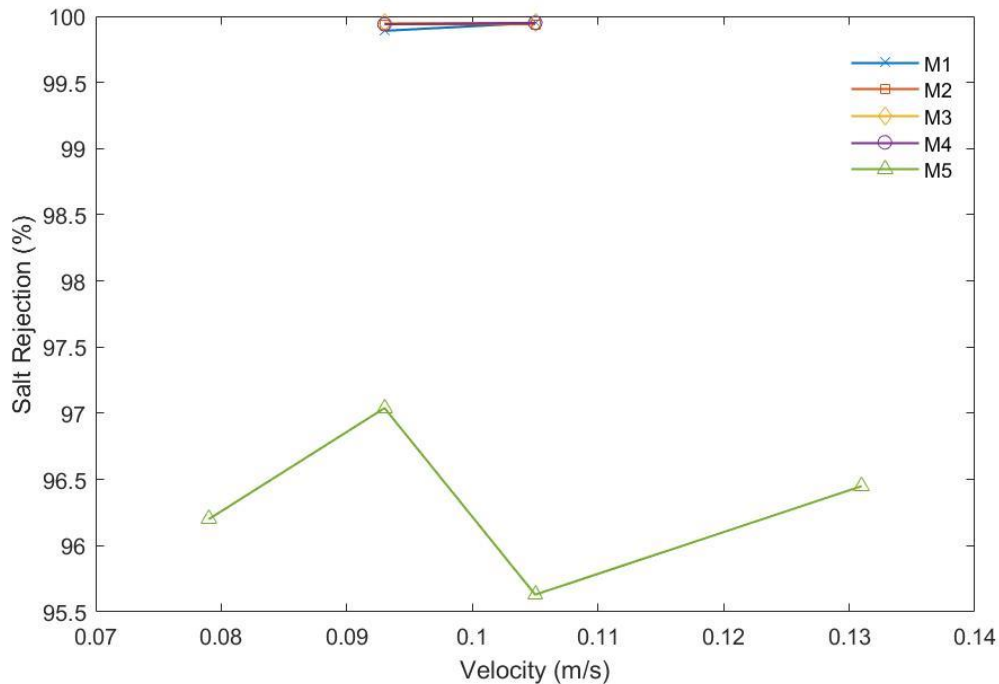


Figure 4.12. Salt rejection at different velocities for counter-current flow at 60°C feed and 20°C permeate inlet temperatures

While observing M5, it can be said that the behaviour was the same when it comes to counter-current flow for salt rejection. Although consistency was achieved between the repeat experiments, rejection rate for M5 membrane fluctuated for counter-current flow.

Rejection for the other membranes were higher with counter-current flow compared to co-current flow. For both flow modes, M5 reached its highest rejection rate at 0.093 m/s. The rejection rate for M5 was better for counter-current flow.

4.5.1.4. Feed inlet temperature effect on salt rejection

Feed inlet temperature effect on salt rejection was observed for single and dual layer membranes during the experiments.

Fig. 4.13 shows salt rejection change with feed inlet temperatures for co-current flow. M5 showed lower rejection when compared with the other membranes. Highest salt rejection for M5 was reached at 80°C. Rejection for M4 was lowest at 50°C.

An increase was observed for M5 membrane as the temperature increased due to lower hydraulic pressure at higher temperatures because of reduced viscosity. This also leads to less wetting through larger pores.

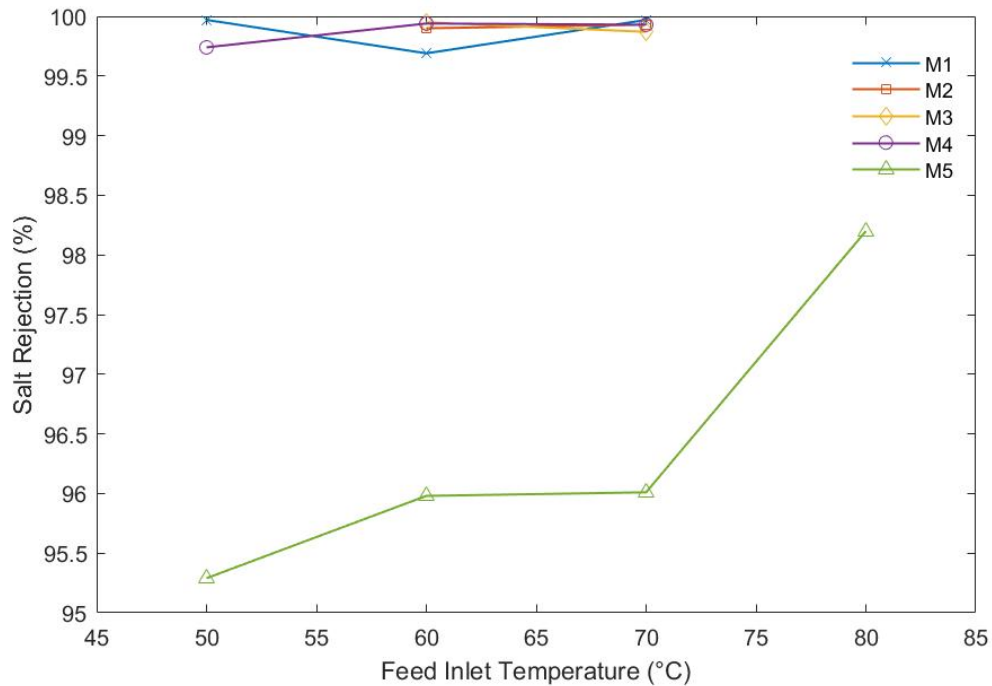


Figure 4.13. Salt rejection at different feed inlet temperatures for co-current flow

Fig. 4.14. demonstrates salt rejection change with different hot inlet temperatures for counter-current flow mode. M1, M2, M3 and M4 achieved better rejection with counter-current flow compared to co-current flow.

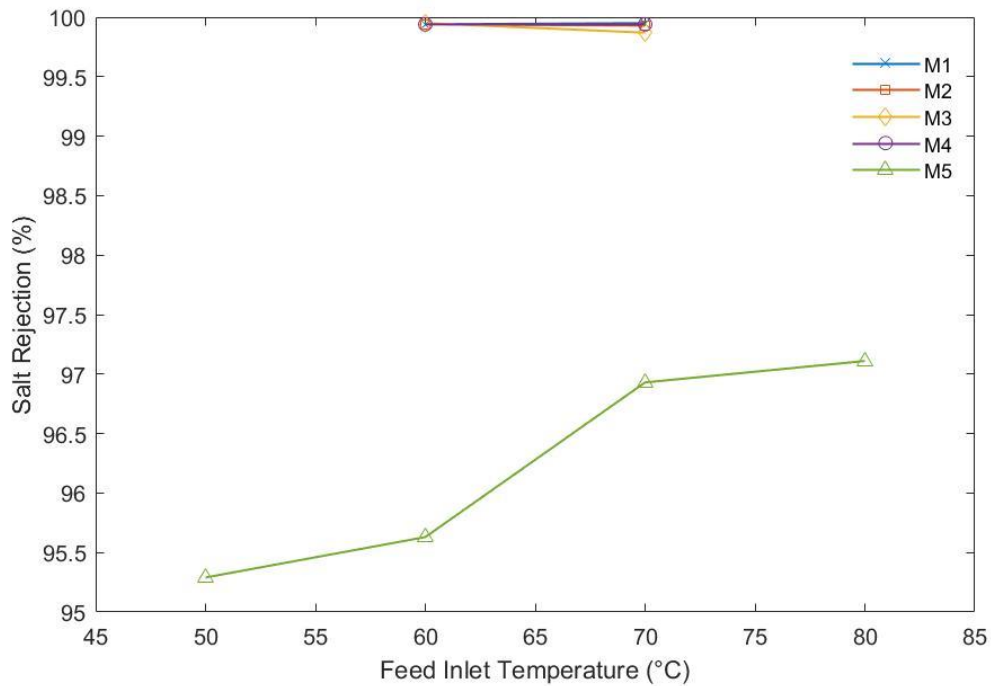


Figure 4.14. Salt rejection at different feed inlet temperatures for counter-current flow

However, rejection at 80°C for counter-current was lower than the rejection at the same temperature for co-current flow.

An increment for M5 was also observed for counter-current flow while increasing the feed inlet temperature. Overall rejection for M5 was lower than the other membranes possibly because of differences in maximum pore sizes. Liquid entry pressures (LEP) for M1 and M5 could possibly provide evidence to support this proposition, however, LEP measurement of M5 was not obtained because the layers could not be separated when undertaking the LEP measurements.

4.6. Summary

Direct contact membrane distillation (DCMD) experiments were conducted with five membranes at different process conditions such as different feed velocities, feed and permeate inlet temperatures for a feed solution with 1% w/w salt concentration.

In this chapter, salt rejection rate and global mass transfer coefficients (C_{global}) for the membranes were calculated. The reason for calculating the global mass transfer was to make the comparison between membranes considering their characteristics by removing the effects of temperature and flowrate. When increasing the velocity for membranes,

global mass transfer coefficients of membranes increased for both co- and counter-current flows due to increased turbulence in the channel. However, C_{global} for M5 at the velocity of 0.131 m/s was lower than at the velocity of 0.105 m/s. Therefore, moderate flowrate was chosen as 600 ml/min (0.105 m/s) for the experiments at the different operating temperatures for M5.

Temperature increment from 60°C to 70°C decreased the global mass transfer coefficients for the membranes, but M3 did not show remarkable change. Although pore sizes were similar for M2 and M3, global mass transfer coefficients were different. This can be related to their different porosities and thicknesses. C_{global} was greater for thinner M2 membrane compared to M3 with co-current flow. The opposite trend was observed for M1, M2 and M5 for counter-current compared to co-current while increasing the temperature from 60°C to 70°C. M1 had the greater C_{global} value due to its larger pore size and higher porosity when compared to the other membranes. C_{global} decreased as the temperature increased for M4 with co- and counter-current flow. The reason was that temperature difference across the feed and hydrophilic layer was higher since the hydrophilic layer was the top layer. This leads to lower temperature drop across the hydrophobic layer and the permeate, in which evaporation occurs. However, this effect was reduced for M5 since the top layer was hydrophobic.

Salt rejection with the change of feed velocity and temperature was examined for the membranes. Increasing the feed inlet temperature also increased the rejection rate for membranes with co- and counter-current flow due to higher temperature difference across the membrane that increased evaporation rate. Overall, M1, M2, M3 and M4 recorded greater rejection rate than M5 membrane. Difference in largest pore size, membrane wetting, or compression for membrane could be the reason for lower rejection rate for M5.

CHAPTER 5. MATHEMATICAL MODELLING OF MEMBRANE DISTILLATION AND COMPARISON WITH EXPERIMENTAL RESULTS

5.1. Introduction

Mathematical modelling for MD requires well developed understanding of the heat and mass transfer phenomena during the membrane distillation process throughout the membrane module. Heat and mass transfer equations are the fundamental part of MD modelling, so that analysing the equations is crucial in developing the model [62].

There are generally three types of MD modelling [61]:

- 1- 0-D models: 0-D models do not consider the changes in fluid conditions inside the module. Approximate fluid conditions and module properties are used as inputs in this type of model, and temperatures at feed and permeate side along the module do not change.
- 2- 1-D models: 1-D models divide the module into small elements along its length, so that in each element temperature and flow properties are allowed to change along the membrane.
- 3- 2-D models: 2-D models involve complex computational fluid dynamic approaches (CFD) to describe the heat and mass transfer across the feed and permeate channels and membrane as well as along the membrane. These kind of models need to be solved by detailed calculations that take longer time to solve than 1-D models, especially for large areas membrane modules [61]. 2-D models are useful when changes in flow and temperature occur in 2 dimensions, such as when wanting to understand module inlet conditions or when high fibre density leads to non-uniform flow and temperature distributions across hollow fibre membrane models.

2-D models focus on both axial and cross flow directions for different parameters such as concentration, temperature and velocity. For hollow fibre systems, the model is limited to fibre inside flow, whereas the 1-D model could be more capable of use in multiple ways [60]. 1-D model can be used to account for temperature and concentration polarization if programmed correctly. However, 2-D flow model is computationally expensive compared to 1-D model, and for flat sheet membranes with well-designed feed

inlets uniform flow across the membrane can be assumed. This is the case for the experiments considered here, and for most commercial flat sheet membrane modules. Therefore, only a 1-D model was considered.

5.2. Modelling Assumptions

Before evaluating the mass and heat transfer equations for the modelling the performance of MD, there are some assumptions required to simplify the coding for the 1-D model. These assumptions were:

- Heat loss neglected through the membrane module to the environment.
- The temperature gradient across the width of the membrane was neglected.
- Permeate mass passing the membrane is neglected as the single pass recovery is approximately 5%.
- Sensible heat transferred by the permeate is neglected.
- Concentration polarization effect was neglected due to the low concentration of salt used in the experiments compared to the concentration at which significant vapour pressure depression occurs. Hence, the model is only valid for low salt concentration.

5.3. Modelling Structure

Mathematical modelling for MD is used to predict process performance and analyse experiments using the equations that are stated below. The generation of the models should follow a structure that involves model derivation, model analysis and solution, as well as model validation as in [89]. Modelling derivation involved the use of heat and mass transfer equations to predict the performance of MD, and used membrane characteristics as parameters in the heat and mass transfer equations. This enabled the effect of membrane properties on membrane distillation performance to be obtained. Mathematical modelling structure consists of four steps which are [89],

- 1- Balance equations: Mass and energy balance
- 2- Transport transfer resistance model equations: Phase change, temperature and concentration polarization
- 3- Flow model equations: Mass and energy fluxes

4- Physical property model equations: Density, viscosity, thermal conductivity of the membrane etc [89].

Modelling needs to identify the processes that take place during MD. Balance equations account for mass and energy flows throughout the membrane module, and allowed temperature profiles to be predicted for the feed and permeate streams. Mass and energy fluxes were calculated under the flow model equations, as well as deriving the transport mechanism. Transport model equations are taken into account by considering the phase change and calculating the extent of temperature polarisation. When the equations are derived, they can be divided into sections: feed and permeate side of the membrane, and the membrane itself. Lastly, physical property model equations can be used for estimating the physical properties of pure components and solutions, and for estimating membrane properties such as thermal conductivity, and liquid properties such as density, viscosity and thermal conductivity. A 1-D model based on mass and heat transfer equations was applied and the equations were solved along the membrane for each x_{i+1} point from $x=0$ to $x=L$.

5.3.1. Mass and energy balance equations

Mass and energy balance equations not only consider conduction and diffusion, but also, they incorporate the flow regime [90]. Mass and energy balance equations for the membrane module that results in predicting the mass flow and temperatures at the feed and permeate side. Mass and energy balances are applied to small sections along the membrane so that changes in temperature along the membrane are taken into account, and the total energy and mass balances are the sum of the heat and mass flows from each section along the entire length of the membrane from $x=0$ to $x=L$ [89].

5.3.1.1. Mass balance

The mass balance was established using Eq. 5.1 and Eq. 5.2, which show the mass flow from the feed and to the permeate side, respectively, at steady state.

$$\frac{dmf}{dx} = -J_{total} \cdot W \quad (5.1)$$

$$\frac{dmp}{dx} = J_{total} \cdot W \quad (5.2)$$

where m_f is the mass flow rate on the feed side, m_p is the mass flow rate on the permeate side, w is the membrane width and J_{total} is the total flux through the membrane [60, 89]. The model assumes that the membrane is divided into N equal parts along its length, and calculates the mass transferred at each point along the membrane, x . For the initial point, $x=x_0$, the mass transferred from the feed and to the permeate is defined by Eq. 5.3 and Eq. 5.4 [89].

$$m_f(x=x_0) = m_{f,0} \quad (5.3)$$

$$m_p(x=x_0) = m_{p,0} \quad (5.4)$$

From the beginning point 1 to N , the mass flow from the feed and to the permeate sides is described for each components (i) by [91]:

$$\frac{dm_{f,i}}{dx} = -J_i \cdot w \quad \text{for } i = 1, \dots, N \quad (5.5)$$

$$\frac{dm_{p,i}}{dx} = J_i \cdot w \quad \text{for } i = 1, \dots, N \quad (5.6)$$

5.3.1.2. Energy balance

Eq. 5.7 and Eq. 5.8 describes the energy balance for membrane distillation and accounts for latent transferred to the permeate via the vapour, and for conductive heat transfer through the membrane.

$$\frac{dT_f}{dx} = -\frac{1}{V_f} \left[\frac{Q_{process}w}{c_{p_f}\rho_f} + \frac{J_{total}T_f w}{\rho_f} \right] \quad (5.7)$$

$$\frac{dT_p}{dx} = \frac{1}{V_p} \left[\frac{Q_{process}w}{c_{p_p}\rho_p} - \frac{J_{total}T_p w}{\rho_p} \right] \quad (5.8)$$

where $Q_{process}$ is the total heat flux along with the membrane, V_p and V_f are the volumetric flow rates on the permeate and feed side, respectively [65, 89]. Similar to the mass balance, the energy balance equations can be written as a function of membrane length. The initial conditions for the energy balance are as indicated in Eq. 5.9 and Eq. 5.10.

$$T_f(x=x_0) = T_{f,0} \quad (5.9)$$

$$T_p(x=x_0) = T_{p,0} \quad (5.10)$$

Along the membrane for each point, x_i , T_f and T_p temperatures change according to Eq. 5.11 and Eq. 5.12 [65].

$$\frac{dT_{f,i}}{dx} = T_{f,i} \cdot w \quad \text{for } i = 1, \dots, N \quad (5.11)$$

$$\frac{dT_{p,i}}{dx} = T_{p,i} \cdot w \quad \text{for } i = 1, \dots, N \quad (5.12)$$

5.3.2. Transport model (Transfer resistances) equations

Transport model equations describes the membrane-based separation process in which concentration and temperature polarization effect takes into place with the effects on the performance of the membrane distillation [89].

5.3.2.1. Mass transfer resistance

During the mass transfer, salt ions cannot pass through the membrane. This causes salt ions to accumulate in the feed, and the salt concentration near the membrane surface to increase. This phenomenon is termed concentration polarization [91]. Concentration polarization occurs in the MD feed channels and reduces the transmembrane flux. The Sherwood number, a dimensionless number, can be used as correction factor for concentration polarization. For low concentrations of feed solution, concentration polarization might be negligible as the vapour pressure is not greatly affected. Concentration polarization effect does not give burden computationally when it comes to modelling. However, because of the low concentration used in the experiments, concentration polarization phenomenon was neglected.

5.3.2.2. Heat transfer resistance

Heat transfer resistance in the boundary layer can be explained by temperature polarization. This can be modelled analogously to mass transfer. The heat transfer from bulk of the feed to the permeate side of the membrane can be described by simple heat transfer equations. To estimate the heat transfer coefficient, h_f , Nusselt's equations can be used.

Temperature polarization is the difference between interface temperatures and the bulk temperatures [1].

$$TPC = \frac{T_{mf} - T_{mp}}{T_{bf} - T_{bp}} \quad (5.13)$$

Heat flows from higher temperature to lower temperature by nature so that as the temperature difference increases the rate of the flow also increases [92]. A boundary layer is formed at the membrane surface on the feed and permeate sides, which creates resistance to the flow of heat and makes the temperatures at the interfaces lower than the temperatures in the bulk flows. This phenomenon also creates resistance for mass flux, which can result in lower mass fluxes [34].

Nusselt number is the function of Reynolds number, Prandtl number, d_h , length and viscosity of the solution. [93].

$$Nu = f(Re, Pr, d_h, L, \mu) \quad (5.14)$$

Nusselt's number is defined as:

$$Nu_i = \frac{h_i d_i}{k_i} \quad i=f, p \quad (5.15)$$

The Prandtl number is used as a correction factor for Nusselt number [24].

$$Pr = \frac{\mu C_p}{k} \quad (5.16)$$

$$Re = \frac{\rho u d}{\mu} \quad (5.17)$$

The particular Nusselt number chosen is related to flow regime in the channel [40, 63].

$Re < 2100$ Laminar Regime

$$Nu = 1.86 (Re Pr)^{1/3} \left(\frac{d_h}{L} \right)^{1/3} \quad (5.18)$$

$2100 < Re < 10000$ Transitional Regime

$$Nu = 0.116 (Re^{2/3} - 125) Pr^{1/3} \left[1 + \left(\frac{d_h}{L} \right)^{2/3} \right] \quad (5.19)$$

$Re > 10000$ Turbulent Regime

$$Nu = 0.023 Re^{4/5} Pr^{1/3} \quad (5.20)$$

5.3.3. Flow model equations

Flow model equations govern the mass and heat fluxes across the membrane. Transport of mass and energy occur simultaneously and in the same direction for MD [34]. For mass flux there are three steps that are regional mass fluxes, whereas for heat flux there are four steps for the membrane regions.

5.3.3.1. Mass flux

Mass flux can be defined as water vapour passing through the membrane from the feed to the permeate [9, 94]. Water vapor transports through the membrane pores, in which the process is driven by the partial vapor pressure difference between the feed and permeate [44]. For single layer membranes, the process occurs in the following steps [95]:

- (i) Mass transport through boundary layers at the feed side (subject to temperature and concentration polarization)
- (ii) Mass transfer through the membrane pores
- (iii) Mass transfer from membrane surface to the permeate phase (subject to temperature and concentration polarization)

As can be seen from the Fig. 5.1, water transports through 3 regions for single layer hydrophobic membrane [30].

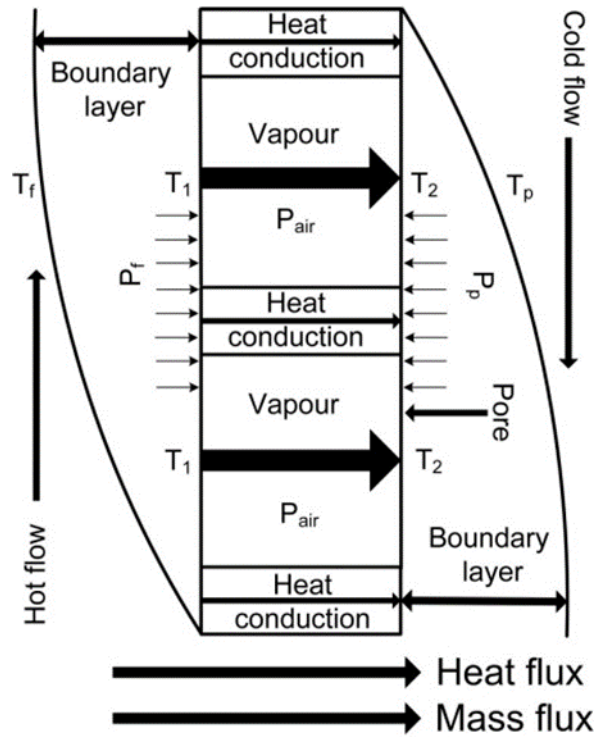


Figure 5.1. Membrane vapor transport regions [30]

Mass flux across the membrane can be calculated using Eq. 5.21. Mass flux depends on the mass transfer coefficient (C_m) and vapour pressure difference (ΔP_v).

$$J = C_m (p_{vm, f} - p_{vm, p}) \quad (5.21)$$

where C_m is the mass transfer coefficient and $p_{vm, f}$ and $p_{vm, p}$ are the partial pressures on the feed and permeate sides, respectively. Vapour pressures for water can be calculated by the Antoine equation shown in Eq. 5.22 [24].

$$p_v = \exp\left(23.328 - \frac{3841}{T-45}\right) \quad (5.22)$$

In the Eq. 5.22, p_v is the vapor pressure and T is the mean temperature at the membrane interface. Eq. 5.22 describes vapor pressure dependence on temperature.

Different types of transport mechanisms may occur through the membrane depending upon the pore size, with Knudsen diffusion, Molecular diffusion and a combination of Knudsen and molecular diffusion possible [11]. In DCMD, generally combined flow (Knudsen and molecular diffusion) describes mass transport through the membrane. Assigning of the appropriate model depends upon the Knudsen number [96].

$$K_n = \frac{l}{d} \quad (5.23)$$

If $K_n > 1$, Knudsen flow dominates and water vapour migration through the membrane pores can be described by Eq. 5.24 [97].

$$C_m = \frac{2}{3} \frac{\varepsilon_t r_{p,t}}{\tau_t \delta_t} \left(\frac{8M}{\pi RT} \right)^{1/2} \quad (5.24)$$

where ε_t , τ_t , $r_{p,t}$, δ_t are the porosity, pore tortuosity, pore radius and thickness of the membrane hydrophobic layer, respectively, C_m is the mass transfer coefficient, M is the molecular weight of water, R is the gas constant and T is the absolute temperature.

If $K_n < 0.01$, molecular diffusion dominates and mass transport through the membrane pores is described by Eq. 5.25.

$$C_m = \frac{\varepsilon_t}{\tau_t \delta_t} \frac{PD}{P_a} \frac{M}{RT} \quad (5.25)$$

where P_a is the air pressure, P is the total pressure inside the pore that is assumed constant and equal to the sum of the partial pressures of air and water vapour, and D is the water diffusion coefficient. The value of PD ($\text{Pa}\cdot\text{m}^2/\text{s}$) for water-air is calculated from Eq. 5.26 [24].

$$PD = 1.19 \times 10^{-4} T^{1.75} \quad (5.26)$$

Finally, in the transition region, $0.01 < K_n < 1$, mass transport occurs by a combined Knudsen/molecular diffusion mechanism, and mass transport is described by Eq. 5.27 [42, 89].

$$C_m = \left[\frac{3}{2} \frac{\tau_t \delta_t}{\varepsilon_t r_{p,t}} \left(\frac{\pi RT}{8M} \right)^{1/2} + \frac{\tau_t \delta_t}{\varepsilon_t} \frac{P_a}{PD} \frac{RT}{M} \right]^{-1} \quad (5.27)$$

5.3.3.2. Heat flux

5.3.3.2.1. Heat flux through hydrophobic single layer membrane

The heat through the hydrophobic single layer membrane is transferred passing 3 regions: bulk feed, membrane and bulk permeate. Ideal heat transfer for single and dual layer

membranes will be discussed in the following parts. The heat transport mechanism from the bulk feed to the bulk permeate can be found as below [47, 94, 98].

(i) Heat transferred from the feed solution to the membrane surface

$$Q_f = h_f (T_{b,f} - T_{m,f}) \quad (5.28)$$

(ii) Heat is transferred through the membrane by convective heat and conduction

$$Q_c = h_m (T_{m,f} - T_{m,p}) + J(\Delta H_v) \quad (5.29)$$

(iii) Heat transfer from the membrane surface to the permeate solution

$$Q_p = h_p (T_{m,p} - T_{b,p}) \quad (5.30)$$

Total heat transfer can be written as in Eq. 5.31 at steady state.

$$Q = Q_f = Q_m = Q_p \quad (5.31)$$

The overall heat transfer coefficient, U , can be calculated from Eq. 5.32. Q is a function of the overall heat transfer coefficient and the temperature difference between the feed and permeate bulk sides.

$$U = \frac{1}{\frac{1}{h_f} + \frac{k_m}{\delta} + \frac{1}{h_p}} \quad (5.32)$$

Overall heat flux is described by Eq. 5.33.

$$Q = \left(\frac{1}{h_f} + \frac{1}{h_m + (J_w \Delta H_v / (T_{m,f} - T_{m,p}))} + \frac{1}{h_p} \right)^{-1} (T_{b,f} - T_{b,p}) \quad (5.33)$$

Fig. 5.2 shows the occurrence of mass and heat transfer phenomena through hydrophobic membrane (a) and through hydrophobic/hydrophilic membrane [11].

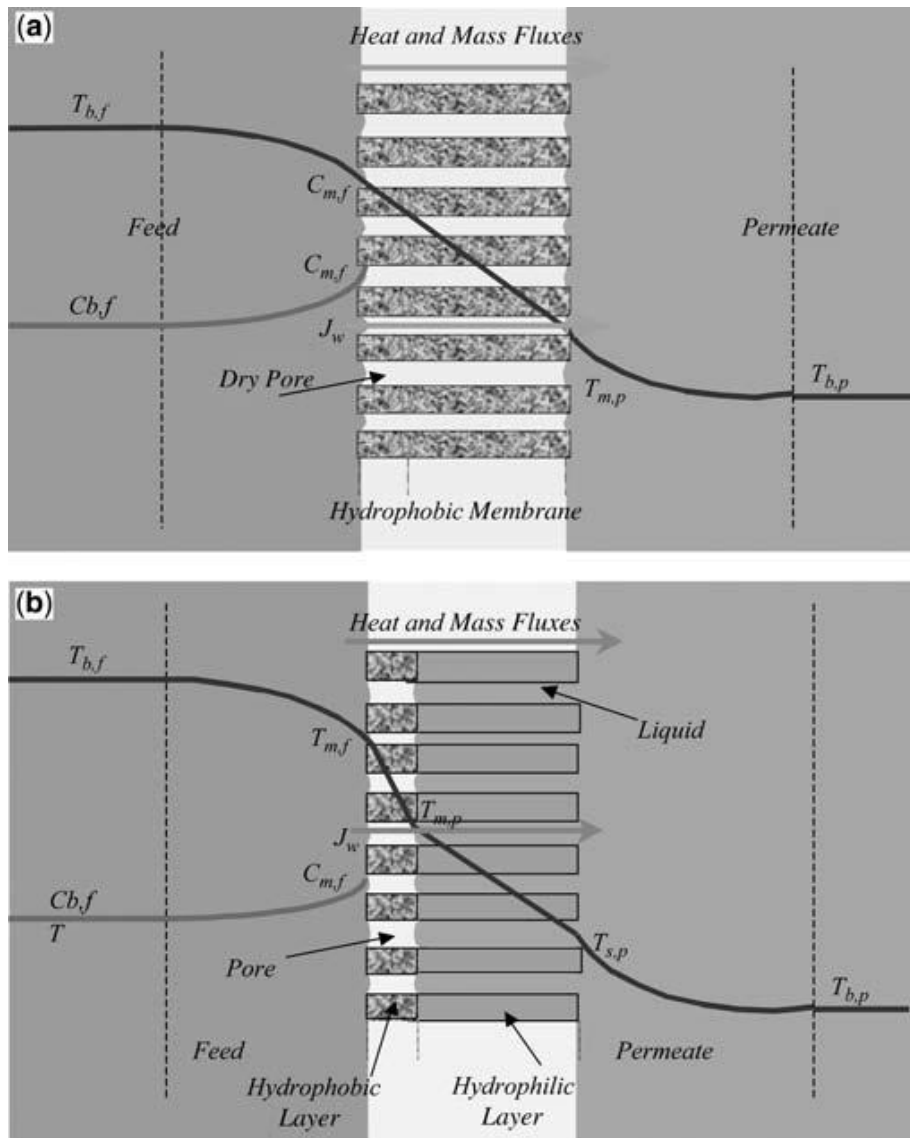


Figure 5.2. Diagram of the temperature and concentration profile through (a) hydrophobic membrane and (b) composite hydrophobic/hydrophilic dual layer membrane [11]

5.3.3.2.2. Heat flux through hydrophobic/hydrophilic dual layer membrane

Heat transport equations for hydrophobic/hydrophilic composite dual layer membranes for DCMD show differences because of the addition of one more transport region, which is the hydrophilic section of the membrane. Heat transfer is assumed to be conductive through the hydrophilic layer of the composite dual layer membrane unlike the heat transfer through dry hydrophobic layer's membrane pores.

For a membrane with a hydrophilic sub-layer supporting a hydrophobic top layer, water molecules' change phase to vapour (evaporation) at the hydrophobic top-layer of the membrane on the hot feed side. Water vapour then condenses at the boundary layer of the hydrophobic and hydrophilic layers [10], so that heat transfer through the hydrophilic sub-layer is by conduction only if the flow of water through this sub-layer is ignored. Ignoring the flow of water through the hydrophilic sub-layer is reasonable given the very slow flowrate expected.

(i) Heat transfer through boundary layer from the feed solution to the top-layer

$$Q_f = h_f (T_{b,f} - T_{m,f}) \quad (5.34)$$

(ii) Heat transfer through hydrophobic top-layer of the dual layer membrane

$$Q_t = h_t (T_{m,f} - T_{m,p}) + J_w \Delta H_v \quad (5.35)$$

(iii) Heat transfer through hydrophilic sub-layer of the membrane

$$Q_s = h_s (T_{m,p} - T_{s,p}) \quad (5.36)$$

(iv) Heat transfer through boundary layer to the permeate solution

$$Q_p = h_p (T_{s,p} - T_{b,p}) \quad (5.37)$$

where Q_f is the convective heat transfer in the feed boundary layer and Q_p is the convective heat transfer through permeate solution boundary layer; Q_t and Q_s are the heat transfer fluxes, respectively, through the hydrophobic top-layer and hydrophilic sub-layer of the membrane [13, 53], h is the heat transfer coefficient for each region of the membrane, J_w is the permeate flux, ΔH_v is the latent heat of vaporization and T is the absolute temperature. Bulk solution, feed, permeate, hydrophobic top-layer of the membrane and hydrophilic sub-layer are identified by the subscripts b , f , p , m and s , respectively [13].

At steady state, the overall heat flux through each layer is equal, so,

$$Q = Q_f = Q_t = Q_s = Q_p \quad (5.38)$$

$$Q = U (T_{b,f} - T_{b,p}) \quad (5.39)$$

U represents the overall heat transfer coefficient for the DCMD process.

Therefore, the heat flux can be written as [12, 13],

$$Q = \left(\frac{1}{h_f} + \frac{1}{h_t + (J_w \Delta H_v / (T_{m,f} - T_{m,p}))} + \frac{1}{h_s} + \frac{1}{h_p} \right)^{-1} (T_{b,f} - T_{b,p}) \quad (5.40)$$

$$U = \left(\frac{1}{h_f} + \frac{1}{h_t + (J_w \Delta H_v / (T_{m,f} - T_{m,p}))} + \frac{1}{h_s} + \frac{1}{h_p} \right)^{-1} \quad (5.41)$$

where ΔT is the bulk temperature difference between the feed and permeate, $T_{b,f}$ and $T_{b,p}$, respectively. The convective heat transfer coefficients can be estimated by using dimensionless numbers' correlations.

$$Nu = a Re^b Pr^c \left(\frac{\mu_b}{\mu_m} \right)^d \quad (5.42)$$

where Nu, Re and Pr are Nusselt, Reynolds and Prandtl dimensionless numbers, respectively; a, b, c and d are characteristics constants of the liquid flow regime, and μ_b and μ_m represents water dynamic viscosity in the bulk and at the corresponding side of the membrane, respectively [13].

The conductive heat transfer coefficients of the hydrophilic sub-layer (h_s) and hydrophobic top-layer (h_t) can be calculated from the following Eq. 5.43 and 5.44.

$$h_s = \frac{k'_s}{\delta_s} = \frac{k_w \varepsilon_s + k_s (1 - \varepsilon_s)}{\delta_s} \quad (5.43)$$

$$h_t = \frac{k'_t}{\delta_t} = \frac{k_g \varepsilon_t + k_t (1 - \varepsilon_t)}{\delta_t} \quad (5.44)$$

Where k_s , k_w , k_t , k_g are the thermal conductivities of the hydrophilic membrane polymer, water in the pores, hydrophobic membrane polymer and the gas contained in the pores; δ_s , δ_t , ε_s , ε_t are the thickness and porosity of the hydrophilic and hydrophobic layer of the composite membrane, respectively.

When predicting the thermal conductivity of the membrane, three different models can be used: 1. Isostrain (parallel model), 2. Isostress model, 3. Flux law model, which can be found calculated from the equations below [62, 99].

$$k_m = (1 - \varepsilon)k_s + \varepsilon k_g \quad \text{Isostrain model} \quad (5.45)$$

$$k_m = \left[\frac{\varepsilon}{k_g} + \frac{(1-\varepsilon)}{k_s} \right]^{-1} \quad \text{Isostress model} \quad (5.46)$$

$$k_m = k_g \left[\frac{1+(1-\varepsilon)\beta_{s-g}}{1-(1-\varepsilon)\beta_{s-g}} \right] \quad \text{Flux law model} \quad (5.47)$$

$$\beta_{s-g} = \frac{\frac{k_s}{k_g} - 1}{\frac{k_s}{k_g} + 2} \quad (5.48)$$

In this work, the Isostrain model was chosen to calculate the thermal conductivity of the membrane. The Isostrain model is often chosen for MD, because of its high accuracy for calculating the thermal conductivity of the membrane in the model [62].

5.3.4. Physical property model equations

Equations to describe the physical properties of solutions and air were located from general literature sources, and were used to describe pure component or solution properties. This allowed these properties to be calculated at the different temperatures along the membranes. Table 5.1 shows the equations used within the model to describe the properties of water and air as a function of temperature [100].

Table 5.1. Equations used to describe the physical properties of water

Water properties	Correlations	Regression Coefficients	Source
Density (g/ml)	$AB^{-\left(1-\frac{T}{T_c}\right)^n}$	A=0.34710 B=0.27400 n=0.28571 T _c =647.13	[100]

Viscosity (μP)	$\log_{10}\mu=A+B/T+CT+DT^2$	$A = -10.21158$ $B = 1.7925 \times 10^{-3}$ $C = 1.7730 \times 10^{-2}$ $D = -1.2631 \times 10^{-5}$	[100]
Air Viscosity (μP)	$A+BT+CT^2$	$A=9.1445$ $B=0.029257$ $C=0.000019067$	[100]
Heat Capacity ($\text{J}/(\text{mol.K})$)	$A+BT+CT^2+DT^3$	$A=92.053$ $B=-3.9953 \times 10^{-2}$ $C=-2.1103 \times 10^{-4}$ $D=5.3469 \times 10^{-7}$	[100]
Heat of Vaporization (kJ/mol)	$A+BT+CT^2+DT^3$	$A=2327.3$ $B=1.4317$ $C=0.010953$ $D=1.2365 \times 10^{-5}$	[1]
Thermal Conductivity $\text{W}/(\text{m.K})$	$A+BT+CT^2$	$A=0.2758$ $B=4.6120 \times 10^{-3}$ $C=-5.5391 \times 10^{-6}$	[100]

5.3.5. Spacer modelling

Spacers induce turbulent flow, which increases mass and heat transfer by reducing the boundary layer thickness next to the membrane. This mechanism can increase flux by 50% [99]. The presence of the spacer creates recirculation regions in which high velocity can be reached and temperature polarization can be decreased [101]. The spacer design used in the MD module is shown in Fig. 5.3, where θ is the angle between the fibres, l_m is the length between the parallel fibres, h_{sp} is the height of the module and d_f is the diameter of a single spacer fibre [30].

Velocity can be calculated from Eq. 5.49, where A is the cross-sectional area, and Q is the flow rate of feed or permeate [1].

$$u = \frac{Q}{A\varepsilon_{spacer}} \quad (5.49)$$

Eq. 5.50 is used to calculate ε_{spacer} .

$$\varepsilon_{spacer} = 1 - \frac{\pi d_f^2}{2l_m h_{sp} \sin\theta} \quad (5.50)$$

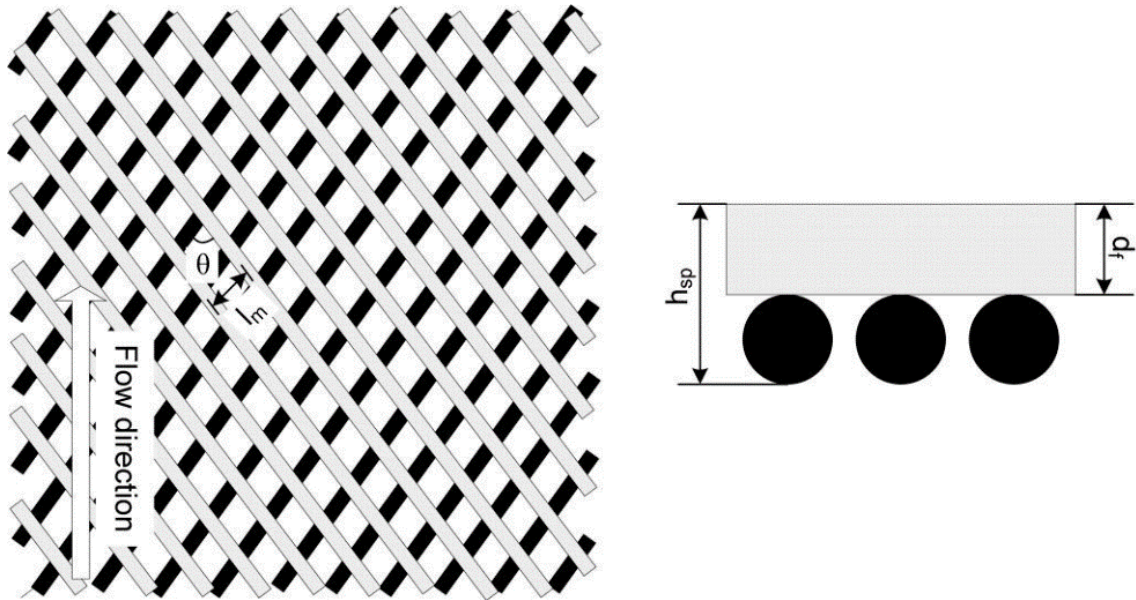


Figure 5.3. Spacer figure [1]

After calculation of the spacer porosity, specific surface of the spacer (S_p) can be calculated by Eq. 5.51 [1].

$$S_{spacer} = \frac{4}{d_f} \quad (5.51)$$

The hydraulic diameter, d_h is calculated by following Eq. 5.52 [1].

$$d_h = \frac{4 \varepsilon_{spacer}}{\left(\frac{2}{h_{sp}}\right) + (1 - \varepsilon_{spacer}) S_{spacer}} \quad (5.52)$$

where h_{sp} is the spacer thickness.

A correction factor for the spacer, K_s is used for Nusselt number correction for spacer filled channels [63].

$$Nu_s = K_s Nu \quad (5.53)$$

$$\text{where, } K_s = a \left(\frac{d_f}{h_{sp}}\right)^c \varepsilon_{spacer}^d \left(\sin \frac{\theta}{2}\right)^e \quad (5.54)$$

Coefficients, a , c , d , e that are used in Eq. 5.54 can be taken as 1.9, 0.039, 0.75 and 0.086, respectively [63].

5.4. Experimental and Methods

Mathematical modelling was conducted using MathWorks MATLAB R2017a program. The heat and mass transfer equations were coded in the modelling program in order to calculate mass and heat flux. The model predicted the permeate flux and energy efficiency for MD. To solve the equations, co-current flow had one calculation loop within the program, while counter-current flow had two calculation loops in order to find the correct permeate outlet temperature for the system.

5.4.1. Modelling algorithms

Performance modelling for DCMD was performed using both co-current and counter-current flows. Flow diagrams for solving the equations outlined previously for both co-current and counter-current flow are depicted in Fig. 5.4 and Fig. 5.5 [1, 91, 98]. For co-current flow, acceptance limit was within 3%, whereas for counter-current flow it was within 5% between two iterations.

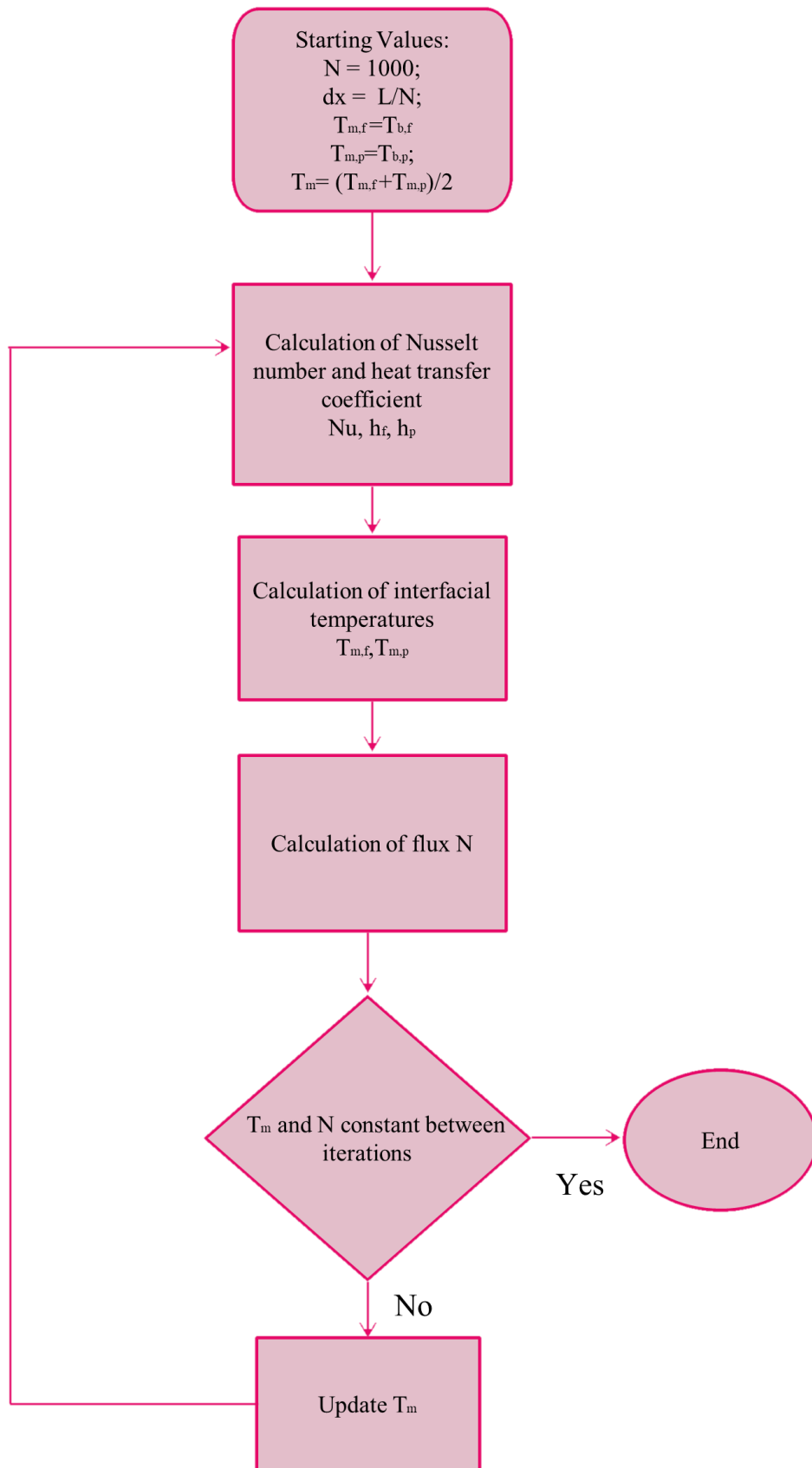


Figure 5.4. Diagram of the modelling algorithm for simulation of co-current DCMD

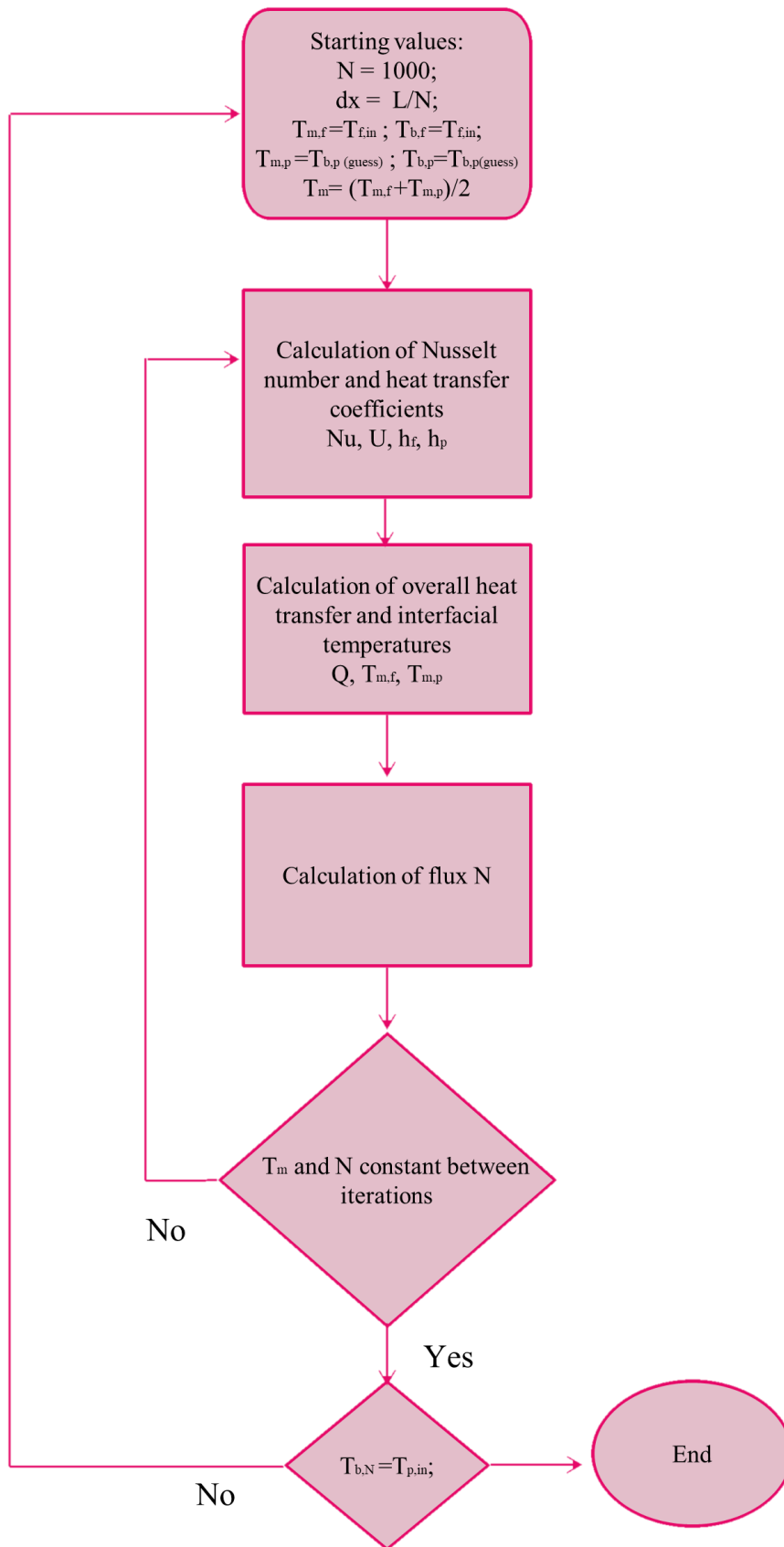


Figure 5.5. Diagram of the modelling algorithm for simulation of counter-current DCMD

5.4.2. Modelling inputs

Modelling inputs for spacer and flow channel for single and dual layer membranes can be found in Table 5.2. W1 defines the module width dimension that was used for M1, M2, M3, M4 membranes, whereas W2 defines the width of the module that was used for M5 membrane.

Table 5.2. Spacer and module dimensions

Flow Channel (mm)			Spacer (mm)			
Length (L)	Width		Depth (D)	Filament diameter (d _f)	Thickness (h _{sp})	Mesh size (l _m)
	(W1)	(W2)				
135	135	95	0.8	0.4	0.8	3

Thermal conductivities for membranes used in modelling can be found in Table 5.3 [102].

Table 5.3. Membranes and their thermal conductivities

Membranes	Thermal conductivities (Wm ⁻¹ K ⁻¹)
PTFE	0.25
PE	0.11
PVDF	0.19
O-PE	0.11
Nylon-6	0.25

5.5. Results and Discussion

Modelling was done for M1, M2 and M3 single layer membranes and for M5 as dual layer membrane. Mass and heat transfer coefficients were calculated by numerically solving heat and mass transfer equations. Flux and energy efficiencies of the membranes were predicted, and model validation were done between modelling results and experimental results for M1, M2, M3 and M5.

5.5.1. Temperature profiles for co- and counter-current flows along the membrane length

Temperature profiles of the single and dual layer membranes were observed along the membrane length. Temperature profiles for single layer membrane were generated at feed velocity of 0.093 m/s and feed and permeate inlet temperatures at 60 and 20 °C, respectively. Temperature profile for single layer membrane with co-current flow can be seen in Fig. 5.6. T_{bf} and T_{bp} are the bulk temperatures at the feed and permeate side, and T_{mf} and T_{mp} are the membrane interface temperature at the feed and permeate, respectively. Temperatures at the interfaces of the single layer membrane were calculated by the model.

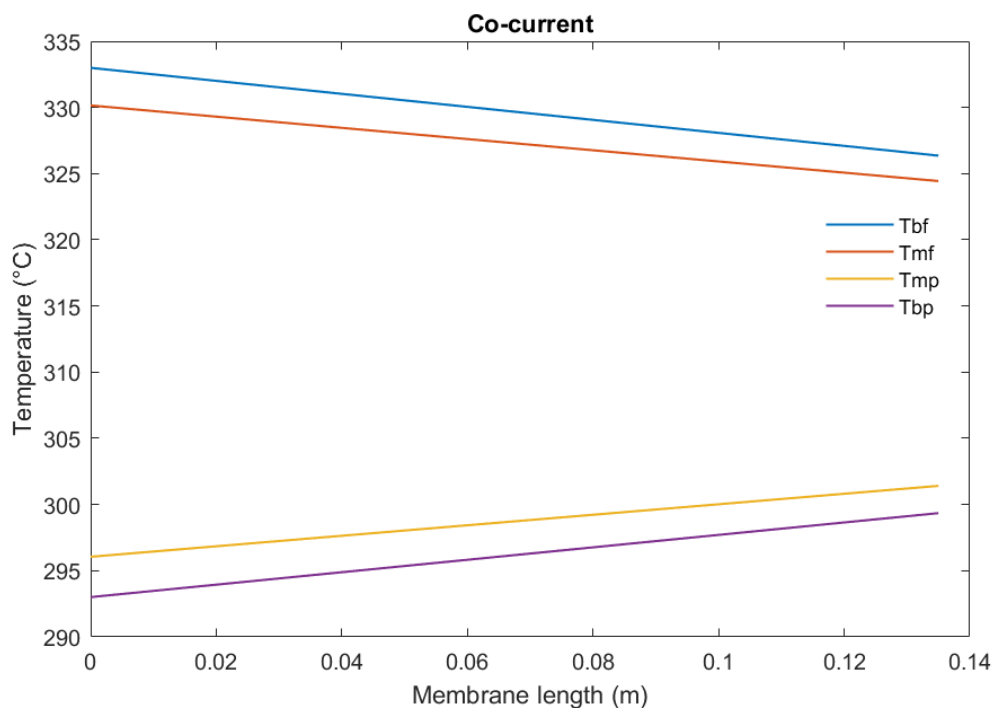


Figure 5.6. Temperature profile for co-current flow of single layer membrane

Fig. 5.7 shows the temperature profile along the membrane module of single layer membrane with counter-current flow. As a difference from co-current, temperature change between feed and permeate bulk is decreasing parallel each other, whereas with co-current temperatures are approaching each other.

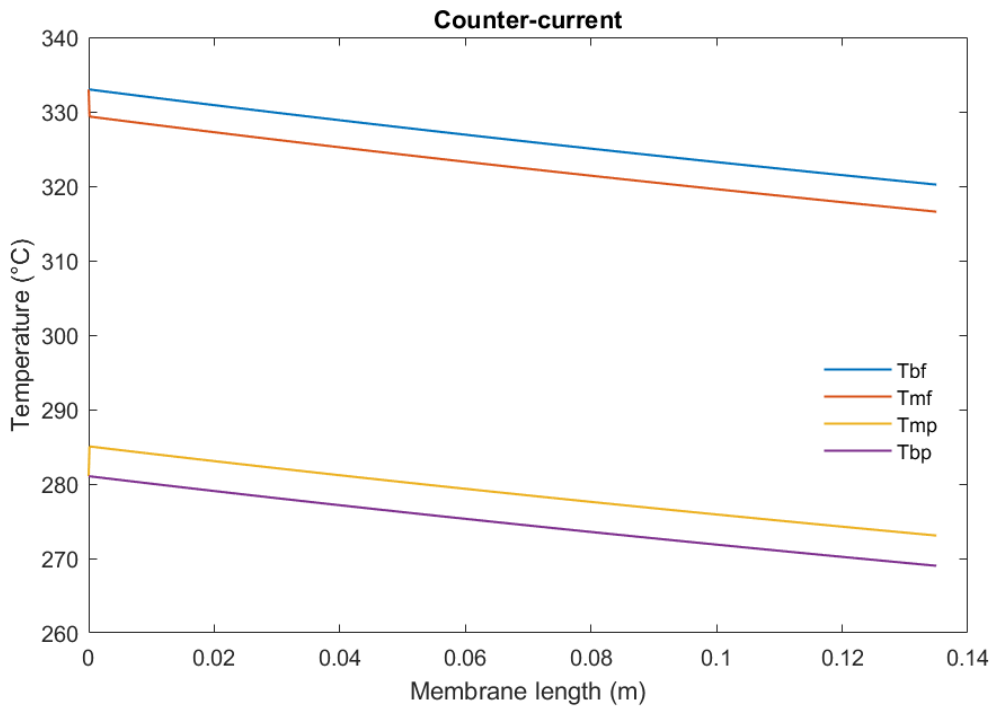


Figure 5.7. Temperature profile for counter-current flow of single layer membrane

Initial temperature difference between feed and permeate bulk solutions was higher with counter-current flow compared to co-current flow, but reduces as the feed solution moves along the membrane. However, greater temperature difference between feed inlet and permeate can reduce the thermal efficiency for DCMD.

Temperature profile of dual layer membrane M5 for co-current flow along the membrane can be seen in Fig. 5.8.

Temperature profiles for single and dual layer membranes were found to be similar. However, temperature profile for M5 has another temperature point between the interfaces of hydrophilic layer and permeate solution, which is T_{sp} .

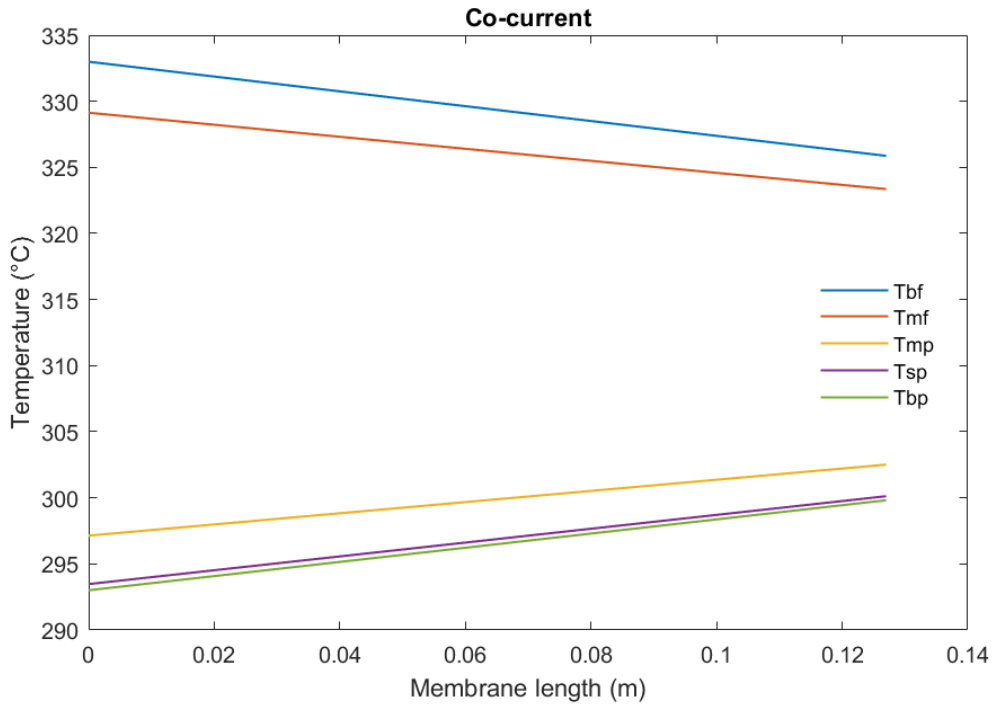


Figure 5.8. Temperature profile of co-current flow for M5

Fig. 5.9 shows temperature profile along with membrane length for counter-current flow of M5 dual layer membrane. As in single layer membranes' counter-current temperature profile, temperatures decrease was parallel.

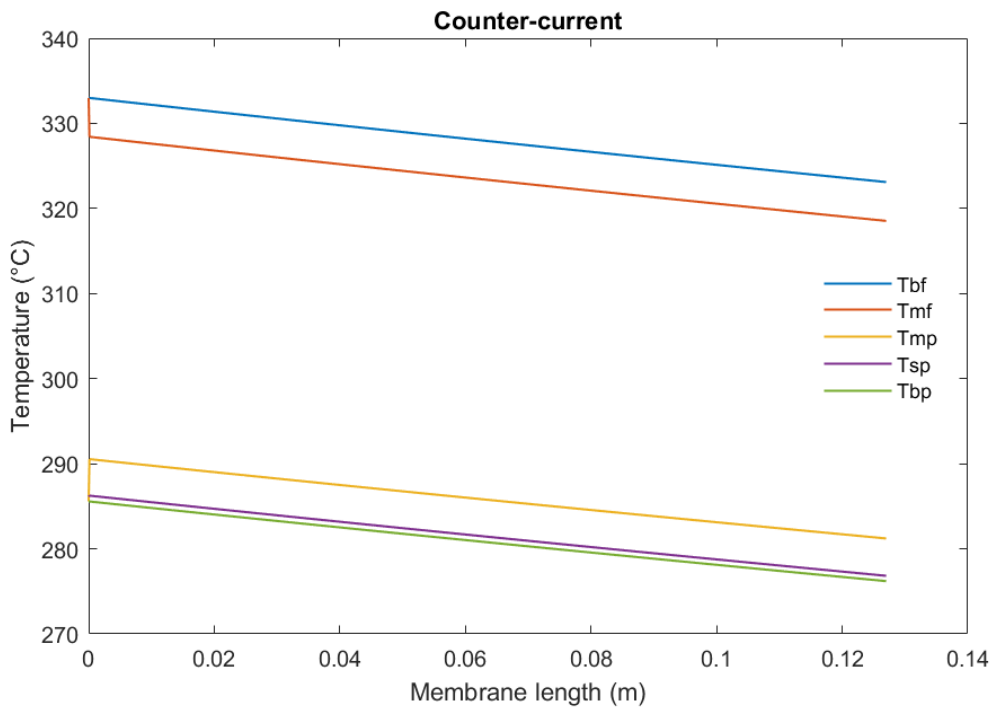


Figure 5.9. Temperature profile for counter-current flow of M5

Temperature difference between T_{sp} and T_{bp} was observed to be very small because the thin hydrophilic layer of the membrane was filled with water, in which only conductive heat transfer takes place without latent heat transfer.

The temperature difference between interface and bulk temperatures was higher for dual layer membrane, which increases the temperature polarization coefficient according to Eq. 5.13. This effect can be a limitation for heat transfer across dual layer membrane because of the additional hydrophilic layer as it increases conductive heat transfer, and reduces the thermal efficiency for the membrane. Therefore, dual layer membrane performance for permeate flux and energy efficiency were lower compared to single layer membranes.

5.5.2. Model verification

Model validation was done for M1, M2, M3 and M5 membranes. In the graphs, dots represent experimental results, while lines represent modelling results.

5.5.2.1. Flux prediction at different feed velocities

Model was used to predict the flux at different feed velocities in DCMD. Increasing the flowrate also increased the MD flux due to enhanced turbulence along the channels. Fig. 5.10 showed flux change at different feed velocities for all membranes at 60°C feed inlet and 20°C permeate inlet.

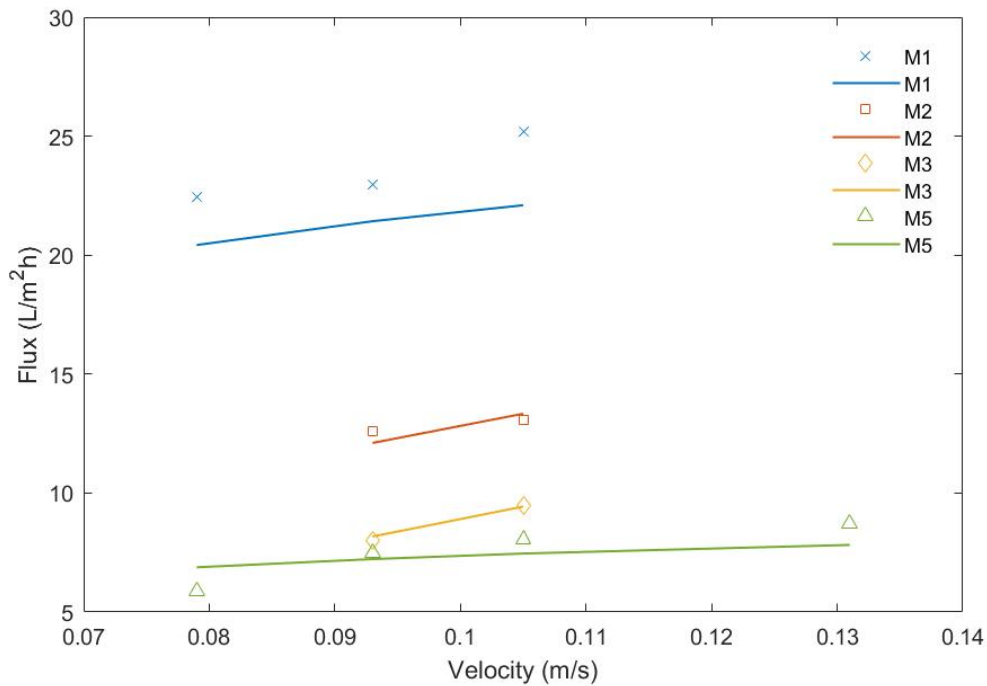


Figure 5.10. Flux versus velocity at 60°C hot and 20°C cold inlet with co-current flow

Flux was predicted within 10% error at different velocities. Increasing the velocity from 0.079 m/s to 0.105 m/s increased the MD permeate flux slightly for all membranes with co-current flow. Model achieved success while predicting the fluxes for co-current flow. M5 had the lowest flux amongst the other membranes. Operating the velocity at 0.131 m/s for M5 did not increase the flux significantly compared to the velocity at 0.105 m/s.

Fig. 5.11 showed flux versus feed velocities for the membranes keeping the temperatures of hot inlet at 60°C and cold inlet 20°C while varying the velocities with counter-current flow.

The highest flux at all different velocities was achieved with M1 membrane. Flux increment trend for all membranes with counter-current flow was similar to the trend with co-current flow. After M1 membrane, M2 had the second highest flux among the other membranes. It is worth mentioning that dual layer membrane, M5, achieved lower flux for both flow modes compared to the other membranes.

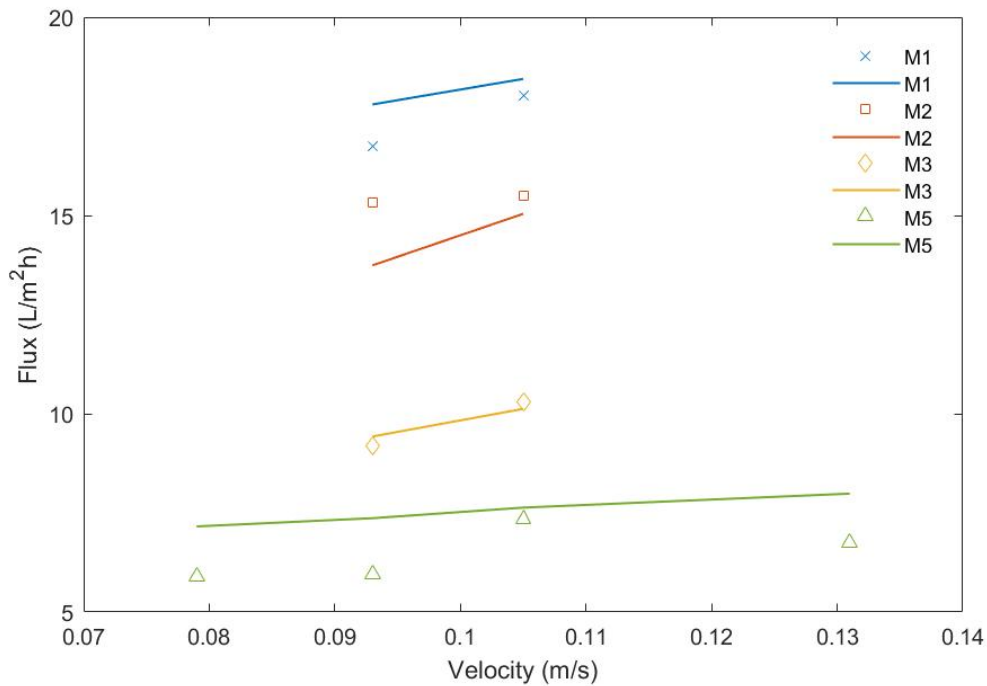


Figure 5.11. Flux versus velocity at 60°C hot and 20°C cold inlet with counter-current

5.5.2.2. Flux prediction at different inlet temperatures

Predicting the MD permeate flux was done using 1-D model with four membranes, which are M1, M2, M3 and M5. Lines in the graphs represent modelling results, whereas dots show the experimental results. Different feed inlet and permeate inlet temperature effects on flux were modelled. While different feed inlet temperatures were examined for co- and counter-current flow, just co-current flow was tested for different permeate inlet temperatures. Fig. 5.12 shows the model validation for flux in different feed inlet temperatures with co-current flow.

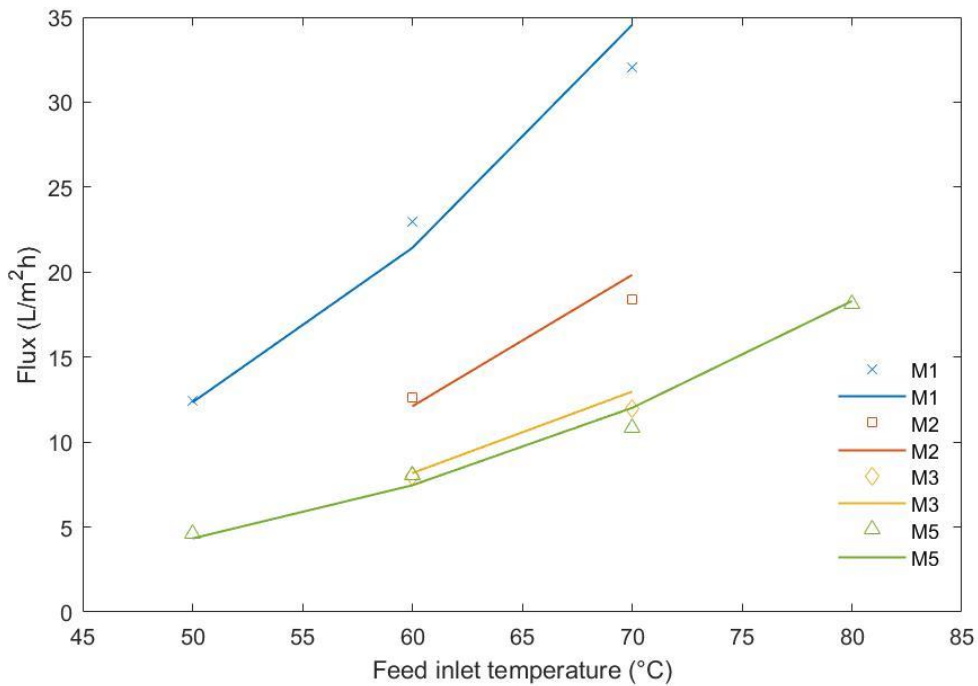


Figure 5.12. Flux versus feed inlet temperature with co-current flow

As it can be seen from Fig. 5.12, the model predicted the MD flux with high accuracy for membranes at different feed inlet temperatures.

Increasing the feed temperature while keeping the permeate temperature at 20°C increased the MD flux for all membranes. The increment trend for M1 was higher than the other membranes. Under the same operating temperatures, the flux was also higher than the other membranes for co-current flow. Lowest flux was achieved for M5. The flux at 80°C for M5 was not higher than the flux at 70°C for M1.

Fig. 5.13 showed the flux change with different feed inlet temperatures for counter-current flow. Increment trend for M1 membrane was more linear than the other membranes, and also flux was higher than the others. Increasing the temperature increased the flux for all membranes for counter-current flow.

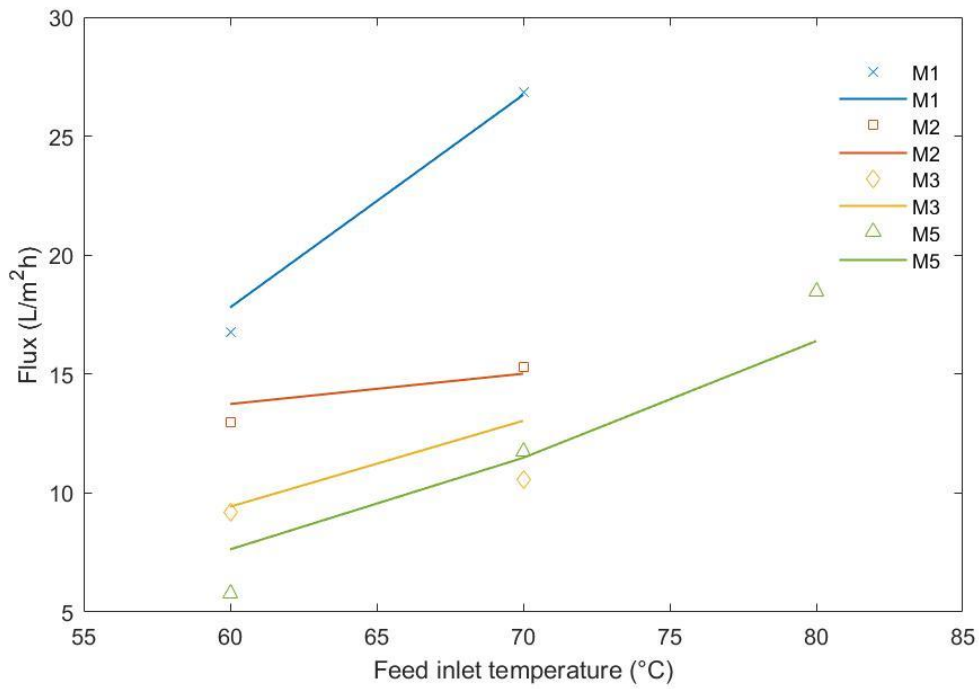


Figure 5.13. Flux versus feed inlet temperature with counter-current flow

Fig. 5.14 shows flux change with different permeate inlet temperatures for co-current flow. Experiments were performed for M1 and M5 membranes at different permeate inlet temperatures. Verification of the model was within 10% error at different permeate temperatures. Experimental results for M1 and M5 was higher than the result in the model at 10°C.

Increasing permeate temperature reduced the flux while keeping the feed temperature at 60°C for the membranes. The reason was reducing the temperature difference across the membrane resulted in reducing the pressure difference.

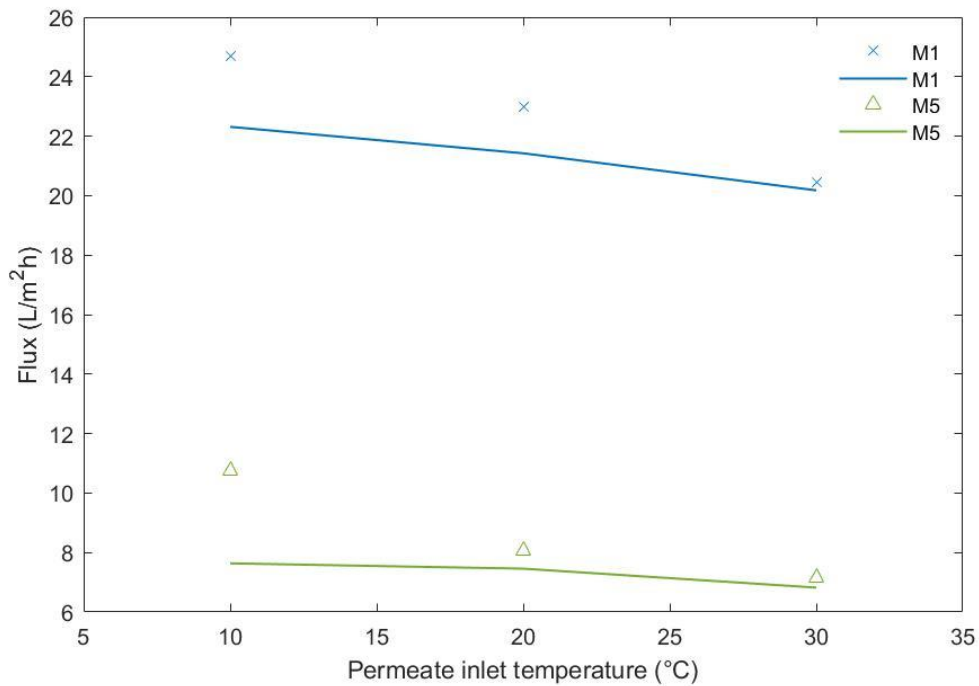


Figure 5.14. Flux versus permeate inlet temperature with co-current flow

Among the membranes, the fluxes for dual layer membranes were lower than the fluxes for single layer membranes with different velocities and different feed and permeate inlet temperatures. Lower flux for M5 dual layer membrane can be related to heat and mass transfer coefficients based on the membrane characteristics. Having higher thickness and relatively smaller pore is a limitation for heat and mass transfer across the membrane for M5. Thicker hydrophobic layer than the hydrophilic layer limited the mass transfer across the membrane so that lowered the permeate flux. Moreover, an additional hydrophilic layer caused more heat loss and it increased temperature polarization on the permeate side.

5.5.2.3. Validation of energy efficiency at different temperatures

The energy efficiency of MD for different membranes was modelled and results verified with the experimental results. Single and dual layer membranes demonstrated different efficiency for MD. Being energy efficient for DCMD is crucial factor for the membranes when choosing the right membranes for the process. Energy efficiency of MD was variable at different feed inlet temperatures for different membranes. Prediction was done using modelling flux and temperature difference between feed inlet and feed outlet.

However, thermal efficiency for the experiments were calculated from the experimental flux and temperature difference between feed inlet and outlet during the experiment.

Thermal efficiency was affected by permeate flux and temperature difference between feed inlet and outlet.

Fig. 5.15 demonstrated the energy efficiency of DCMD for all membranes at different temperatures with co-current flow. Feed inlet temperature increment enhanced the thermal efficiency of the process. Modelling results showed accuracy with the experimental results. From Fig. 5.15, M1 membrane performed better thermal efficiency than the other membranes.

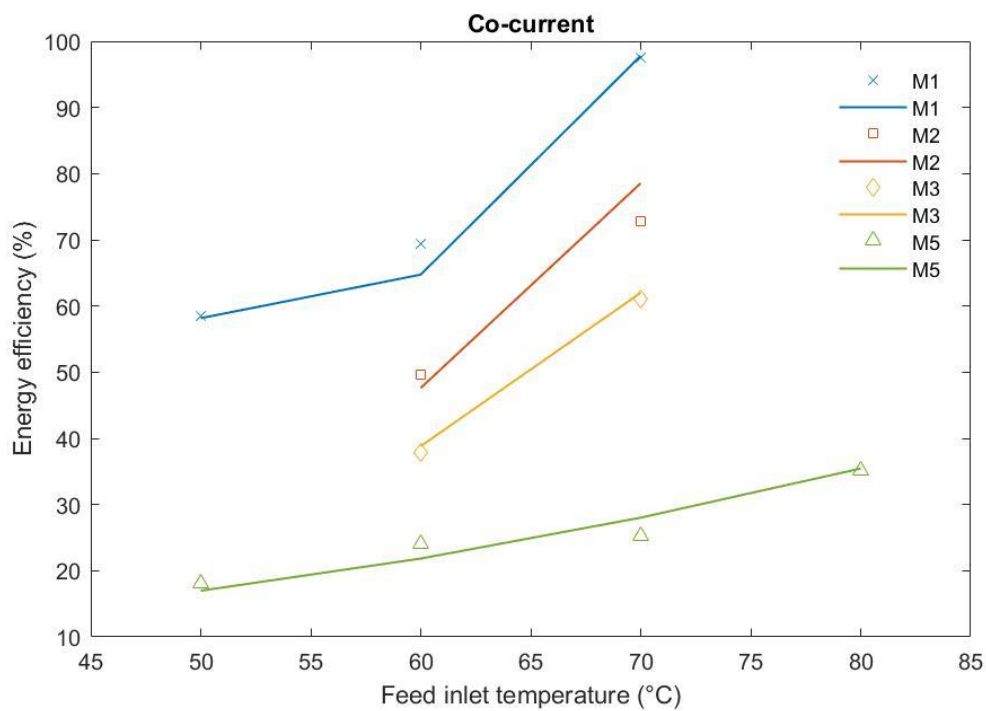


Figure 5.15. Energy efficiency at different feed inlet temperatures with co-current

Fig. 5.16 showed the thermal efficiencies for the membranes at feed inlet different temperatures for counter-current flow. Thermal efficiencies were similar values for M3 and M5 membranes. However, M5 membrane was the least thermally efficient membrane for DCMD.

For co- and counter-current flow, dual layer membranes were less efficient than single layer membranes. Hydrophobic layer thickness of M5 caused more heat loss across the

membrane compared to thinner layer membrane. Greater thickness of the layer reduced the conductive heat transfer coefficient.

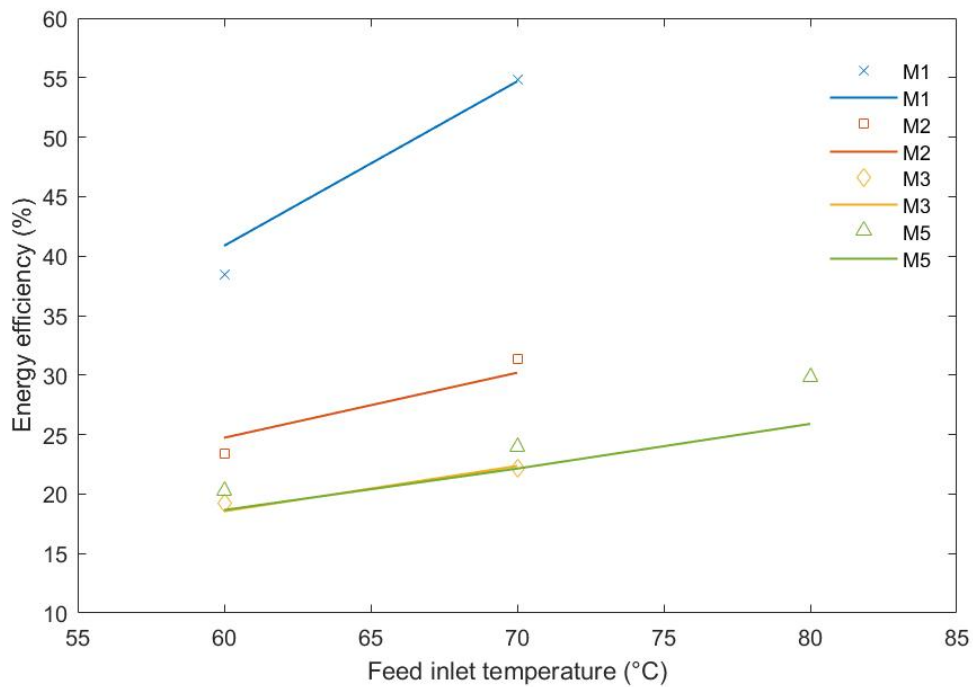


Figure 5.16. Thermal efficiency at different feed inlet temperatures with counter-current

Energy efficiencies for the membranes with counter-current flow were lower than for co-current flow. The reason was higher temperature difference between feed inlet and feed outlet due to the flow directions leading to greater localised temperature polarization. Temperature increases for DCMD also increased the thermal efficiencies for all the membranes.

The correlation between membrane characteristics ϵ/bt and the flux/energy efficiency can be found in Fig. 5.17.

Thermal efficiency of the membranes can be increased by increasing the membrane pore size and porosities, which can lead to higher flux. The thickness also has a significant effect on membrane performance for permeate flux and energy efficiency. The thickness was the highest for M5 among the membranes, so that it limited mass transfer across the membrane because of longer the path for evaporation of water molecules.

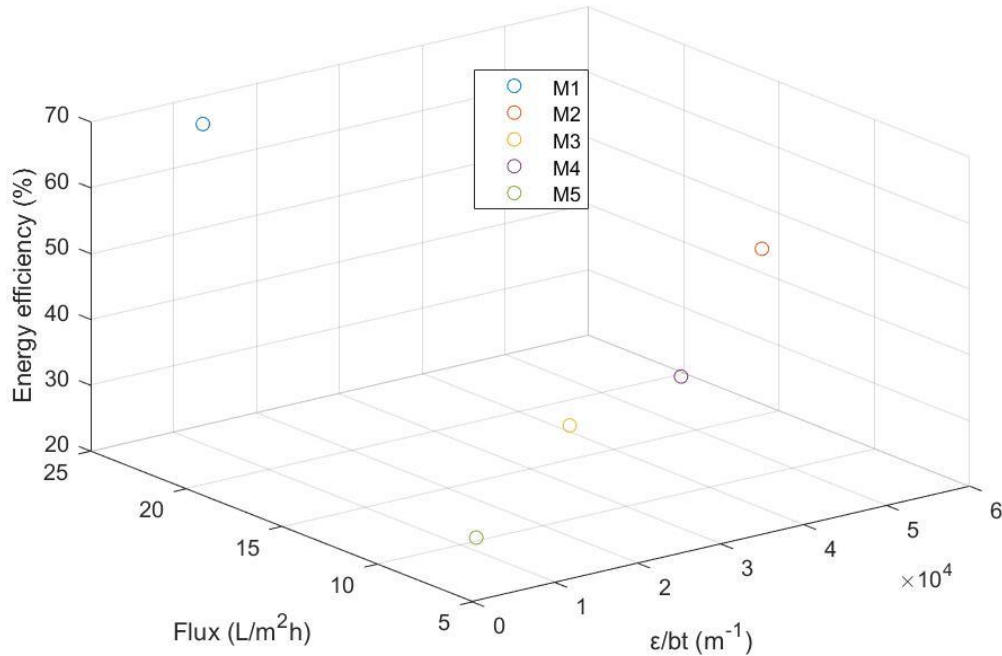


Figure 5.17. Correlation between ϵ/bt and flux/energy efficiency at 60°C feed and 20°C permeate inlet temperatures

The most energy efficient membrane was found as M1 membrane. The membrane had the highest porosity among the other membranes, and this characteristic reduced heat losses by lowering the thermal conductivity of the membrane material. It also increases mass transfer by providing reduced resistance to flow. Lower flux and energy efficiency can be related to its lower mean pore size, although M5 dual layer high porosity. Increased thickness for M5 was another factor for lower flux. The additional hydrophilic layer also increased the heat loss, which also resulted in lowering the energy efficiency of the membrane.

5.6. Summary

Performance modelling of the single layer hydrophobic membranes and dual hydrophobic/hydrophilic membrane was done using 1-D model in MATLAB. Permeate fluxes and energy efficiencies were predicted with the model for membranes. Heat and

mass transfer equations for single and dual layer membrane showed differences due to additional hydrophilic layer for M5. The equations were derived for dual layer membrane M5, and coded in the model. Mass transfer coefficient for the model was calculated taking the hydrophobic top layer characteristics while the hydrophilic layer was considered to be filled with water. However, the hydrophilic layer was included in the heat transfer equations, and its characteristics such as porosity and thickness used for calculating the heat transfer coefficients.

Temperature profiles for co- and counter-current flows for single and dual layer membranes were calculated. While temperatures approaching each other for co-current flow, parallel temperature profiles were observed for counter-current flow. Temperature at the interface of hydrophilic layer and permeate (T_{sp}) was included for M5. Using T_{sp} value allowed calculation of the heat transfer through hydrophilic layer (Q_{sp}) for M5.

The permeate flux was predicted at different velocities for co-current flow for the membranes, except M4. However, the fluxes and thermal efficiency were shown in the graphs for M4 from experimental results. Highest flux was achieved with M1 membrane with both flow modes, followed by M2 and M3 single layer membranes. Oleophobic layer made some difference to porosity and thickness which led to reduce C_{global} . Moreover, M1 had the highest porosity, the largest pore size and the lowest thickness, which enhanced the mass transfer coefficient resulted in high flux. Lowest flux was recorded for M5 with co- and counter-current flow at different velocities. Although M5 had higher porosity, the thickness of the membrane limited the mass and heat transfer by reducing the mass and heat transfer coefficients.

The permeate flux for the membranes were predicted with high accuracy (error within 10%) at different temperatures. Increment for temperature increased the fluxes for all membranes. M1 had the highest flux amongst the other membranes. Membranes performed better with co-current flow compared to counter-current flow. Fluxes at different permeate inlet temperatures were predicted for M1 and M5, and increasing the permeate temperature decreased the flux for both membranes.

Energy efficiencies at different feed inlet temperatures for the membranes were predicted and validation was done comparing the modelling results with the experimental results. Energy efficiencies were lower for counter-current compared to co-current. Most efficient

membrane was chosen as M1 with co- and counter-current flow. Thermal efficiencies for dual layer membranes were lower compared to dual layer membranes. This can be explained by heat loss through hydrophilic layer across the membrane as related to their thicknesses.

Model accuracy at different velocities and different feed and permeate inlet temperatures was within 10%. Model predicted the flux at different temperatures better than at different velocities due to the sensitivity of the model and process sensitivity. At feed and permeate velocities considered in the experiments, good mixing occurred so variation on velocity had little impact on flux or thermal efficiency.

CHAPTER 6. CONCLUSION AND RECOMMENDATIONS

6.1. Introduction

This study was to numerically model the hydrophobic/hydrophilic dual layer membranes and to identify their distinctive factors that separates them from hydrophobic single layer membranes. Objectives proposed for this work were:

- ❖ Identification of single and dual layer membranes characteristics via measurement of parameters such as porosity, mean pore size, maximum pore size, thickness, the LEP that have effects on permeate flux and thermal efficiency,
- ❖ Derivation of heat and mass transfer equations for single layer hydrophobic and hydrophobic/hydrophilic dual layer membranes,
- ❖ Experimental DCMD tests for five membranes to observe their performance under different flowrates, feed and permeate inlet temperatures for validation of the models developed, and
- ❖ Modelling the performance of DCMD with different membranes based on membrane characterization parameters and heat and mass transfer equations using a 1-D model to predict the flux and energy efficiency for MD using dual layer membranes.

Objectives for this work were undertaken in the previous chapters. The mathematical modelling of hydrophobic/hydrophilic dual layer membranes with 1-D modelling has never been done before, which makes this work unique. MATLAB was used for coding of the performance modelling program. Heat and mass transfer equations were compiled from previous studies that considered modelling of hydrophobic/hydrophilic dual layer membranes. The equations for dual layer membranes were different because of additional hydrophilic layer. The hydrophilic layer of the membrane was assumed to be filled with water in the pores, so that the hydrophilic layer was neglected when calculating the mass transfer coefficient, while the hydrophobic layer membrane characteristics were used for the calculation. However, for calculation of the heat transfer coefficients, heat transfer through hydrophilic layer was assumed as conductive heat transfer, and characteristics of the hydrophilic layer such as thickness and porosity were used for these calculations.

The modelling was done for the membrane with facing of the hydrophobic layer on feed side as in the experiments.

6.2. Outcomes

The numerical modelling of dual layer membranes was the aim of this work. Five membranes were used for this study, which were PTFE (M1), PE (M2), O-PE (M3), PU-PTFE (M4) and PVDF-co-HFP-N6 (M5). M1 membrane was PTFE active layer with PP support layer. M2 membrane was symmetric PE membrane. M3 membrane was symmetric oleophobic coated PE membrane (oil-repellent). M4 was polyurethane dense coated PTFE dual layer membrane. M5 was copolymerized PH Electrospun with Nylon-6 dual layer membrane. M1, M2 and M3 were the single layer membranes, whereas M4 and M5 were the dual layer membranes.

Mass and heat transfer equations for the membranes were numerically solved, and the heat and mass transfer coefficients were calculated based on membrane characteristics. To achieve this, characterisation tests were conducted to measure the characteristic parameters of the membranes. Porosity tests were conducted via gravimetric analysis using wetting and non-wetting liquids. The reason for using the wetting liquid was to wet the membrane completely to eliminate the effect of air trapped in the pores. The technique was used on separate the layers of the dual layer membranes, and followed the same steps as for single layer membranes. Maximum and mean pore sizes were measured by Porometer for membranes. Scanning electron microscopy (SEM) was used to measure the thicknesses of the membranes via imaging of cross sections of the membranes. Contact angle measurement was performed by sessile drop technique for membranes to observe their hydrophobicity. For dual layer membranes, both sides were tested. M1 was the most hydrophobic membrane. For dual layer membranes M4 and M5, hydrophilicity for M5 was greater than M4 (lower contact angle), while at the same time the hydrophobicity of the hydrophobic layer of M5 was higher than M4. The porosity for M1 was highest with 93%. Mean pore size of M1 was higher than the other membranes. M3 had the smallest pore size compared to others. M5 was the thickest membrane, and the hydrophobic layer was thicker than the hydrophilic layer, which limits mass transfer across the membrane. This might be the reason it had lower permeate flux.

DCMD performance tests were conducted with five membranes at different operating conditions in both co-current and counter-current flow modes. Different flowrates and feed and permeate inlet temperatures were tested for the membranes to see the effects on flux and energy efficiency. Global mass transfer coefficients (C_{global}) were calculated for

the membranes to compare them, and this removed the effects of temperature and flowrate. The global mass transfer coefficient was highest for M1 for flows at different velocities and temperatures followed by M2 membrane. Salt rejections of the membranes were approximately 99.5% and higher for all membranes except M5. Lowest rejection of 95.2% was achieved for M5.

Mathematical modelling was undertaken for membranes except M4 membrane because the dense hydrophilic layer required different heat and mass transfer equations compared to M5 membrane and because time of the project was restricted. The model aimed to predict the permeate flux and energy efficiency of DCMD. Some assumptions were made to make the model computationally less challenging. These modelling assumptions were to neglect the following heat loss through the MD module, concentration polarization effect due to low salt concentration, permeate passing the membrane, and sensible heat transfer by the permeate. Flow diagrams for solving the equations were constructed for co- and counter-current flows to enable solving of the heat and mass transfer equations to calculate the overall heat transfer coefficient and mass transfer coefficient. Counter-current flow included the temperature assumption for permeate inlet at the beginning of process because this is an unknown temperature at commencement of the calculations. Model validation was performed by comparing the model results with the experimental results.

A 1-D model was developed for performance modelling of the membranes. M1 membrane performed better than the other membranes regarding permeate flux and thermal efficiency. Having higher porosity, larger pore size, and being thinner was important for higher flux. Although M5 membrane had the high porosity, performance was lower than the others. The thickness and relatively smaller pore size of the dual layer membrane M5 could be the factors for limiting mass transfer. Dual layer membranes, M4 and M5 produced lower fluxes and thermal efficiencies compared to single layer membranes. Modelling accuracy for flux and thermal efficiency was within 10% error (5% experimental error and 5% modelling error), which makes the model reliable for performance modelling of DCMD. Flux variation at different velocities was less sensitive compared to different feed inlet temperatures. The model had more parameters that were influenced by temperature, and those can increase the sensitivity of the model to the temperature rather than velocity. The experiments also showed the same sensitivity as the

model. This was because when the flow was fully developed, further increments of fluxes increase thermal differences marginally. However, temperature increases the vapour pressure exponentially. Thermal efficiency was lower for counter-current flow than co-current flow for all membranes because of higher temperature difference between feed inlet and outlet. However, for some membranes flux was higher with the counter-current flow.

6.3. Recommendations for future studies

Because of lack of time, modelling for M4 (polyurethane coated PTFE) was not performed. For this membrane, the dense hydrophilic layer of the membrane faced the feed side, whereas the hydrophobic layer of M5 was faced on the feed side in the experiments. This changes the mass and heat transfer phenomena for M4 compared to M5, so deriving the equations for modelling M4 membrane requires additional effort. However, modelling the performance for M5 was the initial step for this work as it relates to previous studies reported in scientific literature. Performance modelling for M4 is proposed for future work, and needs to consider water transport through dense membrane where the driving force is related to the vapour pressure difference across the hydrophobic membrane. Additional characterisation of the mass transfer resistance of the dense layer would also be required.

Hydrophobic/hydrophilic dual layer membranes similar to M5 have a higher risk of wetting due to hydrophilic supporting layer compared to hydrophobic single layer membranes. Wetting and leaking can reduce the permeate quality in DCMD, which leads to shorten the membrane run times between cleaning. For future work, wetting capacities of dual layer membranes should be examined.

Successful attempt of 1-D model for hydrophobic/hydrophilic dual layer membranes can lead to in-depth analysis for heat and mass phenomena for the membranes, which can be extended to 2-D models. A 2-D model for dual layer membranes could be developed in the future, and may include effects that arise from concentration and flow velocity.

Nomenclature

- d mean pore diameter of the membrane (m)
- l mean free path (0.11 μm at feed temperature of 60°C) (m)
- k_b Boltzmann constant (1.381×10^{-23}) (JK^{-1})
- P_T Total absolute pressure (Pa) (1.013×10^5)
- σ_A Collision diameter for air (3.711×10^{-10}) (m)
- σ_w Collision diameter for water vapour (2.641×10^{-10}) (m)
- M_w Molecular weight of water (g/mol)
- M_A Molecular weight of air (g/mol)
- R Universal gas constant (8.314472 J/mol.K)
- T Mean temperature in the pore (K)
- P_a Air pressure inside the membrane pores (Pa)
- K_n Knudsen number (dimensionless)
- C_m Mass transfer coefficient ($\text{kg}\cdot\text{m}^{-2}\cdot\text{h}\cdot\text{Pa}$)
- C_{global} Global mass transfer coefficient ($\text{kg}\cdot\text{m}^{-2}\cdot\text{hPa}$)
- PD Diffusion coefficient in the pores ($\text{Pa}\cdot\text{m}^2\cdot\text{s}^{-1}$)
- p_{vf} Partial pressure of water molecule on the feed side (Pa)
- p_{vp} Partial pressure of water molecule on the permeate side (Pa)
- J Mass flux ($\text{kg}\cdot\text{m}^{-2}\cdot\text{s}$)
- T_{mf} Membrane interface temperature on feed side (K)
- T_{mp} Membrane interface temperature on permeate side (K)

T_{bf} Bulk feed temperature (K)

T_{bp} Bulk permeate temperature (K)

T_{sp} Membrane interface temperature between hydrophilic layer and permeate (K)

ν Viscosity ($\text{N}\cdot\text{s}\cdot\text{m}^{-2}=\text{Pa}\cdot\text{s}$) ($\text{kg}\cdot\text{m}^{-1}\cdot\text{s}^{-1}$)

C_p Specific heat of water (J/kgK)

k_h thermal conductivity of fluid ($\text{kg}\cdot\text{m}^{-3}$)

D_{ab} Diffusion coefficient of water ($\text{m}^2\cdot\text{s}^{-1}$)

H_{vap} Heat of vaporization ($\text{J}\cdot\text{kg}^{-1}$)

u Average velocity ($\text{m}\cdot\text{s}^{-1}$)

d_h hydraulic diameter of the channel (m)

ν Kinematic viscosity ($\text{m}\cdot\text{s}^{-2}$)

L Membrane module length (m)

Re Reynolds number (Dimensionless)

Pr Prandtl number (Dimensionless)

Nu Nusselt number (Dimensionless)

Sc Schmidt number (Dimensionless)

Sh Sherwood number (Dimensionless)

w Width of the membrane module (m)

h Height of the membrane module (m)

k_m thermal conductivity of the membrane ($\text{W}\cdot\text{m}^{-1}\cdot\text{K}^{-1}$)

k_g thermal conductivity of the gas ($\text{W}\cdot\text{m}^{-1}\cdot\text{K}^{-1}$)

- k_p thermal conductivity of the polymer ($\text{W}\cdot\text{m}^{-1}\cdot\text{K}^{-1}$)
- h_m heat transfer coefficient of the membrane ($\text{W}\cdot\text{m}^{-2}\cdot\text{K}^{-1}$)
- h_f heat transfer coefficient of feed ($\text{W}\cdot\text{m}^{-2}\cdot\text{K}^{-1}$)
- h_p heat transfer coefficient of permeate ($\text{W}\cdot\text{m}^{-2}\cdot\text{K}^{-1}$)
- ε membrane porosity
- δ membrane thickness (m)
- τ membrane tortuosity
- V flow rate ($\text{m}^3\cdot\text{s}^{-1}$)

References

1. Zhang, J., *Theoretical and experimental investigation of membrane distillation*. 2011, School of Engineering & Science, Victoria University.
2. Wang, P. and T.-S. Chung, *Recent advances in membrane distillation processes: Membrane development, configuration design and application exploring*. Journal of Membrane Science, 2015. **474**: p. 39-56.
3. Alklaibi, A.M. and N. Lior, *Membrane-distillation desalination: status and potential*. Desalination, 2005. **171**(2): p. 111-131.
4. Drioli, E., A. Ali, and F. Macedonio, *Membrane distillation: Recent developments and perspectives*. Desalination, 2015. **356**: p. 56-84.
5. Thomas, N., et al., *Membrane distillation research & implementation: Lessons from the past five decades*. Separation and Purification Technology, 2017. **189**: p. 108-127.
6. Pangarkar, B.L., M.G. Sane, and M. Guddad, *Reverse osmosis and membrane distillation for desalination of groundwater: a review*. ISRN Materials Science, 2011. **2011**.
7. Tavakkoli, S., et al., *A techno-economic assessment of membrane distillation for treatment of Marcellus shale produced water*. Desalination, 2017. **416**: p. 24-34.
8. Shim, W.G., et al., *Solar energy assisted direct contact membrane distillation (DCMD) process for seawater desalination*. Separation and Purification Technology, 2015. **143**: p. 94-104.
9. Khayet, M., J.I. Mengual, and T. Matsuura, *Porous hydrophobic/hydrophilic composite membranes*. Journal of Membrane Science, 2005. **252**(1-2): p. 101-113.
10. Qtaishat, M., M. Khayet, and T. Matsuura, *Guidelines for preparation of higher flux hydrophobic/hydrophilic composite membranes for membrane distillation*. Journal of Membrane Science, 2009. **329**(1-2): p. 193-200.
11. Li, N.N., et al., *Advanced membrane technology and applications*. 2011: John Wiley & Sons.
12. Souhaimi, M.K. and T. Matsuura, *Membrane distillation: principles and applications*. 2011: Elsevier.
13. Qtaishat, M., M. Khayet, and T. Matsuura, *Guidelines for preparation of higher flux hydrophobic/hydrophilic composite membranes for membrane distillation*. Journal of membrane science, 2009. **329**(1): p. 193-200.
14. Wang, L.K., et al., *Membrane and desalination technologies*. Vol. 13. 2008: Springer.
15. Scott, K. and R. Hughes, *Industrial membrane separation technology*. 2012: Springer Science & Business Media.
16. Castel, C. and E. Favre, *Membrane separations and energy efficiency*. Journal of Membrane Science, 2018. **548**: p. 345-357.
17. Noble, R.D. and S.A. Stern, *Membrane separations technology: principles and applications*. Vol. 2. 1995: Elsevier.
18. SIRKAR, K.K., *Membrane separation technologies: current developments*. Chemical Engineering Communications, 1997. **157**(1): p. 145-184.
19. Enrico Drioli, A. and L.P.M. Criscuoli, *Water and WasteWater Treatment Technologies Volume 3*. 2009. **3**.
20. Alkhdhiri, A., N. Darwish, and N. Hilal, *Membrane distillation: A comprehensive review*. Desalination, 2012. **287**: p. 2-18.
21. Zhang, J., et al., *Modelling for scale-up of membrane distillation processes*. 2009.
22. Yun, Y., et al., *Direct contact membrane distillation mechanism for high concentration NaCl solutions*. Desalination, 2006. **188**(1): p. 251-262.

23. Qtaishat, M.R. and F. Banat, *Desalination by solar powered membrane distillation systems*. Desalination, 2013. **308**: p. 186-197.
24. U. Lawal, D. and A. E. Khalifa, *Flux Prediction in Direct Contact Membrane Distillation*. International Journal of Materials, Mechanics and Manufacturing, 2014. **2**(4): p. 302-308.
25. Drioli, E., A. Criscuoli, and L.P. Molero, *Membrane distillation*. EOLSS Encycl, 2000.
26. Tijjng, L.D., et al., *Fouling and its control in membrane distillation—A review*. Journal of Membrane Science, 2015. **475**: p. 215-244.
27. Goh, S., et al., *Fouling and wetting in membrane distillation (MD) and MD-bioreactor (MDBR) for wastewater reclamation*. Desalination, 2013. **323**: p. 39-47.
28. Gryta, M., *Influence of polypropylene membrane surface porosity on the performance of membrane distillation process*. Journal of Membrane Science, 2007. **287**(1): p. 67-78.
29. Chanachai, A., K. Meksup, and R. Jiratananon, *Coating of hydrophobic hollow fiber PVDF membrane with chitosan for protection against wetting and flavor loss in osmotic distillation process*. Separation and Purification Technology, 2010. **72**(2): p. 217-224.
30. Camacho, L., et al., *Advances in Membrane Distillation for Water Desalination and Purification Applications*. Water, 2013. **5**(1): p. 94-196.
31. Essalhi, M. and M. Khayet, *Application of a porous composite hydrophobic/hydrophilic membrane in desalination by air gap and liquid gap membrane distillation: A comparative study*. Separation and Purification Technology, 2014. **133**: p. 176-186.
32. Summers, E.K., H.A. Arafat, and J.H. Lienhard, *Energy efficiency comparison of single-stage membrane distillation (MD) desalination cycles in different configurations*. Desalination, 2012. **290**: p. 54-66.
33. Eykens, L., et al., *How to select a membrane distillation configuration? Process conditions and membrane influence unraveled*. Desalination, 2016. **399**: p. 105-115.
34. El-Bourawi, M.S., et al., *A framework for better understanding membrane distillation separation process*. Journal of Membrane Science, 2006. **285**(1-2): p. 4-29.
35. Susanto, H., *Towards practical implementations of membrane distillation*. Chemical Engineering and Processing: Process Intensification, 2011. **50**(2): p. 139-150.
36. Cipollina, A., et al., *Development of a Membrane Distillation module for solar energy seawater desalination*. Chemical Engineering Research and Design, 2012. **90**(12): p. 2101-2121.
37. Wenten, I.G., *Ultrafiltration in Water Treatment and Its Evaluation as Pretreatment for Reverse Osmosis System*. 2008.
38. Strathmann, H., *Membrane separation processes: Current relevance and future opportunities*. AIChE Journal, 2001. **47**(5): p. 1077-1087.
39. Wilderer, P.A., *Treatise on water science*. 2010: Newnes.
40. Khayet, M., *Membranes and theoretical modeling of membrane distillation: a review*. Adv Colloid Interface Sci, 2011. **164**(1-2): p. 56-88.
41. Lin, P.-J., et al., *Prevention of surfactant wetting with agarose hydrogel layer for direct contact membrane distillation used in dyeing wastewater treatment*. Journal of Membrane Science, 2015. **475**: p. 511-520.
42. Qtaishat, M., et al., *Heat and mass transfer analysis in direct contact membrane distillation*. Desalination, 2008. **219**(1-3): p. 272-292.
43. Qtaishat, M., M. Khayet, and T. Matsuura, *Novel porous composite hydrophobic/hydrophilic polysulfone membranes for desalination by direct contact membrane distillation*. Journal of Membrane science, 2009. **341**(1): p. 139-148.
44. Lee, J.-G., et al., *Performance modeling of direct contact membrane distillation (DCMD) seawater desalination process using a commercial composite membrane*. Journal of Membrane Science, 2015. **478**: p. 85-95.

45. Khayet, M., *Membranes and theoretical modeling of membrane distillation: a review*. Advances in colloid and interface science, 2011. **164**(1): p. 56-88.
46. Zhang, J., et al., *Identification of material and physical features of membrane distillation membranes for high performance desalination*. Journal of Membrane Science, 2010. **349**(1-2): p. 295-303.
47. Swaminathan, J., et al., *Membrane distillation model based on heat exchanger theory and configuration comparison*. Applied Energy, 2016. **184**: p. 491-505.
48. Zhao, S., et al., *Condensation studies in membrane evaporation and sweeping gas membrane distillation*. Journal of Membrane Science, 2014. **462**: p. 9-16.
49. Salehi, S.M., et al., *Membrane distillation by novel hydrogel composite membranes*. Journal of Membrane Science, 2016. **504**: p. 220-229.
50. Huang, J., et al., *Study of a new novel process for preparing and co-stretching PTFE membrane and its properties*. European Polymer Journal, 2004. **40**(4): p. 667-671.
51. Arafat, H., M. Bilad, and F. Marzooqi, *New Concept for Dual-Layer Hydrophilic/Hydrophobic Composite Membrane for Membrane Distillation*. Journal of Membrane and Separation Technology, 2015. **4**(3): p. 122-133.
52. Zuo, J., S. Bonyadi, and T.-S. Chung, *Exploring the potential of commercial polyethylene membranes for desalination by membrane distillation*. Journal of Membrane Science, 2016. **497**: p. 239-247.
53. Zhang, J. and S. Gray, *Effect of applied pressure on performance of PTFE membrane in DCMD*. Journal of Membrane Science, 2011. **369**(1): p. 514-525.
54. Cath, T.Y., V.D. Adams, and A.E. Childress, *Experimental study of desalination using direct contact membrane distillation: a new approach to flux enhancement*. Journal of Membrane Science, 2004. **228**(1): p. 5-16.
55. Khayet, M., et al., *Design of novel direct contact membrane distillation membranes*. Desalination, 2006. **192**(1-3): p. 105-111.
56. Qtaishat, M., et al., *Preparation and characterization of novel hydrophobic/hydrophilic polyetherimide composite membranes for desalination by direct contact membrane distillation*. Journal of Membrane Science, 2009. **327**(1-2): p. 264-273.
57. Wei, X., et al., *CF 4 plasma surface modification of asymmetric hydrophilic polyethersulfone membranes for direct contact membrane distillation*. Journal of membrane science, 2012. **407**: p. 164-175.
58. Bonyadi, S., T.S. Chung, and R. Rajagopalan, *A novel approach to fabricate macrovoid-free and highly permeable PVDF hollow fiber membranes for membrane distillation*. AIChE journal, 2009. **55**(3): p. 828-833.
59. Deshpande, J., K. Nithyanandam, and R. Pitchumani, *Analysis and design of direct contact membrane distillation*. Journal of Membrane Science, 2017. **523**: p. 301-316.
60. Marriott, J., E. Sørensen, and I. Bogle, *Detailed mathematical modelling of membrane modules*. Computers & Chemical Engineering, 2001. **25**(4): p. 693-700.
61. Alsaadi, A.S., et al., *Modeling of air-gap membrane distillation process: A theoretical and experimental study*. Journal of Membrane Science, 2013. **445**: p. 53-65.
62. Ibrahim, S.S. and Q.F. Alsalhy, *Modeling and simulation for direct contact membrane distillation in hollow fiber modules*. AIChE Journal, 2013. **59**(2): p. 589-603.
63. Zhang, J., S. Gray, and J.-D. Li, *Modelling heat and mass transfers in DCMD using compressible membranes*. Journal of Membrane Science, 2012. **387-388**: p. 7-16.
64. Zhang, J., S. Gray, and J.-D. Li, *Predicting the influence of operating conditions on DCMD flux and thermal efficiency for incompressible and compressible membrane systems*. Desalination, 2013. **323**: p. 142-149.
65. Chen, T.-C., C.-D. Ho, and H.-M. Yeh, *Theoretical modeling and experimental analysis of direct contact membrane distillation*. Journal of Membrane Science, 2009. **330**(1): p. 279-287.

66. Zhang, J., J.-D. Li, and S. Gray, *Researching and modelling the dependence of MD flux on membrane dimension for scale-up purpose*. Desalination and Water Treatment, 2011. **31**(1-3): p. 144-150.
67. Hwang, H.J., et al., *Direct contact membrane distillation (DCMD): Experimental study on the commercial PTFE membrane and modeling*. Journal of Membrane Science, 2011. **371**(1-2): p. 90-98.
68. Soukane, S., et al., *Effect of feed flow pattern on the distribution of permeate fluxes in desalination by direct contact membrane distillation*. Desalination, 2017. **418**: p. 43-59.
69. Bonyadi, S. and T.S. Chung, *Flux enhancement in membrane distillation by fabrication of dual layer hydrophilic–hydrophobic hollow fiber membranes*. Journal of Membrane Science, 2007. **306**(1-2): p. 134-146.
70. Su, M., et al., *Effect of inner-layer thermal conductivity on flux enhancement of dual-layer hollow fiber membranes in direct contact membrane distillation*. Journal of Membrane Science, 2010. **364**(1-2): p. 278-289.
71. Saffarini, R.B., et al., *Effect of temperature-dependent microstructure evolution on pore wetting in PTFE membranes under membrane distillation conditions*. Journal of Membrane Science, 2013. **429**: p. 282-294.
72. Zhang, J., J.-D. Li, and S. Gray, *Effect of applied pressure on performance of PTFE membrane in DCMD*. Journal of Membrane Science, 2011. **369**(1-2): p. 514-525.
73. Khayet, M. and T. Matsuura, *Application of surface modifying macromolecules for the preparation of membranes for membrane distillation*. Desalination, 2003. **158**(1-3): p. 51-56.
74. Bonnard, B., P. Causse, and F. Trochu, *EXPERIMENTAL INVESTIGATION OF CAPILLARY FLOW POROMETRY FOR CHARACTERIZATION OF DUAL SCALE POROSITY IN FIBROUS REINFORCEMENTS*.
75. Phillips, R.K., et al., *Ex-situ Measurement of Properties of Gas Diffusion Layers of PEM Fuel Cells*. Energy Procedia, 2012. **29**: p. 486-495.
76. Khayet, M. and T. Matsuura, *Preparation and characterization of polyvinylidene fluoride membranes for membrane distillation*. Industrial & engineering chemistry Research, 2001. **40**(24): p. 5710-5718.
77. Zhang, J., et al., *Depletion of VOC in wastewater by vacuum membrane distillation using hydrophilic-hydrophobic membrane: mechanism of mass transfer and selectivity*. Unpublished.
78. Criscuoli, A., M.C. Carnevale, and E. Drioli, *Evaluation of energy requirements in membrane distillation*. Chemical Engineering and Processing: Process Intensification, 2008. **47**(7): p. 1098-1105.
79. Eykens, L., et al., *Influence of membrane thickness and process conditions on direct contact membrane distillation at different salinities*. Journal of Membrane Science, 2016. **498**: p. 353-364.
80. Zhang, Y., et al., *Review of thermal efficiency and heat recycling in membrane distillation processes*. Desalination, 2015. **367**: p. 223-239.
81. Li, Z., et al., *Effects of thermal efficiency in DCMD and the preparation of membranes with low thermal conductivity*. Applied Surface Science, 2014. **317**: p. 338-349.
82. Yang, X., et al., *Optimization of microstructured hollow fiber design for membrane distillation applications using CFD modeling*. Journal of membrane science, 2012. **421**: p. 258-270.
83. Hou, D., et al., *Preparation and characterization of PVDF/nonwoven fabric flat-sheet composite membranes for desalination through direct contact membrane distillation*. Separation and Purification Technology, 2012. **101**: p. 1-10.

84. Edwie, F., M.M. Teoh, and T.-S. Chung, *Effects of additives on dual-layer hydrophobic-hydrophilic PVDF hollow fiber membranes for membrane distillation and continuous performance*. Chemical Engineering Science, 2012. **68**(1): p. 567-578.
85. Mostafa, M.G., et al., *Membrane Distillation of Meat Industry Effluent with Hydrophilic Polyurethane Coated Polytetrafluoroethylene Membranes*. 2017. **7**: p. 55.
86. Shirazi, M.M.A., A. Kargari, and M. Tabatabaei, *Evaluation of commercial PTFE membranes in desalination by direct contact membrane distillation*. Chemical Engineering and Processing: Process Intensification, 2014. **76**: p. 16-25.
87. Al-Obaidani, S., et al., *Potential of membrane distillation in seawater desalination: thermal efficiency, sensitivity study and cost estimation*. Journal of Membrane Science, 2008. **323**(1): p. 85-98.
88. Duong, H.C., et al., *Optimising thermal efficiency of direct contact membrane distillation by brine recycling for small-scale seawater desalination*. Desalination, 2015. **374**: p. 1-9.
89. Soni, V., et al., *A general model for membrane-based separation processes*. Computers & Chemical Engineering, 2009. **33**(3): p. 644-659.
90. Baehr, H.D. and K. Stephan, *Heat and mass transfer*, 1998. Springer.
91. Hitsov, I., et al., *Modelling approaches in membrane distillation: A critical review*. Separation and Purification Technology, 2015. **142**: p. 48-64.
92. Adnan, S., et al., *Commercial PTFE membranes for membrane distillation application: effect of microstructure and support material*. Desalination, 2012. **284**: p. 297-308.
93. Hitsov, I., et al., *Full-scale direct contact membrane distillation (DCMD) model including membrane compaction effects*. Journal of Membrane Science, 2017. **524**: p. 245-256.
94. Al-Anezi, A.A.-H., et al., *Experimental Investigation of Heat and Mass Transfer in Tubular Membrane Distillation Module for Desalination*. ISRN Chemical Engineering, 2012. **2012**: p. 1-8.
95. Srisurichan, S., R. Jiraratananon, and A. Fane, *Mass transfer mechanisms and transport resistances in direct contact membrane distillation process*. Journal of Membrane Science, 2006. **277**(1-2): p. 186-194.
96. Phattaranawik, J., *Effect of pore size distribution and air flux on mass transport in direct contact membrane distillation*. Journal of Membrane Science, 2003. **215**(1-2): p. 75-85.
97. Khayet, M., K. Khulbe, and T. Matsuura, *Characterization of membranes for membrane distillation by atomic force microscopy and estimation of their water vapor transfer coefficients in vacuum membrane distillation process*. Journal of Membrane Science, 2004. **238**(1-2): p. 199-211.
98. Bui, V.A., L.T.T. Vu, and M.H. Nguyen, *Simulation and optimisation of direct contact membrane distillation for energy efficiency*. Desalination, 2010. **259**(1-3): p. 29-37.
99. Phattaranawik, J., R. Jiraratananon, and A. Fane, *Heat transport and membrane distillation coefficients in direct contact membrane distillation*. Journal of Membrane Science, 2003. **212**(1): p. 177-193.
100. Coker, A.K., *Ludwig's applied process design for chemical and petrochemical plants*. 2014: Gulf Professional Publishing.
101. Shirazi, M.M.A., et al., *Computational Fluid Dynamic (CFD) opportunities applied to the membrane distillation process: State-of-the-art and perspectives*. Desalination, 2016. **377**: p. 73-90.
102. Ngo, I.-L., S. Jeon, and C. Byon, *Thermal conductivity of transparent and flexible polymers containing fillers: A literature review*. International Journal of Heat and Mass Transfer, 2016. **98**: p. 219-226.

Appendix

(I) Single Layer Membranes Co-current Model

```
clear all
l=1*10^-7;
%d=5.107*10^-7; %PTFE membrane
%d=2.07*10^-7; %PE membrane
d=1.878*10^-7; %O-PE membrane
%epsilon=0.93; %PTFE membrane
%epsilon=0.85; %PE membrane
epsilon=0.79; %O-PE membrane
tau=((2-epsilon)^2/(epsilon));
%delta=9.66*10^-5; %PTFE membrane
%delta=1.428*10^-5; %PE membrane
delta=3.33*10^-5; %O-PE membrane
M=18.02;
R=8314.472;
Pa=1.013*10^5;
%kp=0.25;%PTFE membrane
%kp=0.11;%PE membrane
kp=0.11; %O-PE membrane
kg=0.0272;
km=(1-epsilon)*kp+(epsilon*kg);
w=0.135;
h=0.0008;
df=0.0004;
hsp=0.0008;
theta=90;
lm=0.003;
epsilon_s=1-pi*df^2/(2*lm*hsp*sin(theta));
Svsp=4.0/df;
dh=4.0*epsilon_s/(2/hsp+(1-epsilon_s)*Svsp);
alpha_s=1.904*(df/h)^(-
0.039)*epsilon_s^0.75*(sin(theta/2))^0.086;
A=w*h;
V=8.83*10^-6; %530 ml/min
%V=1*10^-5; %600 ml/min
%V=7.5*10^-6; %450 ml/min
%V=1.25*10^-5; %750 ml/min
```

```

%V=1.083*10^-5; %650 ml/min
u=V/(A*epsilon_s);
L=0.135;
Kn=l/d;
error=1;
N=1000;
dx=L/(N-1);
x=0:dx:L;
Tf_in=333;
Tp_in=293;
Tbf(1:N)=333;
Tbp(1:N)=293;
J(1:N)=0;
for i=1:N
    J(1)=0;
    x1=x(i);
    if 0<=x1 && x1<=L
Re_f=(u*density(Tbf(i))*dh)/(viscosity(Tbf(i)))
;
Re_p=(u*density(Tbp(i))*dh)/(viscosity(Tbp(i)))
;
Pr_f=(viscosity(Tbf(i))*heatcapacity(Tbf(i)))/(
thermalconductivity(Tbf(i)));
Pr_p=(viscosity(Tbp(i))*heatcapacity(Tbp(i)))/(
thermalconductivity(Tbp(i)));
%Nu_f=alpha_s*(Re_f^1)*(Pr_f^0.33); %PTFE
membrane %O-PE
%Nu_p=alpha_s*(Re_p^1)*(Pr_p^0.33); %PTFE
membrane %O-PE
%Nu_f=alpha_s*0.027*(Re_f^0.8)*(Pr_f^0.33);
%Nu_p=alpha_s*0.027*(Re_p^0.8)*(Pr_p^0.33);
%Nu_f=alpha_s*0.13*(Re_f^0.64)*(Pr_f^0.4);
%Nu_p=alpha_s*0.13*(Re_p^0.64)*(Pr_p^0.4);
%Nu_f=alpha_s*0.036*Re_f^0.8*Pr_f^0.333*(dh/L)^
0.055;
%Nu_p=alpha_s*0.036*Re_p^0.8*Pr_p^0.333*(dh/L)^
0.055;
Nu_f=alpha_s*0.023*(Re_f^0.8)*(Pr_f^0.33)*(1+(6
*dh/L)); %PE memb
Nu_p=alpha_s*0.023*(Re_p^0.8)*(Pr_p^0.33)*(1+(6
*dh/L)); %PE memb

```

```

%Nu_f=alpha_s*0.023*(Re_f^0.54)*(Pr_f^0.3);%*(d
h/L)^0.055;
%Nu_p=alpha_s*0.023*(Re_p^0.54)*(Pr_p^0.3);%*(d
h/L)^0.055;
%Nu_f=alpha_s*0.664*(Re_f^0.5)*(Pr_f^0.33)*(2*d
h/L)^0.5;
%Nu_p=alpha_s*0.664*(Re_p^0.5)*(Pr_p^0.33)*(2*d
h/L)^0.5;
%Nu_f=alpha_s*(4.36+((0.036*Re_f*Pr_f*(dh/L))/(
1+(0.0011*(Re_f*Pr_f*((dh/L)^0.8))))));
%Nu_p=alpha_s*(4.36+((0.036*Re_p*Pr_p*(dh/L))/(
1+(0.0011*(Re_p*Pr_p*((dh/L)^0.8))))));
h_f=(Nu_f*thermalconductivity(Tbf(i)))/dh;
h_p=(Nu_p*thermalconductivity(Tbp(i)))/dh;
U=1/((1/h_f)+(delta/km)+(1/h_p));
Q=(Tbf(i)-
Tbp(i)+J(i)*heatofvaporization(Tbf(i))/(km/delt
a))*U;
Tmf(i)=Tbf(i)-(Q/h_f);
Tmp(i)=Tbp(i)+(Q/h_p);
end
Tf_up=340;
Tf_low=313;
Tp_up=303;
Tp_low=290;
iter=0;
while error>0.0001 && iter<100
    Tmf2=(1/2)*(Tf_up+Tf_low);
    Tmp2=(1/2)*(Tp_up+Tp_low);
    T=((Tmf2+Tmp2)/2);
PD=(1.19*(10^-4))*(T^1.75);
Cm=((3/2)*((tau*delta)/(epsilon*d))*((pi*R*T/8*
M)^(1/2))+(((tau*delta/epsilon))*(Pa/PD)*(R*T/M
)))^-1;
J(i)=Cm*(saturationpressure1(Tmf2)-
saturationpressure1(Tmp2));
Tmf1=Tbf(i)-(Q/h_f);
Tmp1=Tbp(i)+(Q/h_p);
error1=abs((Tmf2-Tmf1)/(Tmf2));
error2=abs((Tmp2-Tmp1)/(Tmp2));
error=max(error1,error2);

```

```

if Tmf1>Tmf2
    Tf_up=Tmf1;
end
if Tmf1<Tmf2
    Tf_low=Tmf1;
end
if Tmp1>Tmp2
    Tp_up=Tmp1;
end
if Tmp1<Tmp2
    Tp_low=Tmp1;
end

    iter=iter+1;

end
if i==1
    Tbf(i)=Tf_in-
dx*w*Q/(heatcapacity(Tbf(i))*u*density(Tbf(i))*
A);
Tbp(i)=Tp_in+dx*w*Q/(heatcapacity(Tbp(i))*u*den
sity(Tbp(i))*A);
else
    Tbf(i)=Tbf(i-1)-
dx*w*Q/(heatcapacity(Tbf(i))*u*density(Tbf(i))*
A);
    Tbp(i)=Tbp(i-
1)+dx*w*Q/(heatcapacity(Tbp(i))*u*density(Tbp(i)
))*A);
end
Q=U*(Tbf(i)-Tbp(i));
Tmf(i)=Tbf(i)-(Q/h_f);
Tmp(i)=Tbp(i)+(Q/h_p);
J(i)=Cm*(saturationpressure1(Tmf(i))-
saturationpressure1(Tmp(i)));
E=(mean(J)*0.018*heatofvaporization(Tbf(1)))/(4.
17*530/60*(Tbf(1)-Tbf(i)));
Cf=1560;
Cp=9;
salt_R=(Cf-Cp)/Cf;
end

```

(II) Single Layer Membranes Counter-current Model

```
clear all
l=1*10^-7;
%d=5.107*10^-7; %PTFE membrane
d=2.07*10^-7; %PE membrane
%d=1.878*10^-7; %O-PE membrane
%epsilon=0.93; %PTFE membrane
%epsilon=0.85; %PE membrane
epsilon=0.79; %O-PE membrane
tau=((2-epsilon)^2/(epsilon));
%delta=9.66*10^-5; %PTFE membrane
delta=1.428*10^-5; %PE membrane
%delta=3.33*10^-5; %O-PE membrane
M=18.02;
R=8314.472;
Pa=1.013*10^5;
%kp=0.25; %PTFE membrane
kp=0.11; %PE membrane
%kp=0.11; %O-PE membrane
kg=0.0272;
km=(1-epsilon)*kp+(epsilon*kg);
w=0.135;
h=0.0008;
df=0.0004;
hsp=0.0008;
theta=pi/4;
lm=0.003;
epsilon_s=1-pi*df^2/(2*lm*hsp*sin(theta));
Svsp=4.0/df;
dh=4.0*epsilon_s/(2/hsp+(1-epsilon_s)*Svsp);
alpha_s=1.904*(df/h)^(-
0.039)*epsilon_s^0.75*(sin(theta/2))^0.086;
A=w*h;
V=8.83*10^-6; %530 ml/min
%V=1*10^-5; %600 ml/min
%V=7.5*10^-6; %450 ml/min
%V=1.25*10^-5; %750 ml/min
%V=1.083*10^-5; %650 ml/min
u=V/(A*epsilon_s);
```

```

L=0.135;
Kn=1/d;
error=1;
N=1000;
dx=L/(N-1);
x=0:dx:L;
Tf_in=343;
Tp_in=293;
Tc_up=Tf_in;
Tc_low=Tp_in;
Tbf(1:N)=343;
Tbp(1:N)=293;
J(1:N)=0;
counter=0;
while error>0.00001 && counter<100

Tc_guess=0.5*(Tc_up+Tc_low);

for i=1:N
    x1=x(i);
    Tmf(1)=Tf_in;
    Tmp(1)=Tc_guess;
    Tbf(1)=Tf_in;
    Tbp(1)=Tc_guess;
    J(1)=0;
    if 0<=x1 && x1<=L
Re_f=(u*density(Tbf(i))*dh)/(viscosity(Tbf(i)))
;
Re_p=(u*density(Tbp(i))*dh)/(viscosity(Tbp(i)))
;
Pr_f=(viscosity(Tbf(i))*heatcapacity(Tbf(i)))/(
thermalconductivity(Tbf(i)));
Pr_p=(viscosity(Tbp(i))*heatcapacity(Tbp(i)))/(
thermalconductivity(Tbp(i)));
%Nu_f=alpha_s*(Re_f^1)*(Pr_f^0.33); %PTFE
%Nu_p=alpha_s*(Re_p^1)*(Pr_p^0.33); %PTFE
%Nu_f=alpha_s*0.027*(Re_f^0.5)*(Pr_f^0.33);
%Nu_p=alpha_s*0.027*(Re_p^0.5)*(Pr_p^0.33);
%Nu_f=0.13*(Re_f^0.64)*(Pr_f^0.4); %O-PE
%Nu_p=0.13*(Re_p^0.64)*(Pr_p^0.4); %O-PE

```

```

%Nu_f=alpha_s*0.023*(Re_f^0.8)*(Pr_f^0.33)*(1+(
6*dh/L));
%Nu_p=alpha_s*0.023*(Re_p^0.8)*(Pr_p^0.33)*(1+(
6*dh/L));
Nu_f=alpha_s*0.036*Re_f^0.8*Pr_f^0.333*(dh/L)^0
.055; %PE
Nu_p=alpha_s*0.036*Re_p^0.8*Pr_p^0.333*(dh/L)^0
.055; %PE
%Nu_f=alpha_s*0.664*Re_f^0.5*Pr_f^0.333*(2*dh/L
)^0.5;
%Nu_p=alpha_s*0.664*Re_p^0.5*Pr_p^0.333*(2*dh/L
)^0.5;
%Nu_f=alpha_s*(4.36+0.036*Re_f*Pr_f*dh/L/(1+0.0
011*(Re_f*Pr_f*dh/L)^0.8));
%Nu_p=alpha_s*(4.36+0.036*Re_p*Pr_p*dh/L/(1+0.0
011*(Re_p*Pr_p*dh/L)^0.8));
h_f=(Nu_f*thermalconductivity(Tbf(i)))/dh;
h_p=(Nu_p*thermalconductivity(Tbp(i)))/dh;
U=1/((1/h_f)+(delta/km)+(1/h_p));
Q=(Tbf(i)-
Tbp(i)+J(i)*heatofvaporization(Tbf(i))/(km/delt
a))*U;
Tmf(i)=Tbf(i)-(Q/h_f);
Tmp(i)=Tbp(i)+(Q/h_p);
    end
Tf_up=340;
Tf_low=313;
Tp_up=303;
Tp_low=290;
iter=0;
while error>0.0001 && iter<100
    Tmf2=(1/2)*(Tf_up+Tf_low);
    Tmp2=(1/2)*(Tp_up+Tp_low);
    T=((Tmf2+Tmp2)/2);
PD=(1.19*(10^-4))*(T^1.75);
Cm=((3/2)*((tau*delta)/(epsilon*d))*((pi*R*T/8*
M)^(1/2))+(((tau*delta/epsilon)*(Pa/PD)*(R*T/M
))))^-1;
J(i)=Cm*(saturationpressure1(Tmf2)-
saturationpressure1(Tmp2));
Tmf1=Tbf(i)-(Q/h_f);

```

```

Tmp1=Tbp (i) + (Q/h_p) ;
error1=abs ((Tmf2-Tmf1) / (Tmf2)) ;
error2=abs ((Tmp2-Tmp1) / (Tmp2)) ;
error=max (error1,error2) ;
if Tmf1>Tmf2
    Tf_up=Tmf1;
end
if Tmf1<Tmf2
    Tf_low=Tmf1;
end
if Tmp1>Tmp2
    Tp_up=Tmp1;
end
if Tmp1<Tmp2
    Tp_low=Tmp1;
end

    iter=iter+1;

end
if i==1
    Tbf (i)=Tf_in-
dx*w*Q/ (heatcapacity (Tbf (i)) *u*density (Tbf (i)) *
A) ;
    Tbp (i)=Tp_in-
dx*w*Q/ (heatcapacity (Tbp (i)) *u*density (Tbp (i)) *
A) ;
else
    Tbf (i)=Tbf (i-1) -
dx*w*Q/ (heatcapacity (Tbf (i)) *u*density (Tbf (i)) *
A) ;
    Tbp (i)=Tbp (i-1) -
dx*w*Q/ (heatcapacity (Tbp (i)) *u*density (Tbp (i)) *
A) ;
end
Q=U* (Tbf (i) -Tbp (i)) ;
Tmf (i)=Tbf (i) - (Q/h_f) ;
Tmp (i)=Tbp (i) + (Q/h_p) ;
J (i)=Cm* (saturationpressure1 (Tmf (i)) -
saturationpressure1 (Tmp (i))) ;
end

```

```
counter=counter+1;
error=abs((Tbp(N)-Tp_in)/Tp_in);
if (Tbp(N)>Tp_in)
    Tc_up=Tbp(N);
end
if (Tbp(N)<Tp_in)
    Tc_low=Tbp(N);
end
E=(mean(J)*0.018*heatofvaporization(Tbf(1))/(4.
17*530/60*(Tbf(1)-Tbf(i))));
end
```

(III) Dual Layer Membrane Co-current Model

```
clear all
l=1*10^-7;
d_t=3.124*10^-7;
d_s=2.498*10^-7;
epsilon_s= 0.91;
epsilon_t= 0.81;
delta_s= 1.36*10^-5 ;
delta_t=9.3886*10^-5;
tau_t=((2-epsilon_t)^2/(epsilon_t));
M=18.02;
R=8314.472;
Pa=1.013*10^5;
kg=0.0272;
kw=0.6;
ks=0.25;
kt=0.19;
%k_m=(1-epsilon)*kp+(epsilon*kg);
k_s=(kw*epsilon_s)+ks*(1-epsilon_s);
k_t=(kg*epsilon_t)+kt*(1-epsilon_t);
w=0.135;
h=0.0008;
df=0.0004; %diameter of a single spacer fibre
hsp=0.0008; %height of the spacer
%theta=pi/4; %angle between spacer fibres in
the flow direction
theta=90;
lm=0.003; %distance between parallel spacer
fibres
epsilon_spacer=1-
((pi*df^2)/((2*lm*hsp*sin(theta))));
Svsp=4.0/df;
dh=4.0*epsilon_spacer/(2/hsp+(1-
epsilon_spacer)*Svsp);
alpha_s=1.9*((df/hsp)^(0.039))*(epsilon_spacer^
0.75)*((sin(theta/2))^0.086);
A=w*h;
%V=8.83*10^-6; %530 ml/min
V=1*10^-5; %600 ml/min
%V=7.5*10^-6; %450 ml/min
```

```

%V=1.25*10^-5; %750 ml/min
%V=1.083*10^-5; %650 ml/min
u=V/(A*epsilon_spacer);
%L=0.13;
L=0.127;
Kn=1/d_t;
error=1;
N=1000;
dx=L/(N-1);
x=0:dx:L;
Tf_in=333;
Tp_in=293;
Tbf(1:N)=333;
Tbp(1:N)=293;
J(1:N)=0;
for i=1:N
    J(1)=0;
    x1=x(i);
if 0<=x1 && x1<=L
Re_f=(u*density(Tbf(i))*dh)/(viscosity(Tbf(i)))
;
Re_p=(u*density(Tbp(i))*dh)/(viscosity(Tbp(i)))
;
Pr_f=(viscosity(Tbf(i))*heatcapacity(Tbf(i)))/(
thermalconductivity(Tbf(i)));
Pr_p=(viscosity(Tbp(i))*heatcapacity(Tbp(i)))/(
thermalconductivity(Tbp(i)));
%Nu_f=alpha_s*(Re_f^1)*(Pr_f^0.33);
%Nu_p=alpha_s*(Re_p^1)*(Pr_p^0.33);
%Nu_f=alpha_s*0.027*(Re_f^0.5)*(Pr_f^0.33);
%Nu_p=alpha_s*0.027*(Re_p^0.5)*(Pr_p^0.33);
%Nu_f=alpha_s*0.036*Re_f^0.8*Pr_f^0.333*(dh/L)^
0.055;
%Nu_p=alpha_s*0.036*Re_p^0.8*Pr_p^0.333*(dh/L)^
0.055;
%Nu_f=alpha_s*0.664*Re_f^0.5*Pr_f^0.333*(2*dh/L
)^0.5;
%Nu_p=alpha_s*0.664*Re_p^0.5*Pr_p^0.333*(2*dh/L
)^0.5;
Nu_f=alpha_s*(4.36+0.036*Re_f*Pr_f*dh/L/(1+0.00
11*(Re_f*Pr_f*dh/L)^0.8));

```

```

Nu_p=alpha_s*(4.36+0.036*Re_p*Pr_p*dh/L/(1+0.00
11*(Re_p*Pr_p*dh/L)^0.8));
h_f=(Nu_f*thermalconductivity(Tbf(i)))/dh;
h_p=(Nu_p*thermalconductivity(Tbp(i)))/dh;
h_s=(k_s/delta_s);
h_t=(k_t/delta_t);
U=1/((1/h_f)+(1/h_t)+(1/h_p)+(1/h_s));
Q=(Tbf(i)-
Tbp(i)+J(i)*heatofvaporization(Tbf(i))/h_t)*U;
%Q=(Tbf(i)-
Tbp(i)+J(i)*heatofvaporization(Tbf(i))/(k_t/del
ta_t))*U;
%Q=U*(Tbf(i)-Tbp(i));
Tmf(i)=Tbf(i)-(Q/h_f);
Tsp(i)=Tbp(i)+(Q/h_s);
Tmp(i)=Tbp(i)+(Q/h_p);

end
Tf_up=350;
Tf_low=313;
Tp_up=303;
Tp_low=290;
iter=0;
while error>0.0001 && iter<100
    Tmf2=(1/2)*(Tf_up+Tf_low);
    Tmp2=(1/2)*(Tp_up+Tp_low);
    T=((Tmf2+Tmp2)/2);
PD=(1.19*(10^-4))*(T^1.75);
Cm=((3/2)*((tau_t*delta_t)/(epsilon_t*d_t))*((p
i*R*T/8*M)^(1/2))+(((tau_t*delta_t/epsilon_t))*
(Pa/PD)*(R*T/M)))^-1;
J(i)=Cm*(saturationpressure1(Tmf2)-
saturationpressure1(Tmp2));
Tmf1=Tbf(i)-(Q/h_f);
Tmp1=Tbp(i)+(Q/h_p);
error1=abs((Tmf2-Tmf1)/(Tmf2));
error2=abs((Tmp2-Tmp1)/(Tmp2));
error=max(error1,error2);
if Tmf1>Tmf2
    Tf_up=Tmf1;
end

```

```

if Tmf1<Tmf2
    Tf_low=Tmf1;
end
if Tmp1>Tmp2
    Tp_up=Tmp1;
end
if Tmp1<Tmp2
    Tp_low=Tmp1;
end

    iter=iter+1;

end
if i==1
    Tbf(i)=Tf_in-
dx*w*Q/(heatcapacity(Tbf(i))*u*density(Tbf(i))*
A);

Tbp(i)=Tp_in+dx*w*Q/(heatcapacity(Tbp(i))*u*den
sity(Tbp(i))*A);
else
    Tbf(i)=Tbf(i-1)-
dx*w*Q/(heatcapacity(Tbf(i))*u*density(Tbf(i))*
A);
    Tbp(i)=Tbp(i-
1)+dx*w*Q/(heatcapacity(Tbp(i))*u*density(Tbp(i)
))*A);
end
Q=U*(Tbf(i)-Tbp(i));
Tmf(i)=Tbf(i)-(Q/h_f);
Tmp(i)=Tbp(i)+(Q/h_p);
Tsp(i)=Tbp(i)+(Q/h_s);
J(i)=Cm*(saturationpressure1(Tmf(i))-
saturationpressure1(Tmp(i)));
E=(mean(J)*0.012*heatofvaporization(Tbf(1))/(4.
17*600/60*(Tbf(1)-Tbf(i))));
Cf=1616;
Cp=8.87;
salt_R=(Cf-Cp)/Cf;
end

```

(IV) Dual Layer Membrane Counter-current Model

```
clear all
l=1*10^-7;
d_t=3.124*10^-7;
d_s=2.498*10^-7;
epsilon_s= 0.91;
epsilon_t= 0.81;
delta_s= 1.36*10^-5 ;
delta_t=9.3886*10^-5;
tau_t=((2-epsilon_t)^2/(epsilon_t));
M=18.02;
R=8314.472;
Pa=1.013*10^5;
%kp=0.19;
kg=0.0272;
kw=0.6;
ks=0.25;
kt=0.19;
%k_m=(1-epsilon)*kp+(epsilon*kg);
k_s=(kw*epsilon_s)+ks*(1-epsilon_s);
k_t=(kg*epsilon_t)+kt*(1-epsilon_t);
w=0.135;
h=0.0008;
df=0.0004;
hsp=0.0008;
theta=90;
lm=0.003;
epsilon_spacer=1-
((pi*df^2)/((2*lm*hsp*sin(theta))));
Svsp=4.0/df;
dh=4.0*epsilon_spacer/(2/hsp+(1-
epsilon_spacer)*Svsp);
alpha_s=1.9*((df/hsp)^(0.039))*(epsilon_spacer^
0.75)*((sin(theta/2))^0.086);
A=w*h;
%V=8.83*10^-6; %530 ml/min
V=1*10^-5; %600 ml/min
%V=7.5*10^-6; %450 ml/min
%V=1.25*10^-5; %750 m/min
%V=1.083*10^-5; %650 ml/min
```

```

u=V/(A*epsilon_spacer);
%L=0.13;
L=0.127;
Kn=1/d_t;
error=1;
N=1000;
dx=L/(N-1);
x=0:dx:L;
Tf_in=343;
Tp_in=293;
Tc_up=Tf_in;
Tc_low=Tp_in;
Tbf(1:N)=343;
Tbp(1:N)=293;
J(1:N)=0;
counter=0;
while error>0.00001 && counter<100

Tc_guess=0.5*(Tc_up+Tc_low);

for i=1:N
    x1=x(i);
    Tmf(1)=Tf_in;
    Tmp(1)=Tc_guess;
    Tbf(1)=Tf_in;
    Tbp(1)=Tc_guess;
    J(1)=0;
    if 0<=x1 && x1<=L
Re_f=(u*density(Tbf(i))*dh)/(viscosity(Tbf(i)))
;
Re_p=(u*density(Tbp(i))*dh)/(viscosity(Tbp(i)))
;
Pr_f=(viscosity(Tbf(i))*heatcapacity(Tbf(i)))/(
thermalconductivity(Tbf(i)));
Pr_p=(viscosity(Tbp(i))*heatcapacity(Tbp(i)))/(
thermalconductivity(Tbp(i)));
%Nu_f=alpha_s*(Re_f^1)*(Pr_f^0.33);
%Nu_p=alpha_s*(Re_p^1)*(Pr_p^0.33);
%Nu_f=alpha_s*0.027*(Re_f^0.5)*(Pr_f^0.33);
%Nu_p=alpha_s*0.027*(Re_p^0.5)*(Pr_p^0.33);

```

```

Nu_f=alpha_s*0.036*Re_f^0.8*Pr_f^0.333*(dh/L)^0
.055; %counter
Nu_p=alpha_s*0.036*Re_p^0.8*Pr_p^0.333*(dh/L)^0
.055; %counter
%Nu_f=alpha_s*0.664*Re_f^0.5*Pr_f^0.333*(2*dh/L
)^0.5;
%Nu_p=alpha_s*0.664*Re_p^0.5*Pr_p^0.333*(2*dh/L
)^0.5;
%Nu_f=alpha_s*(4.36+0.036*Re_f*Pr_f*dh/L/(1+0.0
011*(Re_f*Pr_f*dh/L)^0.8));
%Nu_p=alpha_s*(4.36+0.036*Re_p*Pr_p*dh/L/(1+0.0
011*(Re_p*Pr_p*dh/L)^0.8));
h_f=(Nu_f*thermalconductivity(Tbf(i)))/dh;
h_p=(Nu_p*thermalconductivity(Tbp(i)))/dh;
h_s=(k_s/delta_s);
h_t=(k_t/delta_t);
U=1/((1/h_f)+(1/h_t)+(1/h_p)+(1/h_s));
Q=(Tbf(i)-
Tbp(i)+J(i)*heatofvaporization(Tbf(i))/h_t)*U;
%Q=U*(Tbf(i)-Tbp(i));
Tmf(i)=Tbf(i)-(Q/h_f);
Tsp(i)=Tbp(i)+(Q/h_s);
Tmp(i)=Tbp(i)+(Q/h_p);
    end

Tf_up=340;
Tf_low=313;
Tp_up=303;
Tp_low=290;
iter=0;
while error>0.0001 && iter<100
    Tmf2=(1/2)*(Tf_up+Tf_low);
    Tmp2=(1/2)*(Tp_up+Tp_low);
    T=(Tmf2+Tmp2)/2;
PD=(1.19*(10^-4))*(T^1.75);
Cm=((3/2)*((tau_t*delta_t)/(epsilon_t*d_t))*((p
i*R*T/8*M)^(1/2))+(((tau_t*delta_t/epsilon_t)*
(Pa/PD)*(R*T/M)))^-1;
J(i)=Cm*(saturationpressure1(Tmf2)-
saturationpressure1(Tmp2));
Tmf1=Tbf(i)-(Q/h_f);

```

```

Tmp1=Tbp (i) + (Q/h_p) ;
error1=abs ((Tmf2-Tmf1) / (Tmf2)) ;
error2=abs ((Tmp2-Tmp1) / (Tmp2)) ;
error=max (error1,error2) ;
if Tmf1>Tmf2
    Tf_up=Tmf1;
end
if Tmf1<Tmf2
    Tf_low=Tmf1;
end
if Tmp1>Tmp2
    Tp_up=Tmp1;
end
if Tmp1<Tmp2
    Tp_low=Tmp1;
end

    iter=iter+1;

end
if i==1
    Tbf (i)=Tf_in-
dx*w*Q/ (heatcapacity (Tbf (i)) *u*density (Tbf (i)) *
A) ;
    Tbp (i)=Tp_in-
dx*w*Q/ (heatcapacity (Tbp (i)) *u*density (Tbp (i)) *
A) ;
else
    Tbf (i)=Tbf (i-1) -
dx*w*Q/ (heatcapacity (Tbf (i)) *u*density (Tbf (i)) *
A) ;
    Tbp (i)=Tbp (i-1) -
dx*w*Q/ (heatcapacity (Tbp (i)) *u*density (Tbp (i)) *
A) ;
end
Q=U* (Tbf (i) -Tbp (i)) ;
Tmf (i)=Tbf (i) - (Q/h_f) ;
Tmp (i)=Tbp (i) + (Q/h_p) ;
J (i)=Cm* (saturationpressure1 (Tmf (i)) -
saturationpressure1 (Tmp (i))) ;
end

```

```

counter=counter+1;
error=abs((Tbp(N)-Tp_in)/Tp_in);
if (Tbp(N)>Tp_in)
    Tc_up=Tbp(N);
end
if (Tbp(N)<Tp_in)
    Tc_low=Tbp(N);
end

E=(mean(J)*0.012*heatofvaporization(Tbf(1))/(4.
17*600/60*(Tbf(1)-Tbf(i))));
Cf=1700;
Cp=450;
salt_R=(Cf-Cp)/Cf;
end

```